Free-trajectory steady motion control optimisation for the descent of elite cyclists

MSc Thesis

A.M. van der Niet

Free-trajectory steady motion control optimisation for the descent of elite cyclists

MSc Thesis

by

A.M. van der Niet

to obtain the degree of Master of Science
at the Delft University of Technology,
to be defended publicly on Monday September 28, 2020 at 11:00 AM.

Student number:	4359496	
Project duration:	February 17, 2020 – September 28, 2020	
Thesis committee:	dr. ir. R. Happee,	chair
	dr. ir. A. L. Schwab,	supervisor
	ir. M. M. Reijne	

Abstract

Minimum-time optimisation has been used extensively in motorsports, such as Formula One racing. Using minimum-time optimisation, the ideal racing line as well as control strategies such as braking strategies can be found. This is interesting, as Reijne et al have shown that cyclists apply diverse strategies, specifically during a descent [51]. With minimum-time optimisation, it is possible to compare a riders performance to the theoretically optimal performance. The results from such optimisations can be used to help with training, as well as improve and test equipment design.

This work describes a free-trajectory steady motion control optimisation for the descent of elite cyclists. The prediction of the individual descent performance was formulated as an optimal control problem and solved with a direct approach to find optimal cornering and braking strategies which yield the shortest descent time. While the state equations were kept simple (3 variables only), more elaborated performance limits were represented by g-g diagrams. Such diagrams represent the longitudinal, lateral and combined acceleration limits for cyclist. A method to numerically derive g-g diagrams for cyclists driving on 3D tracks was designed. In this method, a tire model, power limit and steady motion equations for a cyclist are used to determine the control space. The bicycle and cyclist are modelled as a single rigid body, the tire friction model is simplified as a friction circle, and the wind speed is considered to be zero at all times. As for the 3D road geometry effects, all possible effects are considered in the method, except from lateral road curvature. The resulting method provides g-g diagrams as a function of 8 local geometry and state variables.

The optimisation model was tested against the velocity and trajectory output data measured on Team Sunweb professional cyclists at the L218 descent in Germany. The resulting trajectory was similar to the trajectory ridden by the elite cyclists. The velocity profile showed large differences, which are a result of a combination of inaccurate track data, differences in friction coefficient estimation, and safety margins applied by the cyclists. The results show that descent performance can be improved, as even when adhering to safety margins harder braking is possible. Overall, the model responds as expected to changes in track, environment and bicycle/rider parameters.

Steps can be made towards better implementation of the g-g diagrams in the minimum-time optimisation. Furthermore, a more accurate tire model and power model can improve the model and extend its applications. The presented model can be used for qualitative descent analyses, and facilitate the training of elite cyclists.

Keywords— optimal control problem, minimum-time, optimisation, cycling, free-trajectory, g-g diagram

Contents

Nomenclature

List of Abbreviations

CoM	Center of Mass
CP	Critical Power
DoF	Degree(s) of Freedom
$M-M$	Margaria-Morton (power model)
NLP	Non-Linear Program
OCP	Optimal Control Problem
QSS	Quasi-Steady-State
UCI	Union Cycliste Internationale

bicycle and rider parameters

b	longitudinal distance from the rear contact point to the CoM in the bicycle ($\mathcal{F}$) frame
C_dA	drag area coefficient
h	height of the CoM
m	mass
P_{max}	power limit
w	wheelbase

curve and ribbon geometry

β	twist angle
$\boldsymbol{b}$	unit binormal vector
$\boldsymbol{m}$	unit ribbon normal vector
$\boldsymbol{n}$	unit camber vector
$\boldsymbol{p}$	unit principal normal vector
$\boldsymbol{t}$	unit tangent vector
γ	banking (Euler) angle (lateral slope)
κ	curvature
ψ	elevation (Euler) angle (forward slope)
τ	torsion
n	lateral position with respect to the road center line
s	distance along the road center line

frames

$\mathcal{B}$	ribbon frame
$\mathcal{C}$	curvature frame
$\mathcal{D}$	driving frame
$\mathcal{F}$	bicycle frame
$\mathcal{K}$	cyclist's principal curvature frame
$\mathcal{N}$	fixed frame

other

α	adherence orientation
$\boldsymbol{F}$	force
χ	orientation of the cyclist with respect to the tangent to the road center line
δ	air density
μ	friction coefficient
ϕ	roll angle
ρ	radius of curvature
a_x	longitudinal acceleration
a_y	lateral acceleration
g	gravitational constant
r	adherence radius
v	velocity along the trajectory
W'	anaerobic work capacity

List of Figures

List of Tables

1 Introduction

Sport is continuously evolving. Innovations in gear, food schemes, and personal training plans are the way to improve performances. One of those innovations is minimum-time optimisation. In both physical sports and motorsports this technique is used to find out how the best racing time can be achieved. When Max Verstappen is preparing himself for a race in his VR simulator, his performance is compared to an 'optimal' performance. An optimal racing line and a speed indication have been calculated through minimum-time optimisation.

1.1. background

Minimum-time optimisation was used in motorsport since approximately the sixties [63], although its first shown success was in 1989, when computers could be deployed and predictions got close to reality [19]. An example of this first computer generated result is found in figure 1.1. In motorsport, it is used to determine the racing line and accelerations along the track. Later on, the idea was extended towards physical sports. In physical sports, it is used to find the optimal power distribution during a race. This is often called an optimal pacing strategy. There are several ways in which minimum-time optimisation can be used. First of all, it can be used to understand what happens during a race and to find out which factors have the greatest influence on the total lap-time. For example, why is it better to slow down earlier, or why does a parabolic power distribution yield the best results? Secondly, it can be used to theoretically 'test' new gear before it is actually made. Furthermore, the pros and cons of both gear and sportsman parameters (mass, tire materials, etc.) can be explored. This is used a lot in formula-1 racing, as only a few test drives are allowed to determine the best setup. Lastly, the information can be used to train sportsmen to perform in the theoretically best way.

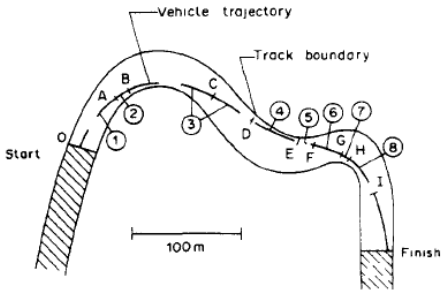

Figure 1.1: A computer generated optimal trajectory on a section of the Paul Ricard circuit, said to be first digitally computed trajectory and control optimisation. Figure from [19]

1.2. motivation and goal

While minimum-time optimisation can help to improve performances in sports, it has not been used much in physical sports so far. In motorsport it has been used extensively. Can we alter and apply the methods used in motorsport to use them on cycling? In an ideal case, the racing line and acceleration/deceleration behaviour for a certain course can be found to train elite cyclists with. This is interesting, as Reijne et al have shown that racing lines differ quite a bit between

professional cyclists, specifically during a descent [51]. Furthermore, theoretical changes to the bicycle and driver can be analyzed without any risk of falling and injury. The cyclist could be modelled as a motor vehicle, where the "motor" consists of all propelling factors. During a descent, the main propelling factor is gravity, and the anaerobic capacity is left intact. This means that optimal pacing is not of much interest, and out of the scope of this project. A minimum-time optimisation could help improve the performance of cyclists to new extents. Therefore the goal for this project is the following:
to build a free-trajectory minimum-time optimisation model for the descent of elite cyclists.
There are two main challenges that arise from this goal: (1) applying free-trajectory minimum-time optimisation on cycling, and (2) transferring the model from 2D to 3D to create a general model that can be used for a descent scenario.

1.3. state of the art

In literature, several different approaches for minimum-time optimisation can be found. Over time, new possibilities came about, as a result of the development of computers. In this section, an literature overview is given on all the topics in which choices are faced when solving a minimum-time optimisation problem. The majority of the information is also presented in the literature study on optimal control approaches for minimum-time optimisation in sports, by the author of this thesis. The reader is invited to request the literature study from the author [1].

1.3.1. fixed vs free trajectory

In practise, there are two main methods used for minimum-time optimisation. The quasi steady state (QSS) approach, and the transient optimal control problem (OCP) approach. The first minimum-time optimisations were done following the QSS approach, the transient OCP approach has been used since the start of the new millennium [16]. Both the QSS approach (e.g. [11, 19, 65]) and transient OCP approach (e.g. [4, 16, 23, 31, 52, 61, 66]) are still widely used. The current state of the art approach combines those two categories and benefits from both their advantages (this is illustrated in figure 1.2) [48]. Another method is the fixed trajectory OCP, that is used to determine optimal pacing strategies for athletes (e.g. optimal pacing strategies for cyclists: [22, 38, 69]).

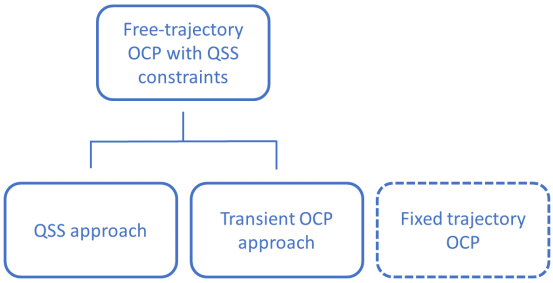

Figure 1.2: An orderly overview of minimum-time optimisation approaches

quasi steady state approach-
In this approach a predetermined trajectory is taken. This trajectory may come from data of the fastest driver or athlete taken during a top level race. It can also be a specific height profile (e.g. for cycling), or a route predefined for the competition.
In vehicle sports the approach is to first find the apex. An apex is the location in a turn where the lateral acceleration is maximal [48]. It is often assumed to be located to be at the part of the turn that has the largest curvature. Here, the velocity of the vehicle is assumed to be the lowest. Between these low velocities control strategies are developed to achieve the highest average speed in between. To do so, an initial guess of the states is used to calculate the optimal controls (the accelerations), and the states are updated using the results. This is iterated until the states have settled. The state equations are steady state equations of motion, which do not take into account time dependencies and response time [11]. It is assumed that the steady state is reached instantly. In this thesis, the motion that results from this assumptions is referred to as steady motion. As a final result, lateral and longitudinal accelerations or power output at each (discretised) point are found.
The benefit of this method is that the calculations are relatively simple. The downsides are the inaccuracy of the results if the apexes are incorrect, the less accurate representation of the dynamics due to the steady motion assumption and the large amount of iterations necessary to find a steady solution.

[1] e-mail address: astridvdniet@outlook.com

transient OCP approach-
In a free-trajectory approach, the goal is to find optimal trajectory and optimal controls simultaneously. It is done by describing the fully dynamic model as a set of first order differential equations. In practise, the transient OCP approach often involves many degrees of freedom [52]. This makes the computations complex.
The benefit of this method is that the trajectory is found, so that no further data acquisition and analysis of for example driver data is needed. The downside is that the calculations can be complex and computationally expensive.

free-trajectory OCP with QSS constraints-
Every minimum-time problem in which the trajectory still has to be determined (free trajectory) was solved using a fully dynamic model. Until last year. Then, a new approach was suggested [48]. This approach is a combination of the QSS approach and the transient OCP approach. It describes an optimal control problem, but the state equations do not describe the full equations of motion of the vehicle. Instead, they describe a simple model that shows how inputs are related to positioning and movement on the road. The complex vehicle dynamics are taken into account via one constraint: a g-g diagram. An example of a g-g diagram can be found in figure 1.4. A g-g diagram describes the limits of acceleration. The name comes from the gravitational acceleration, that is indicated with the letter 'g'. The diagram shows the limits of acceleration divided by g in two directions, hence g-g diagram. This way, the diagram is the same regardless of the use of imperial or metric units. The concept has been used academically since the 1970's [60].The g-g diagram is composed using quasi steady state equations and tire models, and describes the vehicle performance. This model takes the best of both worlds. Because most of the vehicle dynamics are taken into account implicitly through the constraint, only a few states are solved in the OCP. This means that computational effort is relatively low, while having the possibility of solving for the trajectory. Therefore, the free-trajectory OCP with QSS constraints approach is used for this project.

1.3.2. 2D vs 3D

In literature, only two studies have undertaken minimum-time optimisation while accounting for a 3D track and the dynamics that it imposes [24, 45]. The study by Leonelli and Limebeer shows that inclusion of 3D effects like banking (lateral slope of a road) can result in lap-time differences of 5% for relatively flat tracks, see figure 1.3. The largest effect is seen for turns with a large banking angle and a small turn radius. Here, the normal force is high, increasing the friction force such that turns can be driven with higher speeds. Since mountain roads almost solely have turns with a small radius and large banking angle, it is important to include banking effects in the minimum-time optimisation model. Of course, forward elevation is also a crucial 3D effect that should definitely be considered, because of the extra propulsion provided by gravity.

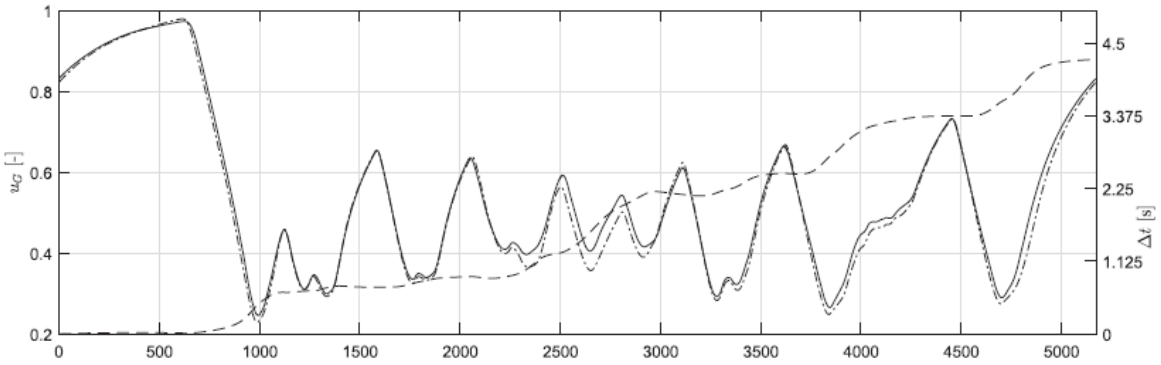

Figure 1.3: Comparison between 2D and 3D simulation. The dash-dot line represents the speed in the 2D simulation, the solid line represents the speed in the 3D simulation. The dashed line represents the build up of the lap-time difference. Figure from [45]

1.3.3. OCP solving methods

As the minimum-time optimisation approach that is chosen makes use of optimal control problems, it is necessary to determine which solving method can be used. Both indirect and direct methods can be used. With the indirect or variational approach, Lagrangian or Hamiltonian formalism is employed to convert the control problem to a (two-point) boundary value problem following the Pontryagin Maximum Principle explicitly [16]. The indirect method requires an estimation of the solution that is already fairly accurate. Such estimations are scarce, as data acquisition of the accelerations of cyclists is scarce. Furthermore, control history is assumed to be continuous. This is a problem, specifically for the case of a cycling descent, as switching from acceleration to braking can happen rapidly and discontinuously. Therefore, the indirect method is nearly impossible to use for this specific case. Another method, the direct method, is applied. The direct method converts the OCP into a non-linear programming (NLP) problem. In this method the time-dependent (or space dependent) unknown variables are approximated by parametrised equations. Then, parameters are treated as

optimisation variables and the problem is transcribed to an NLP [49]. There are various NLP solvers available to receive a solution. In this project, IPOPT (Interior Point OPTimiser) is used as it is freely available and implemented in popular optimisation applications. In a Hock-Schittkowski benchmark test it is close to the fastest solver available [40].

1.3.4. online versus offline

Minimum time optimisation is mostly used to find an offline solution, opposed to an online solution [28]. An online solution is found and updated while the control takes place, during a race or on the road. Most minimum time optimisations are computationally expensive and take a long time, so they cannot be deployed online. While the utility of offline solutions is great, sometimes online and real-time solutions are necessary, due to rapidly changing scenarios. For instance, if the racer is not able to follow a previously calculated path, how should it recover? In practise, not many successful online minimum time optimisations exist so far [27, 64]. Since optimal path finding is new for cycling, the first goal is to find an offline solution. Online solutions can be the next step.

1.4. approach

The approach as suggested by Veneri and Massaro was chosen to work with: a free-trajectory OCP with QSS constraints [48]. As control inputs lateral and longitudinal accelerations are used, instead of the standard bicycle control inputs (steering, leaning, pedalling/braking). As the lateral (stabilisation) dynamics are not of interest, steady motion is assumed. The g-g diagram expresses the steady motion constraints for the inputs. A g-g diagram describes the maximum lateral and longitudinal accelerations possible for a certain vehicle driving at a certain speed. Implicitly it describes all of the steady motion vehicle dynamics as well as tire dynamics within one figure. Such figures are a standard within motor sports for describing vehicle performance, hence the synonym 'performance envelope'. An example can be seen in figure 1.4.

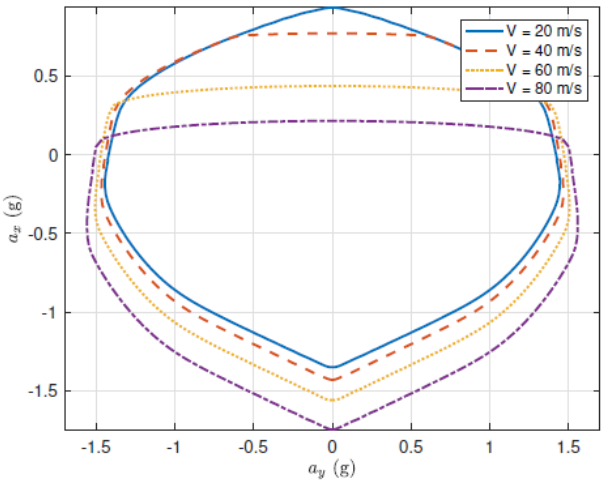

Figure 1.4: An example of a g-g diagram of a race car. A standard way to look at the diagram is through polar coordinates. The angle starting from the positive a_y axis is called the adherence orientation α (anti-clockwise rotation is positive). The corresponding acceleration limit is called the maximum adherence radius, r_{max}. The magnitude of any combination of lateral and longitudinal acceleration is referred to as the adherence radius r. Figure from [48]

The optimisation variables are speed, lateral track position and the orientation with respect to the track. This way, the movement of the cyclist is directly related to the track geometry. The optimisation constraints are listed below:

- the cyclist is constrained to move between the left and right track boundaries.
- the g-g diagrams constrain the inputs (accelerations).

The optimisation objective is to minimize time, therefore the cost function is simply the time cost to ride the track from start to finish line.
Because it is the objective to model a descent, a 3D track geometry description will be used. As this project is a first exploration into combining g-g diagrams and 3D road effects, the focus will be on producing an offline model.

1.5. reading guide

In chapter 2, the model description and the optimal control problem will be described. The g-g diagram, the most important constraint of the OCP, is described in chapter 3. The constraint equations for the g-g diagram are gradually build up,

forming a non-linear programming problem. A solving approach for the NLP is proposed. In chapter 4, the g-g diagram model is analysed for parameter sensitivity. A case study of the L218 mountain road in Vossenack, Germany, is presented in chapter 5. Finally, the discussion, recommendations and conclusion about the presented free-trajectory steady motion model are discussed in the last chapters.

2

Optimal Control Problem

The goal is to determine the optimal accelerations of a cyclist during a descent. This is done through a minimum-time optimisation for a 3D road. To be able to describe vehicle movement on a 3D road, first a track model needs to be defined. For this project, a ribbon road model is used. Then, state equations are set up for a cyclist moving over this ribbon road. Finally, the complete optimal control problem is formulated.

2.1. track description

Since the movement of the cyclist is (assumed to be) constrained to the road, it is important to define a road geometry description. There are several ways to model a 3D track. One well known way to do this is using B-splines. This is often used for road tracking in automated driving. However, b-splines describe only the road boundaries, and say nothing about the space in between. In the case of minimum-time optimisation, the orientation of the cyclist in space is important. Therefore, a ribbon is used to model the road. The benefit of a ribbon is that it is build up out of a chain of planes, so that the orientation of the road is known. A ribbon road assumes that there is no lateral curvature. Thus, lateral curvature is not taken into account when using the ribbon model.

2.1.1. curve geometry

A ribbon is an extended space curve. A space curve is a point set x in space $\mathbb{R}^3$ that can be split into subintervals that can be described by ($r \geq 1$) differentiable functions [44].

$$\mathscr{C} = \{\boldsymbol{x}(s) = [x(s), y(s), z(s)] \in \mathbb{R}^3 : s \in [s_0, s_f]\} \tag{2.1}$$

The distance over the curve is defined as s. At every s, a right handed coordinate system can be defined. In literature this is often called a moving trihedron [32], here it will be referred to as the curve frame $\mathcal{C}$ (see figure 2.1). The frame consists of the unit vectors $\boldsymbol{t}, \boldsymbol{p}$ and $\boldsymbol{b}$. $\boldsymbol{t}$ is the tangent vector to the curve. The direction of $\boldsymbol{t}$ depends on the direction of movement over the curve, indicated by an increasing value of s. Principal normal vector $\boldsymbol{p}$ points towards the center of the osculating circle. The osculating circle can be seen as the best circle that approximates the curve at a certain location s [34]. The plane in which the circle resides has the fitting name 'osculating plane' (osculare is latin for kissing). The distance from the center of the osculating circle at s to the point on the curve at s is called the radius of curvature ρ. Often, the inverse of the radius of curvature is used. This is called the curvature, κ. The binormal vector $\boldsymbol{b}$ is the cross product $\boldsymbol{t} \times \boldsymbol{p}$. It is therefore normal to the osculating plane.

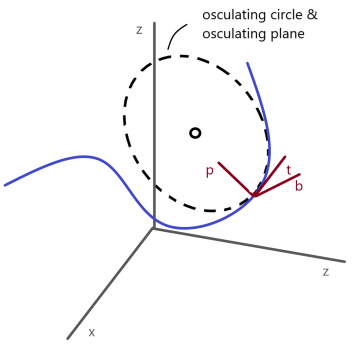

Figure 2.1: A space curve with the curve frame $\mathcal{C}$.

2.1.2. ribbon geometry

A ribbon or a strip can be seen as a curve in space, that has been expanded with a width and twist [32]. The ribbon has a spine, which can be the center line in the road. The ribbon is then built up out of planes tangent to the spine, ensuring that lateral road curvature is not present (figure 2.2). The entire ribbon can now be described with help of the notions curvature κ, torsion τ and twist β. Curvature describes the curving of the spine in the osculating plane. Torsion describes the extent to which the curve deviates from its osculating plane. With twist, camber can be described. The camber vector $\boldsymbol{n}$ lies in the plane normal to the tangent vector $\boldsymbol{t}$ of the spine. In this project, the direction of the camber vector is chosen

such that it always points to the right side of the road. The camber vector is rotated with a twist angle β with respect to the principal normal $\boldsymbol{p}$ [1]. Together with the tangent vector and a ribbon normal vector $\boldsymbol{m}$, a trihedron moving over the ribbon is defined. This is the ribbon frame $\mathcal{B}$.

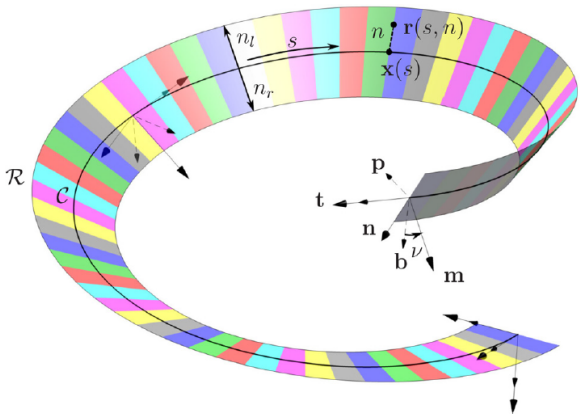

Figure 2.2: A ribbon generated by a spine curve C. The spine describes torsion and curvature, camber is described via twist angle $\beta(s)$. Figure from [32]

A different way to describe the orientation of a single plane of the ribbon is through Euler angles. Those will be used later on, as it is an easy manner to describe elevation and banking with respect to the inertial frame. For the complete parametrisation of a ribbon plane three Euler angles are needed. However, the direction of the center line within the xy plane is not necessary for further calculations. We will see later on, that only the relative orientation with respect to gravity matters. Therefore, only two angles are introduced, ψ and γ. ψ describes the angle between the tangent and the xy plane of the inertial frame $\mathcal{N}$, or forward elevation. γ describes the angle between the camber vector $\boldsymbol{n}$ and the xy plane rotated by ψ, or banking. The Euler angles are represented corresponding to the right handed coordinate system.

2.2. model description

The goal is to build a free-trajectory minimum-time optimisation model for the descent of elite cyclists. In such situations, forward elevation is one of the main propelling factors. Banking is often positive [2] and can cause a higher normal force. Therefore it is important to describe these road aspects and take them into account. The ribbon geometry is used to describe the 3D road. The cyclist is constrained to move over this ribbon surface. A bicycle with a cyclist is a complex system, the bicycle itself consists of multiple rigid bodies that are connected through hinges [42]. For the sake of simplicity, in this model the cyclist and bicycle are together regarded as a single rigid body that moves over a ribbon surface. The number of degrees of freedom can be found when looking at movement constraints.

1 body	1 ×6	=	6	coordinates
2 contact points	2 ×1	=	2	coordinate constraints
	total	=	4	independent coordinates

The independent coordinates together describe the location of the center of mass and the orientation of the rigid body in space. The location of the cyclist in space can be described with two variables. Variable s describes the distance over the center line of the ribbon. Variable n describes the lateral offset from s in the ribbon plane. The rigid body moves over the ribbon surface, so it is constrained in height. The orientation of the cyclist can be described with two variables. χ describes the orientation of the cyclist with respect to the center line, in the ribbon plane. ϕ describes the roll angle of the cyclist around its longitudinal axis. As part of the minimum-time optimisation approach, steady motion is assumed. In the case of cycling, this specifically means that the roll angular acceleration is assumed to be zero. This results into ϕ not being a free variable. Instead, it depends on the other variables and the local track geometry. Therefore the accessible configuration space is three-dimensional and can be described through the configuration variables:

$$\boldsymbol{x} = (s, n, \chi)^T \tag{2.2}$$

This is illustrated in the boxed page "Bicycle orientation: step by step". The velocity variables are commonly found through differentiating the configuration variables. However, the speed of the cyclist projected over the center line $\dot{s}$ is

[1] β ranges from -0.5π to 0.5π. The other possible values of β are mirrored into this range, for those values the corresponding curvature for that point s becomes negative. This is done to still receive the correct values for $\dot{\beta}$, for our definition of the camber vector

[2] banking is called positive when the outside of the road in a turn is higher than the inside of the road.

not very interesting. More interesting is the speed of the cyclist in its own direction, v, as it shows directly what the cyclist does. With v, the speed at the contact point of the wheels with the ground is meant, not the speed of the CoM (Center of Mass). This is done as a simplification, that is further discussed in section 2.3 and appendix B. Furthermore, the derivative of n can be described using the other variables: $\dot{n} = sin(\chi)v$. Therefore, $\dot{n}$ is not an independent variable. That means that the state vector can be given by:

$$\boldsymbol{x} = (s, n, \chi, v, \dot{\chi})^T \tag{2.3}$$

As control inputs there are a_x and a_y, that describe the absolute longitudinal and lateral acceleration of the center of mass respectively. The acceleration is expressed in the driving frame $\mathcal{D}$, so that the direction of a_x is longitudinal to the cyclist and a_y lateral along the ribbon plane. Those are the only inputs that the cyclist gives to the motion. The accelerations together describe change of orientation, and change of speed. a_z is not (always) zero, but depends on the input and track variables.

$$\boldsymbol{u} = (a_x, a_y)^T \tag{2.4}$$

The acceleration limits can be described through a g-g diagram (more about the g-g diagram can be found in chapter 3). It is assumed that any acceleration within the diagram can be carried out in any sequence. Due to the simplification of the model of the bicycle and rider, bicycle characteristics like counter steering and weave are not represented in the model. From acceleration inputs, actual cycling inputs like lean and steering can be determined.

Bicycle orientation: step by step

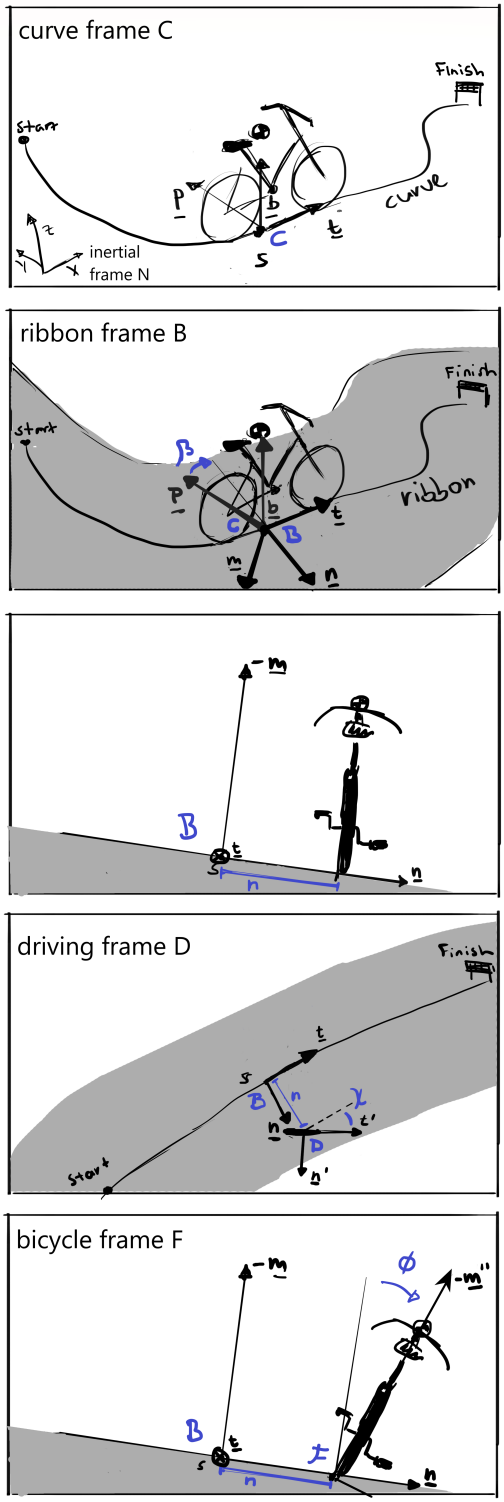

The bicycle is positioned on a curve at a certain distance over the curve s. At its location a curve frame $\mathcal{C}$ is defined, which depends on the geometry of the curve. If the curve is taken as the center line of a ribbon, a road with a certain width can be seen as a ribbon. The road does not have lateral curvature. The ribbon frame that corresponds with it is twisted around the tangent vector with respect to the curve frame by twist angle β. The cyclist can have a lateral position with respect to the center line as well, n. Lateral translation over the ribbon has the direction of the ribbon vector $\boldsymbol{n}$. s and n together determine the position of the center of mass of the bicycle/rider combination. A rotation χ around the moved ribbon normal vector $\boldsymbol{m}$ creates the driving frame $\mathcal{D}$. In this frame we want to know the accelerations, as this frame indicates the longitudinal and lateral directions with respect to the cyclist. Finally, to know the orientation of the cyclist roll (ϕ) is necessary as well. The frame that moves with the cyclist is called the bicycle frame $\mathcal{F}$. Now, the position and orientation of the cyclist on the ribbon can be fully described. This can be done through adding three position vectors.

$$\boldsymbol{r}_{CoM/N} = \boldsymbol{r}_{C/N} + \boldsymbol{r}_{D/C} + \boldsymbol{r}_{CoM/D} \tag{2.5}$$

The first vector from the origin of $\mathcal{N}$ to the origin of C.

$${}^{N}\boldsymbol{r}_{C/N} = \begin{bmatrix} x(s) \\ y(s) \\ z(s) \end{bmatrix} \tag{2.6}$$

The second describes the lateral position with respect to the center line, pointing from $\mathcal{C}$ laterally in the camber vector direction to the origin of $\mathcal{D}$.

$${}^{N}\boldsymbol{r}_{D/C} = {}^{N}\mathbf{R}_{B} \begin{bmatrix} 0 \\ n \\ 0 \end{bmatrix} \tag{2.7}$$

The third vector describes the position of the CoM with respect to the origin of frame $\mathcal{D}$, through the roll angle.

$${}^{N}\boldsymbol{r}_{CoM/D} = {}^{N}\mathbf{R}_{F} \begin{bmatrix} 0 \\ 0 \\ h \end{bmatrix} \tag{2.8}$$

2.3. optimal control problem formulation

Now that it is clear what the control inputs and the state variables are, a connection should be made between the two. The transport theorem can be used to find the state equations conveniently, as the motion can be build up out of relative rotations. Since the control inputs are directed longitudinally and laterally with respect to the cyclist, the $\mathcal{D}$ frame is fit to describe them.

$$ {}^{D}(\boldsymbol{a})_{N} = {}^{D}(\dot{\boldsymbol{v}})_{D} + {}^{D}\boldsymbol{\omega}_{D/N} \times {}^{D}\boldsymbol{v} \tag{2.9} $$

$$ \begin{bmatrix} a_x \\ a_y \\ a_z \end{bmatrix} = \begin{bmatrix} \dot{v} \\ 0 \\ 0 \end{bmatrix} + {}^{D}\boldsymbol{\omega}_{D/N} \times \begin{bmatrix} v \\ 0 \\ 0 \end{bmatrix} \tag{2.10} $$

Figure 2.3 illustrates how the basis rotation that takes place when riding over the center line can be altered through changing state variables like the relative orientation χ. The red axis displays the direction of the combined angular velocity vector ${}^{D}\boldsymbol{\omega}_{D/N}$.

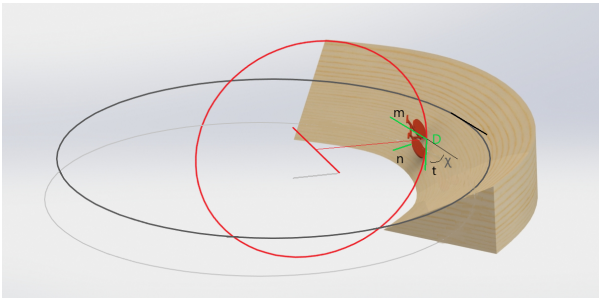

Figure 2.3: A possible configuration of a cyclist on a track. The grey circle depicts the osculating circle at location s on the center line. The red circle depicts the osculating circle for the cyclist's motion. Note that direction of the instantaneous axis of rotation differs from the direction of the unit vector normal to the ribbon.

The goal is to find relations between the state variables and the inputs, but not all the state variables are present in equation 2.3. Or are they? The angular velocity of frame $\mathcal{D}$ with respect to frame N is affected by three different angular velocities: the absolute angular velocity of the center line of the track, the angular velocity of the twist, and the angular velocity of the cyclist with respect to the center line. We can write the angular velocity vector $\boldsymbol{\omega_{D/N}}$ as a sum of angular velocities:

$$ \boldsymbol{\omega}_{D/N} = \boldsymbol{\omega}_{C/N} + \boldsymbol{\omega}_{B/C} + \boldsymbol{\omega}_{D/B} \tag{2.11} $$

Here $\boldsymbol{\omega_{C/N}}$ can be seen as the angular velocity that is the result of moving over the center line. $\boldsymbol{\omega_{B/C}}$ can be seen as the twist angular velocity of the ribbon frame with respect to the curve frame, and $\boldsymbol{\omega_{D/B}}$ is the angular velocity of the driving frame with respect to the ribbon frame, that is a result of the change of the angle χ. The expressions for those angular velocities involve the state variables, making it clear how the inputs and state variables are related.

$$ {}^{D}\boldsymbol{\omega}_{C/N} = \frac{\dot{s}}{\rho} {}^{D}\mathbf{R}_{C} {}^{C}\boldsymbol{b} \tag{2.12} $$

And the twist angular velocity can be described as such:

$$ {}^{D}\boldsymbol{\omega}_{B/C} = \dot{\beta} {}^{D}\mathbf{R}_{B} {}^{B}\boldsymbol{t} \tag{2.13} $$

Finally, the angular velocity of the $\mathcal{D}$ frame with respect to the $\mathcal{B}$ frame that is caused by a change in the relative orientation χ can be expressed in the following way:

$$ {}^{D}\boldsymbol{\omega}_{D/B} = \dot{\chi} {}^{D}\boldsymbol{m} \tag{2.14} $$

When the cross product from 2.10 is combined with equation 2.11, an new expression for the cross product is found:

$$ \boldsymbol{\omega}_{D/N} \times \boldsymbol{v} = \boldsymbol{\omega}_{C/N} \times \boldsymbol{v} + \boldsymbol{\omega}_{B/C} \times \boldsymbol{v} + \boldsymbol{\omega}_{D/B} \times \boldsymbol{v} \tag{2.15} $$

with the help of this expression, a scalar representation can be found for $\dot{v}$ and $\dot{\chi}$. See appendix A for elaborated calculations. For $\dot{\chi}$ expression 2.16 can be found. The first part of the expression describes the angular velocity caused by the lateral acceleration, the second part the angular velocity of movement over the center line. If they are equal, the curvature of the trajectory of the cyclist is the same as the curvature of the center line.

$$\dot{\chi} = \frac{a_y}{v} - \frac{\dot{s}}{\rho}\cos(\beta) \tag{2.16}$$

Here ρ stands for the radius of curvature of the center line of the ribbon at s, and β is the twist angle. Furthermore, $\dot{\chi}$ depends on $\dot{s}$. For $\dot{s}$, the expression by Perantoni was used [24]:

$$\dot{s} = \frac{\cos(\chi)\, v}{1 - \frac{n}{\rho}\cos(\beta)} \tag{2.17}$$

The projected speed is not simply the speed in the tangent direction of the road ($\cos(\chi)\, v$). Some compensation needs to be made for trajectory choices that lead to cutting corners, reducing the length of the cycle trajectory with respect to the length of the center line. If the cyclist rides more towards the inside of a turn, the radius of curvature of the cyclist is shorter than that of the center line. Therefore, the denominator corrects for this. This expression for β takes the 3D direction of road curvature into account. In a situation where a cyclist rides over the top of a hill, β has a value of $\pm 0.5\pi$. In this situation, the lateral position does not matter for the value of ρ. This is reflected by the formula.
Note that equation 2.17 gives a simplified expression for the projection of the speed of the CoM on the center line. With this expression, the velocity v has been treated as if the CoM is located in the center of the wheel contact points. This assumption is made more often in motorsports and cycling [7, 48]. In Appendix B this is described in more detail.

The state equation for v can be extracted from equation 2.10 when looking only at the tangent direction. Per definition, the direction of the angular velocity of the cyclist with respect to the inertial frame is orthogonal to the tangent vector when expressed in the $\mathcal{D}$ frame. This means that:

$$\dot{v} = a_x \tag{2.18}$$

and the last state equation is:

$$\dot{n} = sin(\chi)\, v \tag{2.19}$$

as this information is necessary to reproduce the exact trajectory and motion of the cyclist. Note that this description of $\dot{n}$ only portrays the location of the wheels, not of the CoM. As road width constraints should be applied the wheels, this is convenient for the constraint formulation.
Now how can we find the optimal result? The goal is to find the trajectory and accelerations that lead to fastest track time. Logically, the fastest time is cycled when the highest average projected speed is cycled. Therefore the objective is to minimize this cost function:

$$L = \int \frac{1}{\dot{s}} ds \tag{2.20}$$

subject to state equations 2.16, 2.18 and 2.19. Those state equations are formulated in the time domain, but the cost function is related to the space domain. To convert the state equations to the space domain, the expression for the projected speed can be used (equation 2.21).

$$\boldsymbol{x}' = \frac{d\boldsymbol{x}}{ds} = \frac{\dot{\boldsymbol{x}}}{\dot{s}} \tag{2.21}$$

To complete the OCP description, the path constraints need to be defined. The most important path constraint for this optimal control problem is the g-g diagram. It is implemented through comparison of the adherence radius r with the maximum adherence radius r_{max} (equation 2.22). The formulation of the g-g diagram constraint will be discussed in chapter 3. The second path constraint describes the road width from the center line (equation 2.23). If the road width is fixed, the path constraint can alternatively be implemented by bounding the variable n.

$$r \leq r_{max} \tag{2.22}$$

$$-n_{wl} \leq n \leq n_{wr} \tag{2.23}$$

3

The g-g diagram

The trick of a free-trajectory steady motion minimum-time optimisation, is to capture all acceleration limits in the form of a g-g diagram. In this chapter, a model that finds g-g diagrams will be constructed for a cyclist cycling on a road with a variable orientation with respect to gravity. First, the build-up of a g-g diagram will be discussed. Then, the models and theory that are needed for the composition of the g-g diagram are reviewed. Finally, a solving approach is suggested to find the g-g diagram on the basis of those models.

3.1. build-up of the g-g diagram

A g-g diagram shows acceleration limits. Those limits can be found in several ways; experimentally, by recording accelerations and establishing which of them are the maximum accelerations that were experienced, or numerically. In the numerical method, theoretical acceleration limits are found with the help of models that describe the dynamics of the bicycle, the rider and its tires as well as the influence of the track and the environment on them. In this chapter, the numerical method will be used to establish a model that finds g-g diagrams for a cyclist, moving in 3D.

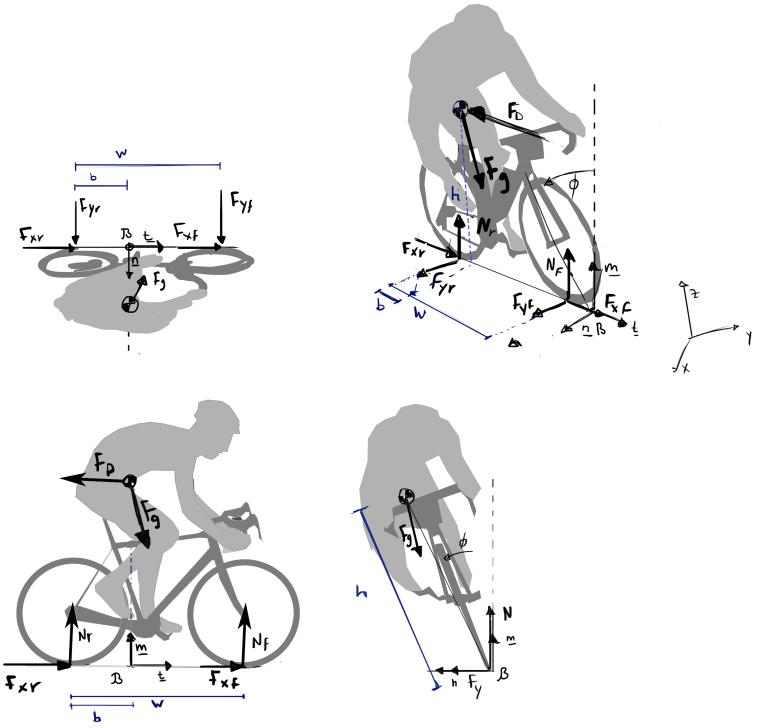

Figure 3.1: Free body diagram of a cyclist on the ribbon plane, modelled as a single rigid body. The isometric view is depicted in the ribbon frame $\mathcal{B}$. The views are projected on the tm plane, the nm plane and the tn plane. Measurements are depicted in blue.

To find the accelerations, the external forces working on the cyclist should be analyzed. Looking at the Free Body Diagram (FBD) in figure 3.1 there are several kinds of forces working on the cyclist. There are ground contact forces, that prevent the cyclist from slipping. Then a propelling force caused by pedalling and a drag force working against it. The direction of the gravitational force is dependent of the orientation of the road, and can either work with or against the cyclist. Lastly, there are normal forces keeping the cyclist on the track. All those forces can cause moments as well. The g-g diagram describes acceleration limits; thus, also force limits. For the ground contact forces, this translates into the maximum forces that can be applied on the tires before they start to slide (losing control). The tire force limits can be translated into lateral and longitudinal acceleration limits and form a basic shape for the g-g diagram. Figure 3.2 shows a few examples of how this may look.

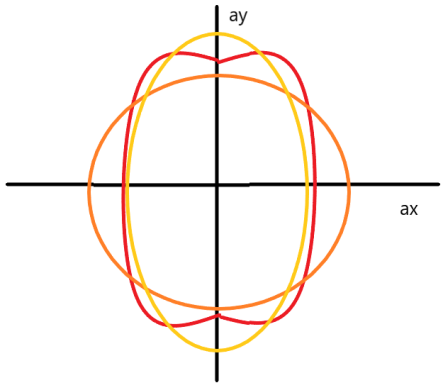

Figure 3.2: Examples of acceleration limits based on tire force limits. The shapes come from different models (red is from Pacejka's magic formula, yellow and orange the friction ellipse).

These shapes give the absolute maximum lateral and longitudinal accelerations for the cyclist. The other forces and moments may reduce this shape further, but can never extend them. There are three effects that can 'cut' the g-g diagram into shape.

- the propulsion limit
- the stoppie limit
- the braking limit

The typical shapes of those limits are shown in figure 3.3. The resulting g-g diagram is shown as well. Next, the limits will be explained in more detail.

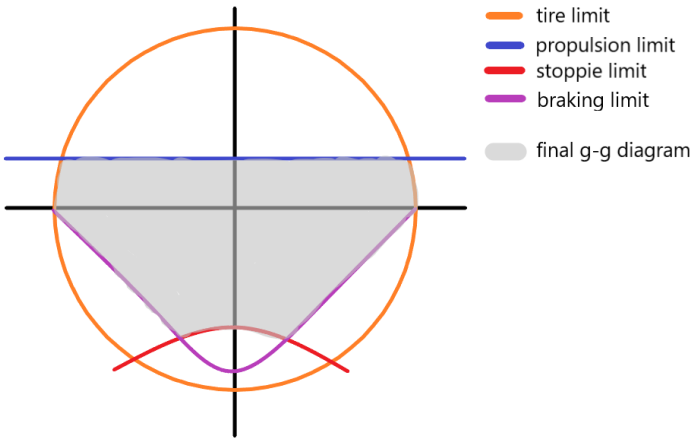

Figure 3.3: The typical shapes of the different acceleration limits that a cyclist experiences. The magnitudes and positions can change, but the shape of the diagram will be symmetrical. The braking limit shape is shown for the 'front brake only' strategy, the optimal braking limit follows the shape of the tire limit instead.

The propulsion limit is caused by the sum of all propelling and resisting forces; air drag, the force output of the cyclist based on the applied power and the part of gravitation that works in the longitudinal direction of the cyclist. It cuts the upper part of the g-g diagram.

A stoppie is an event in which the rear wheel loses ground contact. This can lead to the cyclist falling over the steering wheel. It has a higher risk of occurring during a descent, as the moment arm of the CoM to the front wheel ground contact point is larger in that configuration. A stoppie can be especially dangerous during a descent, when high speeds are reached.

The braking limit is a shape that forms through the application of a certain braking strategy. Examples of strategies are 'front brake only' and 'optimal braking'. The first strategy is the standard strategy for elite cyclists. Using the front brake while braking has much more effect than using the rear brake because there is a lot of load transfer to the front wheel during braking. The risk it brings is that of a stoppie. The second strategy is the optimal braking strategy. In this strategy, the optimal braking ratio is applied. What is the optimal braking ratio? According to Biral, it is when the front and rear tire work at the maximum combined adherence limit [29]. That occurs when the rear and front wheels are equally engaged, i.e. $F_{xr}/N_r = F_{xf}/N_f$. It means that in total, the theoretically maximum available deceleration is reached. However, in another study the found effect of combined rear and front wheel braking compared to front wheel brake only was small [47]. There was only a 300 ms difference while attempting to stop a race motorcycle driving nearly 300 km/h. Because of the load transfer to the front wheel, the rear wheel does not contribute much. It should be considered however that this study did not include slopes, and they can make a large difference.

As a conclusion, the basic shape of the g-g diagram is based on tire forces. Therefore, the first step towards building a g-g diagram is to establish a tire model, that determines the outer shape of the g-g diagram. After that, the extra limits that other forces cause can be found with the steady motion equations. They are found step-by-step, to build-up the complexity gradually. Finally, a solving approach to find the total g-g diagram numerically is proposed.

3.2. the basis: tire forces

To find the maximum possible accelerations that can be experienced without losing control or falling, we need to know what the maximum possible forces are. The contact forces with the ground play a big role. They depend on tire characteristics. That is why it is important to understand tire characteristics and to choose an appropriate tire model. When this basis is established, other conditions that influence the diagram can be analyzed.

3.2.1. tire characteristics

Tires have a large influence on vehicle dynamics. They are the contact between the bicycle and the ground. Tires affect vehicle handling, traction, and friction forces. They are complex, due to their non-linear material dynamics that differ with temperature and use (load cycle frequency), that act even stranger due to the threading of the tires. There exist many different tire models, that are based on experiments or theory [56]. Most are made specifically for car tires. They take into account certain tire properties, and neglect others. Therefore it is fundamental to know which tire properties bicycles have, and how they differ from car tires and motorcycle tires. In this section, the tire characteristics are discussed that are relevant for choosing a tire model.

friction coefficient-
The friction coefficient describes the interaction between the ground and the tires. Finding out what the coefficients value is for a specific situation is complex due to the complex material characteristics of tires. It differs with tire wear and ground surface (think of weather conditions, road quality, the presence of sand). One effect of the non-linear material behavior is the hysteresis effect that rubber experiences in a load cycle. Due to this effect, energy is lost. The energy loss is commonly described with the term 'rolling resistance'. Mostly, rolling resistance is described with a force that represents the energy loss.

contact patch-
The area where a tire makes contact with the ground is called the contact patch (illustrated in figure 3.4. It can be divided into adhesion and slip areas. Part of the tire sticks at a certain moment in time to the ground, while another part slides over it. Which part sticks and which part slides depends on the geometry of the tire, the ground and the pressure distribution.

slip angle-
When the direction of travel differs from the direction the wheel points in, the angle between those directions is called the slip angle. When a slip angle is present, there is a lateral tire force. This force is also called the cornering force. The relation between the slip angle and the cornering force is described by a coefficient called the cornering stiffness. For low

slip angles, the cornering force is linearly proportional to the slip angle. It is directed perpendicular to the mid-line of the tire and lies in the road plane.

longitudinal slip coefficient-
This describes the difference of the free rolling wheel angular velocity, and the actual angular velocity. If the magnitude of the slip coefficient is equal to or larger than one, then sliding occurs (pure slip).

relaxation length-
The delay between the initialization of a slip angle and the lateral force generation due to this slip angle reaching its steady-state is called the relaxation length [25]. It is not a time constant but a length, that can be seen as the tire rolling distance until 63% of the steady-state lateral force is reached [17]. It is mainly influenced by velocity, but also by tire pressure and load. The relaxation length is an important predictor of wobble.

camber stiffness-
Camber stiffness describes the rate of change of the lateral force (also thrust force) that is generated perpendicular to the direction of travel of the tire, due to a camber or roll angle. The wheel wants to travel in an elliptical path due to the inclination, but cannot due to friction that is caused by the deformation of the tire (this is illustrated in figure 3.4) [17]. The lateral force that is generated is located before the center of the contact patch, and therefore generates a torque as well. For bicycles and motorcycles, the thrust force can contribute greatly to the centripetal force that is necessary to make a turn.

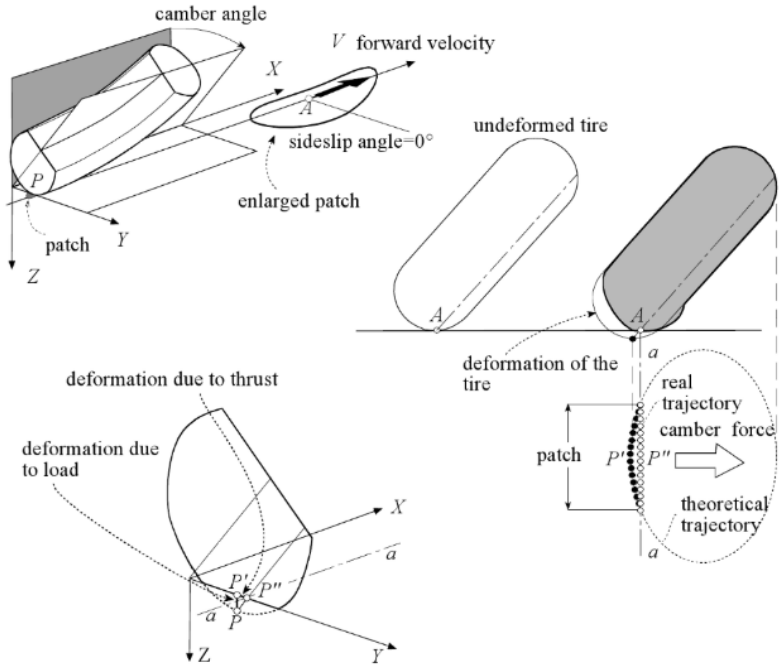

Figure 3.4: Illustration of the a-symmetric contact patch and the difference between the theoretical and real trajectory of the tire, that generates the lateral force. Figure from [17]

3.2.2. tire models

With the help of tire models it is possible to determine the maximum combination of forces that a tire can handle before it starts to slide. This in turn has a great influence on the maximum cornering speed and the vehicle trajectory. Not many studies have been conducted about bicycle tire properties (the efforts of Dressel and Doria are the only studies found [1–3, 26]). No actual bicycle tire models have been designed, while there are numerous models for car tires [25]. However, cars are very different from bicycles. One of the main differences is that they do not roll as much as a bicycle. Therefore, camber forces are less relevant and almost never taken into account in car tire models. There are also several motorcycle tire models available. Since the motion and forces they experience are comparable to bicycles, they could be an option to use for bicycles as well. There are also some important differences, that indicate that bicycle tire models could be significantly different from motorcycle tire models:

- The shape. A tire of a bicycle is relatively thin, and thus has a very elongated contact patch.
- The pressure in bicycle tires is much higher than in motorcycle tires. This gives differences in the contact patch, relaxation length, camber stiffness and cornering stiffness.
- The load on the tire is much lower for bicycles than for motorcycles, affecting for example camber stiffness.

- The tire type does sometimes differ: bicycles have bias ply tires, and motorcycles (especially racing bikes) often have radial tires. This affects the lateral force generation [8].

From this it can be concluded that motorcycle tire models can probably describe bicycle models in the most accurate way. Still, there are many differences. In the next sections three very different models will be discussed. One is a brush model, an analytical model that is based on simplified physical assumptions. Because it is based on simplified general physics, it's findings are as valid for cars as they are for bicycles. The other two discussed models are an often used empirical motorcycle tire model (the Pacejka magic tire formula for motorcycles) and a basic model that is based on observations, the friction ellipse.

brush model with static and kinetic Coulomb model of friction-
This model was developed to relate *longitudinal* forces and *longitudinal* slip [50]. Lateral tire dynamics are not taken into account. A brush model presents the tire tread patterns by elastic brush elements attached to a belt, which is modelled as an elastic beam. The brush elements as well as the foundation of the belt have elasticity conditions that are specific for tires. The friction coefficient is modelled as sliding velocity dependent, namely as a Gaussian function of the logarithm of the sliding velocity. This function is visible in figure 3.5.

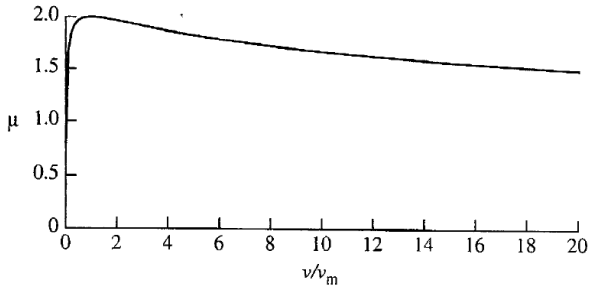

Figure 3.5: Friction characteristic for elastomers. v represents the sliding velocity, v_m the sliding velocity of maximum friction. Increasing the sliding velocity and decreasing the temperature have similar effects, as temperature only affects the sliding velocity variable. Figure from [50]

The biggest shortcoming of the model is that it does not include lateral relations, let alone a combination of longitudinal and lateral forces.

friction ellipse-
The most simple model to work with is the friction ellipse (figure 3.6). The idea is that a tire has two force limits in the lateral and longitudinal direction, and that maximum forces can't be practised in both directions at the same time. The maximum forces can differ between the directions, due to several influences. For example, a tire of a car has longitudinal threading. This makes the flexibility in lateral and longitudinal direction different, and therefore the dynamics of the tire as well. Also, the contact patch does not have the same length as width. An ellipse is then taken to describe the limits for force combinations, as it's two axes have different lengths just like the two different maximum forces. The maximum forces in longitudinal and lateral direction are defined as normal force times friction coefficient μ_x and μ_y.

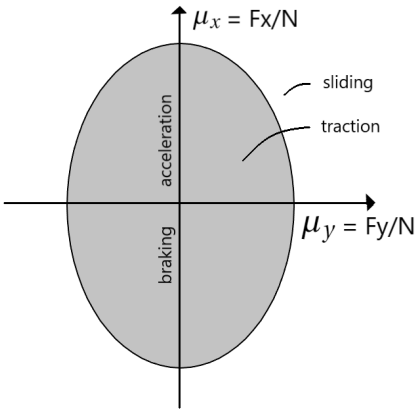

Figure 3.6: An example of a friction ellipse, the limits at the longitudinal and lateral directions are μ_x and μ_y respectively.

The model does not depend on the slip angle and traction slip and does not show nonlinear tire behavior. However, Acceleration measurements have confirmed that an ellipse is able to describe the general force limits [5, 29].

pacejka magic tire formula-
Pacejka has set up an empirical formula that describes the tire forces as a function of the slip coefficients, slip angle, friction coefficients, load and more parameters [56]. The model is fairly accurate for cars, and is widely used. In the magic formula, it is assumed that the camber angle or inclination angle of the tire is small. However, for cyclists, this angle is large because of the large roll movement a cyclist can experience. For motorcycles, large inclination angles are equally important. Pacejka has altered his magic tire formula for motor cyclists, to include large inclination angles. However, he does not seem to include the effect of roll that another part of the tire suddenly makes ground contact. The surface on the sides of a tire can have different friction coefficients. Furthermore, the tire certainly has a different contact patch and thus a different pneumatic trail. Lastly, the pressure distribution during roll is very asymmetrical in comparison to pressure distribution for car tires. Those factors are probably only a few of many. This is all not incorporated in the Pacejka motorcycle tire model. Still, Pacejka finds good results when comparing his empirical magic tire motorcycle formula with measurements. A comparison to bicycle tire performance measurements has yet to be made, but the expectation is that the inaccuracies mentioned above are even larger for bicycles.

tire model choice-
To keep calculations relatively simple, the friction ellipse model was chosen to work with. In literature, it is used more often to model motorcycle tires, and when comparing it with experimental data the shape seems appropriate when the lateral and longitudinal friction coefficients are assumed to be equal (a circle model) [5, 29]. For bicycles, there is no clear argumentation towards a different shape. Therefore the circular shape is adopted. The formula associated with the friction ellipse is described in equation 3.1.

$$\left(\frac{F_{xr}/N_r}{\mu_x}\right)^2+\left(\frac{F_{yr}/N_r}{\mu_y}\right)^2-1\leq 0 \tag{3.1}$$

To form a circle, μ_x equals μ_y.

3.3. the complexity of setting up steady motions equations

There are several aspects that make the equations of steady motion complex. First of all, the motion of the cyclist is build up out of various parts. This is illustrated in figure 3.7. Secondly, the orientation of the road constantly changes. If every local ribbon plane is seen as the reference frame, the orientation of gravity changes constantly.

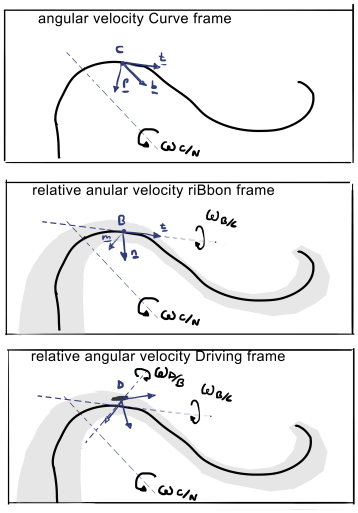

Figure 3.7: This figure illustrates how the different frames move with respect to one another. The possible accelerations of the cyclist will be expressed in the $\mathcal{D}$riving frame.

It is easiest to simplify the problem as far as possible and build up form there. The most simplified representation of a cyclist and bicycle is a point mass. A ribbon is an expanded space curve. Therefore, accelerations of a point mass moving over a space curve will be looked upon first. At the same time, formulas for the base vectors of the $\mathcal{C}$urve frame and the $\mathcal{D}$riving are presented. They are necessary to calculate the accelerations. Next, the space curve is seen as the center line of a ribbon, and the absolute accelerations are expressed in the ribbon frame. The following step is to transform the point mass into a rigid body. First, a point mass on a massless stick that can rotate around the tangent is considered. Finally, this is extended into a massless structure with two ground contact points, which represent the tire contact points.

3.4. step 1: a point mass moving over a space curve

To understand how accelerations on a bicycle riding over a ribbon work, it is convenient to first simplify the situation. The very basic of a ribbon is a curve. As a start, an expression for the accelerations of a point mass moving over a curve will be found. In the book 'differential geometry' by Kreyszig the relevant information can be found [44]. The derivative with respect to s is displayed through prime notation. Derivatives with respect to time are indicated through dot notation.
In chapter 2 it was discussed how the $\mathcal{C}$urve frame is built up. But how can the base vectors of this frame be found?
A unit vector tangent to the curve at a certain location is defined to have the direction of the change of the curve at that location. As a curve can be described with the variable s, the unit tangent vector can be described as a function of s.

$$\boldsymbol{t}(\boldsymbol{s}) = \boldsymbol{x}' \tag{3.2}$$

Next, the principal normal vector $\boldsymbol{p}$ needs to be found . $\boldsymbol{p}$ points per definition in the direction of change of $\boldsymbol{t}$.

$$\boldsymbol{p}(\boldsymbol{s}) = \frac{\boldsymbol{t}'}{|\boldsymbol{t}'|} \tag{3.3}$$

To conclude the curve frame a third unit vector, the binormal vector, can be found by taking the cross product of $\boldsymbol{t}$ and $\boldsymbol{p}$, $\boldsymbol{t} \times \boldsymbol{p}$. An example of the frame is seen in figure 3.8.

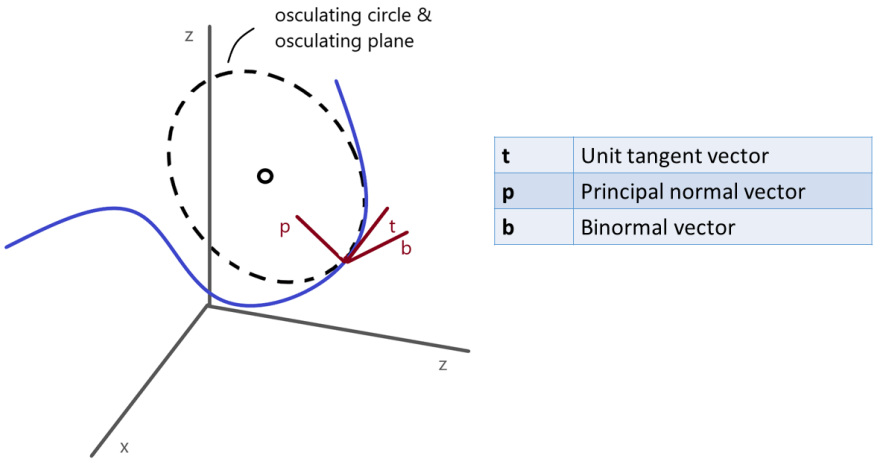

t	Unit tangent vector
p	Principal normal vector
b	Binormal vector

Figure 3.8: A space curve with the $\mathcal{C}$ frame

With the base vectors of the frame defined, the absolute accelerations of the point mass can be expressed more conveniently. The accelerations can be found using the transport theorem (general transport theorem displayed in equation 3.4). The vector $\boldsymbol{A}$ can then be seen as the velocity of the point mass moving over the curve.

$$(\dot{\boldsymbol{A}})_{\boldsymbol{N}} = (\dot{\boldsymbol{A}})_{\boldsymbol{B}} + \boldsymbol{\omega}_{\boldsymbol{B/N}} \times \boldsymbol{A} \tag{3.4}$$

The acceleration relative to the curve frame can only take place in the tangential direction. As this is the acceleration over the curve, it can be described by the term $\ddot{s}$. Since the movement happens over the curve only, the osculating circle that describes the local curve also describes the local movement. The angular velocity vector can therefore be described always having the direction of $\boldsymbol{b}(s)$. The magnitude is the tangential speed divided by the instantaneous radius of curvature ρ. The accelerations of the frame can now be described like this:

$$(\boldsymbol{a})_{\boldsymbol{N}} = \ddot{s}\boldsymbol{t}(s) + \frac{\dot{s}}{\rho(s)}\boldsymbol{b}(s) \times \dot{s}\boldsymbol{t}(s) \tag{3.5}$$

The cross product can be simplified to give the following expression:

$$(\boldsymbol{a})_{\boldsymbol{N}} = \ddot{s}\boldsymbol{t}(s) + \frac{\dot{s}^2}{\rho}\boldsymbol{p}(s) \tag{3.6}$$

The only unknown left is $\rho(s)$, since the acceleration over the curve and thus also the speed over the curve (the velocity of the point mass) are controlled by the rider.

$$\rho(s) = |\boldsymbol{t}(\boldsymbol{s}) \times \boldsymbol{t}'(\boldsymbol{s})| \tag{3.7}$$

With equation 3.6, the accelerations of the point mass moving over a space curve can be found with respect to the inertial frame.

3.5. step 2: a point mass moving over the center line of a ribbon

Our road is not a space curve. Instead it can be described as ribbon, with a space curve as its center line and a width. In this section expressions for the base vectors of the ri$\mathcal{B}$bon frame are first found. When those are established, the accelerations of a point mass moving over the center line of the ribbon can be described in terms of the ribbon frame. The difference between the $\mathcal{C}$urve frame and the ri$\mathcal{B}$bon frame is that the frame is twisted. The camber vector $\boldsymbol{n}$ that lies laterally along the road surface can be twisted with respect to the principal normal vector (see figure 3.9).

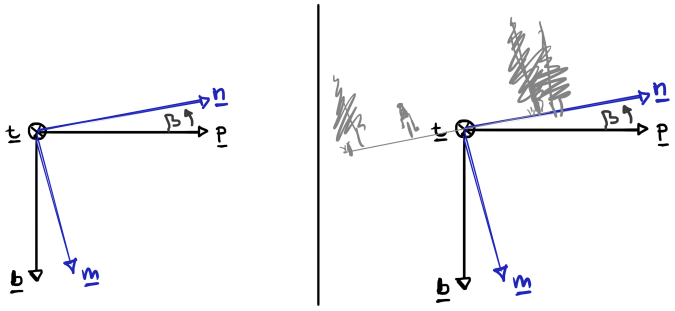

Figure 3.9: The ribbon frame $\mathcal{B}$ with is rotated by an angle β with respect to the $\mathcal{C}$ frame. On the right some environmental context is added, to help imagine how the frame is related to the road. The cyclist is seen from the back.

Now the absolute accelerations over the center line can be expressed in this new frame. To do so, the principal normal vector p needs to be expressed in terms of the $\mathcal{B}$ frame. This is simply done with help of a rotation matrix:

$$^{B}\boldsymbol{p} = {}^{B}\mathbf{R}_{C}\,{}^{C}\boldsymbol{p} \tag{3.8}$$

With this new expression for vector $\boldsymbol{p}$ the accelerations can be described in the ribbon frame (equation 3.9). The tangent vector expression is equal in frame $\mathcal{B}$ and $\mathcal{C}$, as it is not rotated.

$$^{B}(\boldsymbol{a})_{N} = \ddot{s}\,{}^{B}\boldsymbol{t}(s) + \frac{\dot{s}^2}{\rho}\,{}^{B}\mathbf{R}_{C}\,{}^{C}\boldsymbol{p} \tag{3.9}$$

3.6. step 3: steady motion of a point mass on a massless stick moving over a center line of a ribbon

Now let's consider a mass on a massless stick, that moves over a curve that can be considered the center line of a ribbon. Therefore, the accelerations will be expressed in the ribbon frame. The massless stick can make a roll movement (around the tangent) but pitch and yaw rotations are restricted. This can be imagined as a massless stick with a point mass at its end connected to a hinge (see figure 3.10). This means that there are three force equations and one moment equation, around the tangent vector $\boldsymbol{t}$, that are of interest. The normal force at the contact point with the ground, as well as the forces in the longitudinal and lateral direction and the roll angle can be calculated from those equations. The angle ϕ describes the angle between the TM plane and the point mass. The frame that sticks with the point mass and experiences the same rotation will be called the $\mathcal{F}$ frame. To indicate the lateral and longitudinal directions, the indications x and y are used.

The vector $\boldsymbol{r}$ describes the orientation of the massless stick. This vector points from the hinge on the ground towards the center of mass.

$$^{B}\boldsymbol{r} = {}^{B}\mathbf{R}_{F}\,{}^{F}\boldsymbol{r} = \begin{bmatrix} 1 & 0 & 0 \\ 0 & cos(\phi) & sin(\phi) \\ 0 & -sin(\phi) & cos(\phi) \end{bmatrix} \begin{bmatrix} 0 \\ 0 \\ h \end{bmatrix} \tag{3.10}$$

The gravitational force needs to be expressed in the $\mathcal{B}$ frame as well. The force equations can then be found.

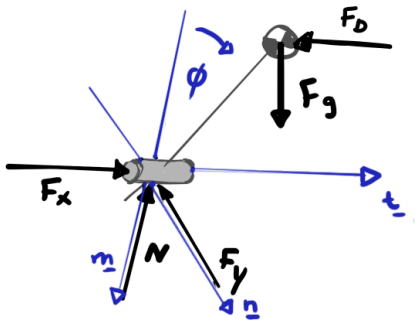

Figure 3.10: Free body diagram of the point mass

$$m\,{}^{B}\boldsymbol{a} = \begin{bmatrix} F_x - F_d \\ F_y \\ N \end{bmatrix} + \underbrace{{}^{B}\mathbf{R}_N \begin{bmatrix} 0 \\ 0 \\ -mg \end{bmatrix}}_{\boldsymbol{F_g}} \tag{3.11}$$

The moment equation of interest is the roll moment, around the tangent vector. Steady motion means that time lag or other time dependent effects are not considered. The steady-state roll is assumed to be reached instantly. Therefore, angular acceleration is not considered.

$$[\boldsymbol{r} \times \boldsymbol{F_g} - \boldsymbol{r} \times m\boldsymbol{a} + \boldsymbol{r} \times \boldsymbol{F} + r \times \boldsymbol{F_d}] \cdot \boldsymbol{t} = 0 \tag{3.12}$$

The drag force is located at the center of mass (CoM), because the center of pressure is assumed to be at the location of the CoM. Because F_d does not cause a moment around $\boldsymbol{t}$, and neither do the contact forces, this can be simplified to:

$$[\boldsymbol{r} \times \boldsymbol{F_g} - \boldsymbol{r} \times m\boldsymbol{a}] \cdot \boldsymbol{t} = 0 \tag{3.13}$$

3.7. final steps: steady motion of a simplified bicycle

In this section the point mass moving on a massless stick will be transformed into something more like a bicycle. Instead of a massless stick, a massless frame with two contact points (the wheel contact points) will be used. First, this structure will be regarded while moving over the center line of the ribbon. Then, this is extended towards movement throughout the ribbon plane.

3.7.1. moving over the center line of a ribbon

First the extension of the model will be applied to movement over the center line of the ribbon. The free body diagram can be seen in figure 3.11. The rigid body is simplified to such length that we can regard it as a point mass connected to a massless rigid frame with two contact points. The rear and front contact points are denoted by $_r$ and $_f$.

The force equations do not change much with respect to the previous situation (point mass on massless stick). The main difference is that the there are now two pairs of tire forces.

$$m\,{}^{B}\boldsymbol{a} = \begin{bmatrix} F_{xr} + F_{xf} - F_d \\ F_{yr} + F_{yf} \\ N_r + N_f \end{bmatrix} + \underbrace{{}^{B}\mathbf{R}_N \begin{bmatrix} 0 \\ 0 \\ -mg \end{bmatrix}}_{\boldsymbol{F_g}} \tag{3.14}$$

The vector r describes the position of the center of mass with respect to the origin of the ribbon frame. The vectors r_r and r_f describe the position of the contact points of the rear and front wheels, relative to the origin of the ribbon frame.

$${}^{B}\boldsymbol{r} = \begin{bmatrix} 1 & 0 & 0 \\ 0 & cos(\phi) & sin(\phi) \\ 0 & -sin(\phi) & cos(\phi) \end{bmatrix} \begin{bmatrix} 0 \\ 0 \\ h \end{bmatrix}, \; {}^{B}\boldsymbol{r_r} = \begin{bmatrix} -b \\ 0 \\ 0 \end{bmatrix}, \; {}^{B}\boldsymbol{r_f} = \begin{bmatrix} w-b \\ 0 \\ 0 \end{bmatrix} \tag{3.15}$$

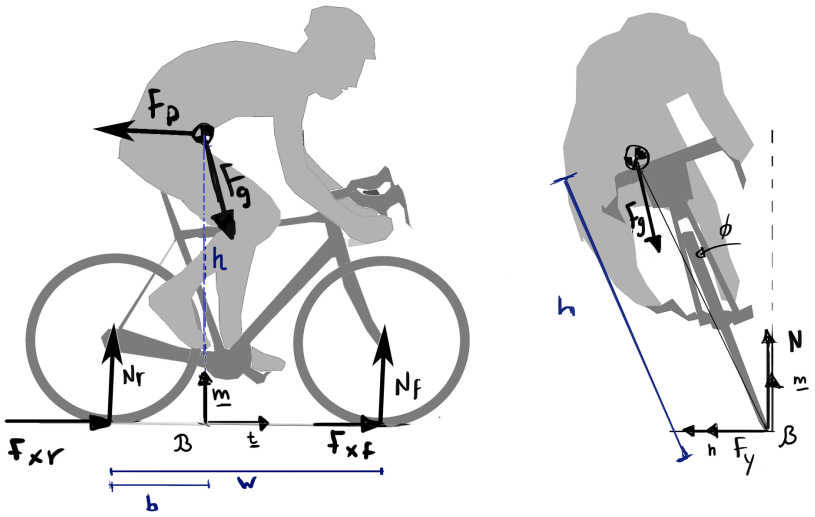

Figure 3.11: Free body diagram of a cyclist cycling over the ribbon plane, depicted in the local ribbon plane orientation.

The force vectors can be split in three vectors: a force at the rear wheel, one at the front wheel and the air drag force, that always works in the opposite direction of movement (negative sense of unit tangent vector).

$$ {}^{B}\boldsymbol{F_r} = \begin{bmatrix} F_{xr} \\ F_{yr} \\ N_r \end{bmatrix}, {}^{B}\boldsymbol{F_f} = \begin{bmatrix} F_{xf} \\ F_{yf} \\ N_f \end{bmatrix}, {}^{B}\boldsymbol{F_d} = \begin{bmatrix} -F_d \\ 0 \\ 0 \end{bmatrix} \tag{3.16} $$

The main difference between this situation and the previous one is that now moment equations around three axes need to be considered instead of one. Steady motion is considered still.

$$ \sum M = \boldsymbol{r} \times \boldsymbol{F_g} + \boldsymbol{r} \times -m\boldsymbol{a} + \boldsymbol{r_r} \times \boldsymbol{F_r} + \boldsymbol{r_f} \times \boldsymbol{F_f} + r \times \boldsymbol{F_d} = 0 \tag{3.17} $$

3.7.2. moving over the ribbon plane

Now we can extend this idea for a bicycle that can move over the whole ribbon plane, instead of the center line only. There is just one factor that changes with respect to the situation in the previous section: the orientation of the cyclist with respect to the center line, χ, has changed. The frame that is related to this new orientation is the $\mathcal{D}$riving frame. The only vector of which the expression changes due to this change in orientation is the gravitational force vector. This vector always points in the negative z direction of the inertial frame (see figure 3.12 on the next page). Other external forces such as the air drag force depend on the direction of movement. It always points in the opposite direction of movement, so that it is easy to express in the driving frame $\mathcal{D}$. In the end, this means that only the rotation matrix R changes with respect to the equations of a simplified bicycle moving over a curve. It now maps from the inertial frame to the driving frame, ${}^{D}R_N$.

The found steady motion equations depend on the orientation of the ribbon plane where the cyclist is cycling, the cycling velocity (this is reflected in the drag force) as well as the cyclists orientation with respect to the center line.

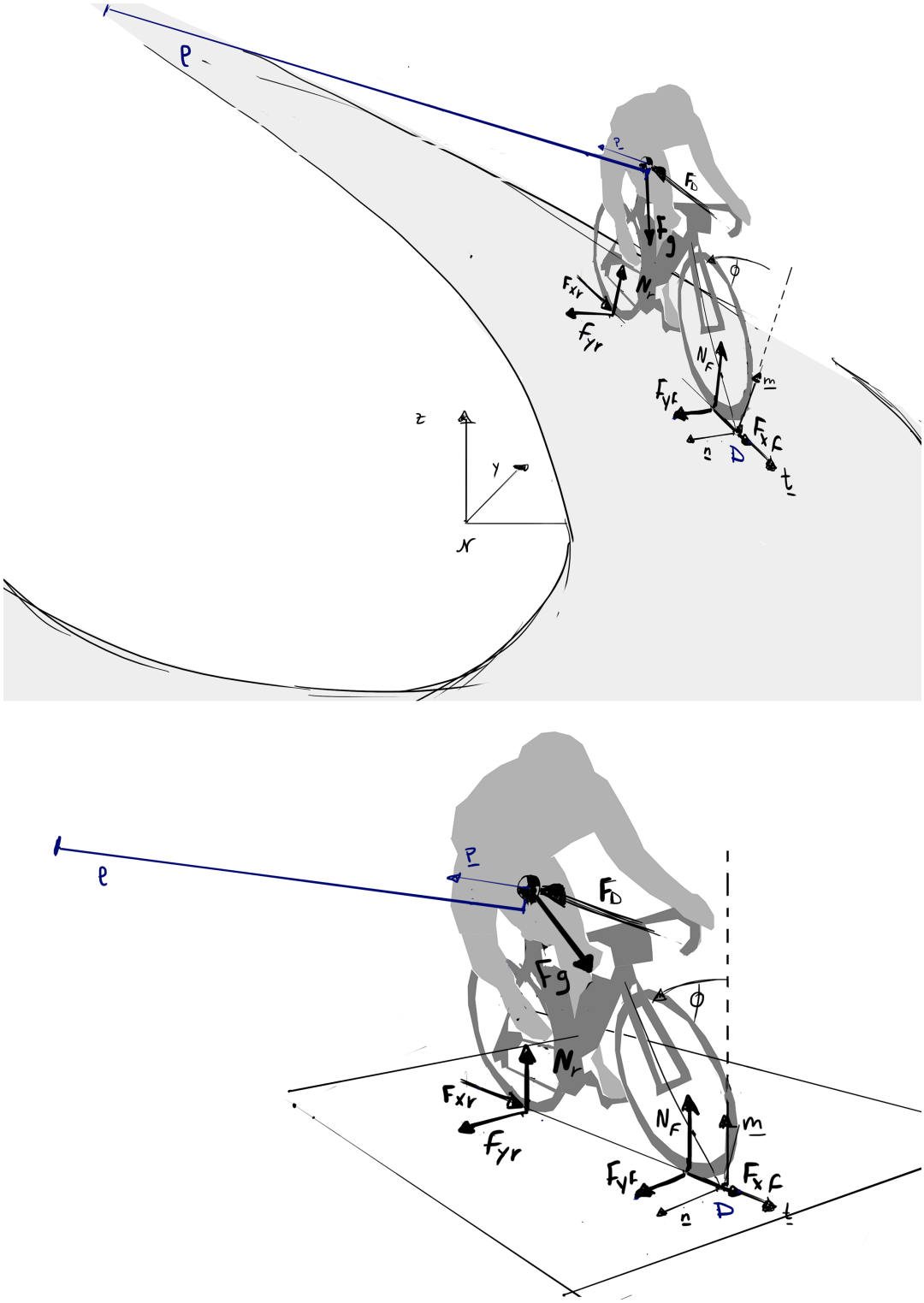

Figure 3.12: In this figure it is illustrated how a certain configuration of a cyclist moving over a track (upper image) can be seen in a simple way (bottom image). The idea is to look at the cyclist at a certain location s and n from a driving frame perspective. The cyclist is observed as if riding over a flat plane. The only vector that changes direction, is the gravitational force vector. The normal forces, lateral, and longitudinal forces always act in the directions of the base vectors of the coordinate frame $\mathcal{D}$, as does the aerodynamic drag force. To describe the direction of $\boldsymbol{F_g}$ in the $\mathcal{D}$ frame, ${}^{D}\mathbf{R}_{N}$ is used, which is a function of elevation Euler angle ψ, banking Euler angle γ, and χ.

3.8. finding the acceleration limits

There are multiple approaches towards finding the acceleration limits to create a g-g diagram. One option is to find the limits analytically, by setting tire forces equal to the tire force limits. This option works well for a simple problem with a few variables. However, a great deal of variables are necessary to describe acceleration limits for a 3D case. To deal with this, a sequence of optimisations is used to form the g-g diagram. The optimisation is run via the function *fmincon*, available in MATLAB. The goal is to maximise the adherence radius, and so the constrained nonlinear multivariable function describes the radius with variables a_x and a_y (see equation 3.18). The negative sign comes from the fact that *fmincon* searches for a minimum cost, while the goal is to maximize the adherence radius.

$$J = -(a_x^2 + a_y^2) \tag{3.18}$$

The function is constrained by several equations.

3.8.1. steady motion constraints

The steady motion equations form a part of the constraints. To complete the steady motion equations, a relation needs to be found such that there are only two independent variables. In this case, a_z is taken as a dependent variable. a_z is chosen because a_x and a_y translate more easily into the classic bicycle inputs (steer, lean, pedalling/braking). Next to this, a_x and a_y depend on the derivatives of the states. a_z does not depend on them. This can be seen when looking at the equations for acceleration. When calculating a_z expression 3.19 is found.

$$^D a_z = \dot{\beta}\sin(\chi)v + \dot{s}\sin(\beta)\cos(\chi)\frac{v}{\rho} \tag{3.19}$$

This makes it clear that a_z depends on β, the twist angle. When the rider moves (and keeps moving) in the osculating plane where β equals zero, the normal force is not affected. It is furthermore affected by $\dot{s}$, that in turn depends on the lateral road position n, next to the variables that are already in the expression for a_z. The dependence on n is clear when looking at a situation with a banked corner and a turn, like in figure 3.13. If the rider cycles on the outside of the turn, a larger turn is made with a bigger radius. Less acceleration in the principal normal direction is needed, so the normal force experienced by the cyclist is smaller. The opposite is true when cycling at the inside of the turn.

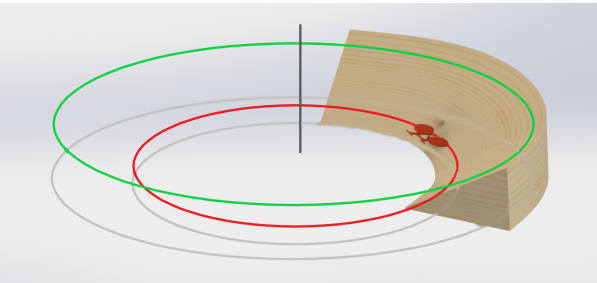

Figure 3.13: The difference between the sizes of the osculating circles causes differences in lateral acceleration. This results in different normal forces due to the banking with respect to the osculating plane.

3.8.2. tire constraints

A very important constraint comes from the tire model. The tire forces that are a result of the found acceleration limit should remain within the friction ellipse. The tire constraint is therefore the same as the description of the friction ellipse given in equation 3.1.

3.8.3. maximized braking constraint

As for braking, it is efficient to maximize the adherence radius. Maximizing the adherence radius to the fullest can be done by making optimal use of the front and rear brake. This is the 'optimal braking' strategy as mentioned earlier in this chapter. Biral and Lot show that front only braking, a strategy which is often used by elite cyclists, does not maximize the adherence radius [29]. For this project, optimal braking will be implemented. As this project is about finding the theoretically best possible performance, it will be assumed that the cyclist can optimally control braking. In reality, this is not so easy.

To find the maximized adherence radius, equal engagement is assumed, to make sure that maximum braking capacity at both the front and rear wheel is accomplished. The equal engagement constraint that implies optimal braking is described in equation 3.20. The constraint is only active when $F_{xr} < 0$, since this condition implies that the cyclist is braking.

$$\frac{F_{xr}}{N_r} - \frac{F_{xf}}{N_f} = 0 \tag{3.20}$$

3.8.4. variable boundaries

While the cyclist applies force on the pedals, the resulting forward force is applied at the rear tire only. This means that there cannot be a propelling force on the front tire, only a braking force. This condition is added through a boundary condition of the front tire longitudinal force. The upper boundary for F_{xf} is equal to 0.

Another boundary condition is applied to the normal forces on the front and rear wheel. If the normal forces cannot become zero or negative, it is ensured that the cyclist does not lose ground contact. In practise, it is possible that a cyclist loses ground contact for a short duration, for instance while driving over a bump. But a g-g diagram relies on ground contact, it is build up out of the friction ellipse, so it is assumed that the cyclist has ground contact. Furthermore, the boundary condition implies two behavioural constraints: a stoppie limit (rear wheel loses ground contact) and a wheelie limit (front wheel loses ground contact). The wheelie limit will probably never be reached, since in this model it is only met when a lot more power is applied than a cyclist can deliver, even during peak performance. The stoppie limit is very important on downward slopes. Due to the slope angle, it is easier for the cyclist to lose ground contact with the rear wheel and tumble. With the stoppie limit it is ensured (theoretically) that the cyclist will not experience such a fall.

3.8.5. power constraint

A power constraint needs to be added to make sure that the pedalling power exerted through the rear wheel is limited to the maximum power that can be delivered. In this model, this will be the critical power since it can be sustained for longer time periods.

$$F_{xr}\, v \leq P_{max} \tag{3.21}$$

3.8.6. NLP formulation

To sum it up, the goal is to maximize the adherence radius, while it is constrained by equation 3.14, 3.17, and equation 3.1 - C.1. The variables used in solving the NLP are $a_x, a_y, F_{xr}, F_{xf}, F_{yf}, N_r, N_f$ and ϕ. The parameters which change the NLP formulation are $\alpha, v, \psi, \gamma, \beta, \dot{\beta}, \rho, n$, and χ. A solving approach for the NLP can be found in appendix C.

3.9. conclusion

A model was developed to generate g-g diagrams as a function of $\alpha, v, \psi, \gamma, \beta, \dot{\beta}, \rho, n$, and χ. The road is described via a ribbon geometry. The tire model used is a simple friction ellipse. The bicycle and rider are modelled as a single point mass on a massless construction with two road contact points, assuming steady motion.

Assumptions of the road geometry-

- there is no lateral curvature
- the road is smooth, there are no small bumps

Assumptions of the tire model-
The friction ellipse tire model does not take into account any of the specific tire characteristics. It is based only on the friction coefficients, and the idea that the general shape of the maximum tire forces could be an ellipse. This idea of a circle is based on tire characteristics like camber stiffness, but they do not directly describe the tire behaviour.

Assumptions of the bicycle plus rider model-

- steady motion
- the side slip angle is small
- the bicycle and cyclist are one rigid body, therefore the movement of the wheels, the movement of the front fork with respect to the frame, the movement of the rider with respect to the bicycle and any other movement within the bicycle and the rider are neglected.
- the center of pressure is located at the center of mass.
- a constant power limit instead of a power model that accounts for exhaustion.

Assumptions of the g-g diagram generating function-

- environmental variables do not vary over the track (like air density, the friction coefficient)
- driver behaviour does not change over the track, e.g. the cyclist does not lean to backwards while braking, and the $C_d A$ does not change either.
- the wind speed is 0 m/s at all times.

4

How bicycle, rider, environment, and track parameters affect g-g diagrams

The shape and placement of the g-g diagram determine the solution of the minimum time optimisation. Therefore, it is interesting to analyse which parameters have greater and smaller influence on the g-g diagram, and what kind of influence they have. Those parameters were placed into three categories: bicycle and rider parameters, environment parameters, and track parameters.

4.1. rider and bicycle parameters

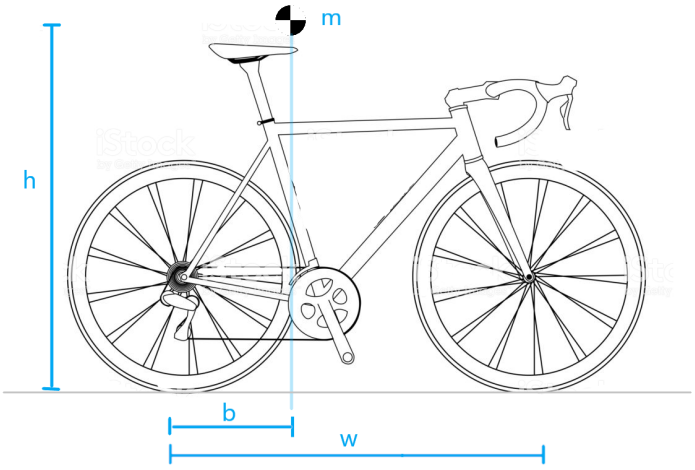

Figure 4.1: Bicycle measurements h, w and b

Rider and bicycle parameters that influence the g-g diagram are illustrated in figure 4.1. The parameters are either constant or assumed to be constant over the length of the track. Truly constant parameters in this model are mass m and wheelbase w. Small amounts of mass might be lost over the course of the track due to for example sweating and urination, but this is negligible. The wheelbase is constant, unless a bike change is made. Some parameters are assumed to be constant, but in reality aren't. A great example is the height of the center of mass h in the bicycle frame $\mathcal{F}$, as cyclists tend to lower their center of mass during descents. Of course, it also varies in a smaller amount as a result of regular cycling movement. The same can be said about the longitudinal distance from the rear wheel contact point to the center of mass b, as expressed in the same frame $\mathcal{F}$. Most cyclists lean to the back of their bicycle while braking, changing b. During normal cycling movement it also varies a little bit.

The effect of the parameters on the shape of the g-g diagram was investigated by changing one parameter at a time, while keeping the others constant. It is expected that the parameters will affect the same areas of the g-g diagram, regardless of the track geometry. Therefore, a simple 2D flat track was chosen as a baseline for this sensitivity study.

4.1.1. mass

The masses chosen reflect the range of masses where elite cyclists plus their bicycles lie within. A bicycle weighs at least 6.8 kg according to the general UCI regulations for all categories of cycling competitions. In figure 4.2a resulting g-g diagrams can be found where only the mass differs. Mass only effects the ability to accelerate, and to decelerate longitudinally. A lighter person is better at both accelerating and decelerating. At first thought, this might seem strange. A lighter person would have relatively more trouble with aerodynamic drag, this would make it indeed easier to brake but harder to accelerate. But when looking at equation 4.1, the answer is found.

$$a_x = \frac{P_{max}}{mv} - \frac{F_d}{m} - g\sin(\psi) \tag{4.1}$$

The key lies in the power definition. For this model, a power limit was used. It is kept constant while the mass is varied, so that the amount of Watt per kilogram changes over the g-g diagrams. A lighter rider will have relatively more Watts per kilogram available to accelerate. This effect is larger than that of the aerodynamic drag, and therefore the lighter rider will be able to accelerate more. The effect of mass changes on g-g diagrams where only front braking is allowed were investigated as well. There are no differences in how mass is affecting g-g diagrams that take 'optimal braking' and front braking only into account.

4.1.2. wheelbase

Wheelbases of bicycles do not differ much. As a baseline, the wheelbase of the Ultimate CF SL Disc 8.0 Di2 Canyon bike was taken. The resulting g-g diagrams are seen in figure 4.2b. The diagrams are not very different, they only have a slight difference at the bottom. This is the stoppie limit. With a shorter wheelbase, the center of mass is closer to the front wheel contact point. Therefore, the moment arm of the gravitational force keeping the cyclist on the ground is shortened, and it is easier to lose rear wheel ground contact. The effect of wheelbase changes on g-g diagrams where only front braking is allowed were investigated as well. There are no differences in how the wheelbase is affecting g-g diagrams that take 'optimal braking' and front braking only into account.

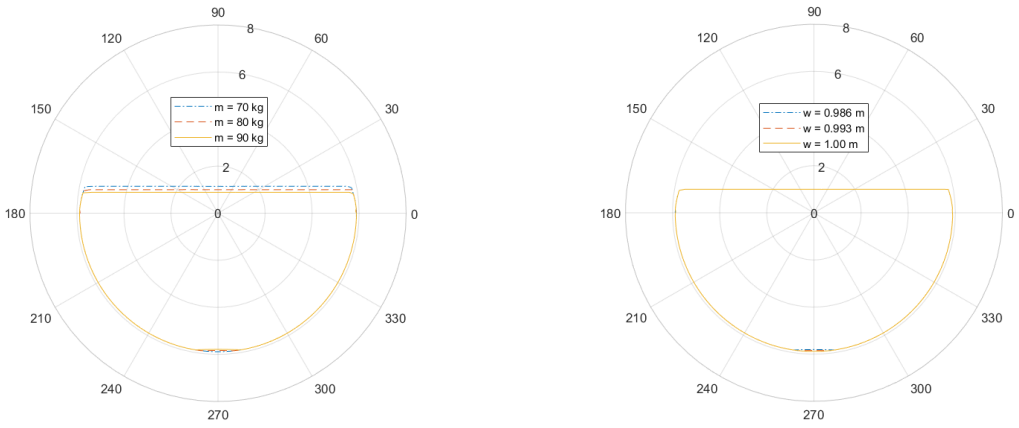

(a) g-g diagrams with varying mass parameter.

(b) g-g diagrams with varying wheelbase parameter

Figure 4.2: Influence of the mass and the wheelbase on the acceleration limits.

4.1.3. height of the CoM in the bicycle frame $\mathcal{F}$

Based on the observations by Biral & Lot [29], who performed a comparable sensitivity analysis for motorcycle g-g diagrams, the effect of the height of the center of mass is expected to be large. While in figure 4.3a the stoppie limit is largely affected by a change in h, the rest of the diagram is unaffected. The effect on the stoppie limit can be explained by the effect of the height of the CoM on the load transfer. With a higher CoM, there is more load transfer and the cyclist will have transferred its load to the front wheel faster, with rear wheel ground contact loss as a result. However, some effects on combined lateral and longitudinal acceleration are expected as well, due to the increased load transfer. An explanation for this is that the cyclist in this model follows 'optimal braking', and will be able to achieve maximum braking at the front and rear wheel anyway. In practise, elite cyclists mostly use their front brakes, and do not achieve the theoretically optimal braking. Therefore, it is interesting to look at the effect of a varying height of the CoM when only front braking is used as well, to fully understand its effect. This is investigated in figure 4.3b

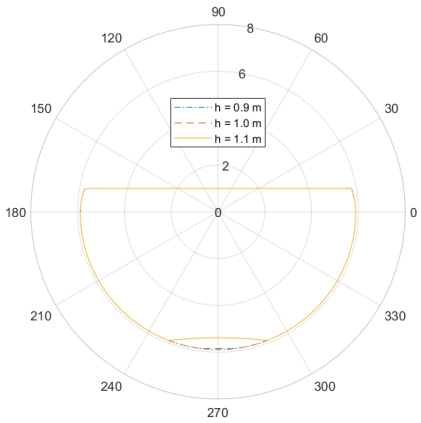

(a) g-g diagrams with varying h, optimal braking

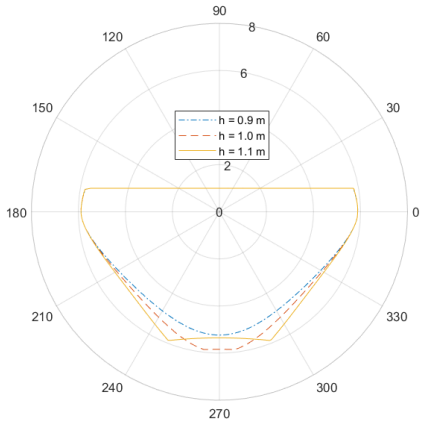

(b) g-g diagrams with varying h, front brake only

Figure 4.3: Influence of the height of the CoM position.

4.1.4. longitudinal position of the CoM in the bicycle frame $\mathcal{F}$

The effect of the longitudinal position of the CoM was studied by Biral and Lot as well. As with the height of the CoM, large effects on the diagram are expected based on that study. The longer b is, the closer the CoM is positioned towards the front wheel contact point. When the CoM is positioned more towards the front, the load transfer is already before braking more towards the front as well. This effect is visible in the stoppie limit line at the bottom of the left diagram, figure 4.4a. A larger effect is seen when only front braking is applied (see figure 4.4b). When looking at pure longitudinal deceleration, their is a minimum length for b that still results in greater deceleration limits. This happens probably due to the fact that only a small proportion of the load is sustained at the front wheel, restricting the maximum brake force that can be generated. As the stoppie limit will move up and down due to elevation differences, an optimal b could be found when riding a specific descent.

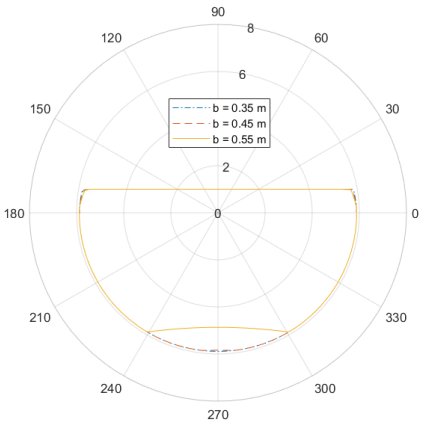

(a) g-g diagrams with varying b, optimal braking

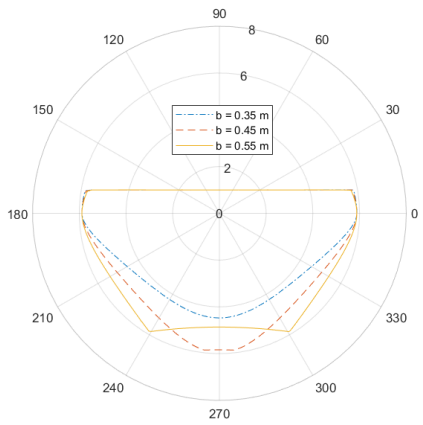

(b) g-g diagrams with varying b, front brake only

Figure 4.4: Influence of the longitudinal CoM position.

4.1.5. drag area

The drag area $C_d A$ is build up out of the drag coefficient of a cyclist times the frontal area. Both can be influenced by rider behaviour. The drag coefficient is affected by the shape of the cyclist. Cyclists have shown very different strategies to counter air drag, ranging from hanging from the steering wheel (as displayed by Froome) to laying flat on the seat (also called the superman) [10]. Next to position changes prioritizing the minimisation of air drag, a cyclist also changes its attitude while braking (shifting the CoM to the back) and in sharp turns (leaning sideways). For this model, the drag area is assumed constant over the length of the track. Varying the drag coefficient affects the drag force, which affects the maximum acceleration and deceleration. With a greater $C_d A$, accelerating gets harder and deceleration easier.

4.1.6. conclusion

The mass of the rider and the wheelbase of the bicycle have only a minor influence on the g-g diagram. The height and longitudinal position of the center of mass play a larger role. Since this study seeks the theoretically optimal solution, and because humans are optimizers, it can be said that the cyclist always chooses the most optimal values that lie within the possibilities. This would mean that the height of the CoM is as low as possible, and the longitudinal position is as far to the back as possible. In combination with the optimal braking strategy, this configuration is ideal.

4.2. environment parameters

There are only two parameters used in the g-g diagram model that can be classified as environment parameters: friction coefficients μ_x/μ_y, and air density ρ_a. The friction coefficient effects the size of the friction circle, which forms the basis of the g-g diagram. The acceleration limits can only be constrained further within the friction circle. The air density affects the aerodynamic drag force, so it affects the acceleration limit in the same way as the drag area. It changes slightly over height, but so little that it is assumed constant.

4.3. track parameters

With track parameters, parameters that can change over the length of the track are meant. For this model there are 8 track parameters: $v, \psi, \gamma, \beta, \dot{\beta}, \kappa, n$ and χ. For a track that is elevated and/or banked, track parameters hugely influence the g-g diagram. Where bicycle and rider parameters influence the g-g diagram independently, track parameters do not. Therefore, a systematic analysis was necessary to fully research all possible combinations of effects. Before that, a few examples of track parameter effects are given to create some familiarity with the idea, and to explain the complexity.

4.3.1. general examples

To give some insight in the behavior of the g-g diagram, some general examples are given in this section. As a reference configuration a flat straight track is chosen (the direction of gravity is the normal direction into the plane), see figure 4.5. Variables are changed one by one with respect to this reference configuration.

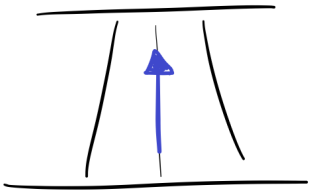

Figure 4.5: The reference configuration: a flat, straight road.

banking-
When the banking angle is changed, the main effect is that the diagram shifts horizontally (see figure 4.6b). This happens due to the lateral force that is induced by the banking. A lateral force is now working on the cyclist, so that in one direction lateral acceleration is supplemented, while it is reduced in the other direction. Another smaller effect (small for realistic banking angles) is that the normal force decreases decreases due to the angle of the road with respect to the direction of gravity. This causes shrinkage of the g-g diagram.

curvature-
When curvature is changed for a flat road, nothing happens to the g-g diagram (see figure 4.7b). The acceleration limits are still the same, since the external forces have not changed. The limits might indicate that a certain curvature cannot be ridden at a certain speed, but that will show in the minimum-time optimisation from the state equations. The curvature can have an influence on the diagram when combined with 3D track aspects. This will be further discussed in section 4.3.2.

elevation-
As visible in figure 4.8b, elevation influences mainly the vertical position of the g-g diagram. Here a negative elevation is

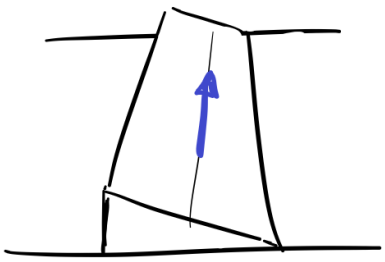

(a) A straight road with banking

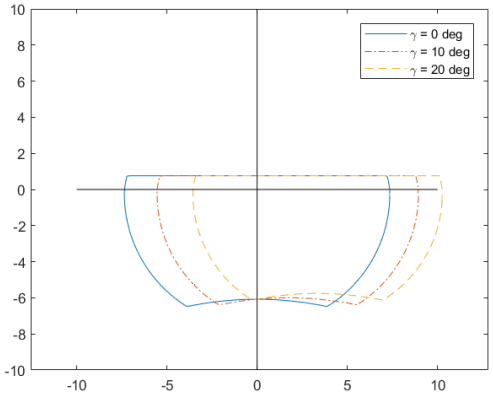

(b) Positive banking is applied, which means that the right side of the track is the downside. The diagram mainly shifts to the right, but also shrinks a bit.

Figure 4.6: Effect of banking

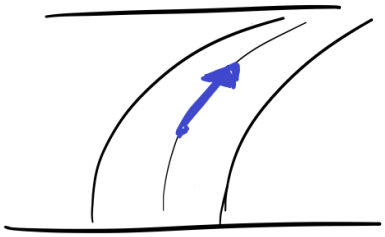

(a) A flat curved road

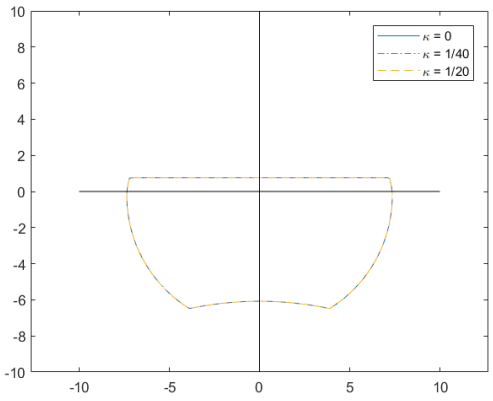

(b) The g-g diagram when different amounts of curvature are applied to a flat track.

Figure 4.7: Effect of curvature

chosen, which represents a downward slope. The cyclist benefits from the gravity working partly along the longitudinal direction, providing extra propulsion. On the other hand, because of that extra propulsion braking is harder as well. The diagram will shrink a little bit as well, due to the normal force on the ribbon plane being smaller as a result of the relative direction of gravity.

combined effects-
When the curvature was examined, no effect was found. However, kappa can have an effect when the track is not flat. An example: when the road has a curvature κ, both the direction of the curvature (displayed by β) and the banking of the road (γ) influence how the g-g diagram is affected. A given value for κ can have zero influence, a large influence and anything in between. This is well visible in figure 4.9.

4.3.2. systematic analysis method

There are some effects of variables on the shape and position of the g-g diagram that are less straight forward. To examine those effects, a more systematic approach was used. Six multiple regressions were used to predict a_x and a_y at three different locations on the g-g diagram. The locations on the g-g diagram are chosen at the $F_x = 0$, the $F_y = 0$ and the $F_y = -F_x$ positions, where a_y has the largest value (first and latter case) or a_x the smallest (second case), see figure 4.10. This is done to find out the correlations between the input variables variables and the position and shape of the g-g

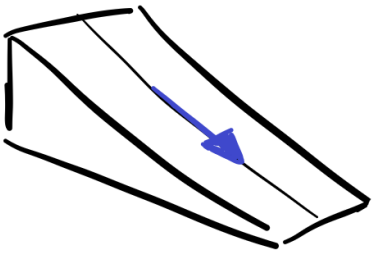

(a) An elevated road

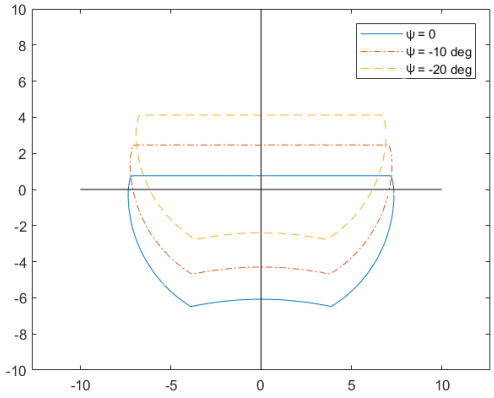

(b) Elevation mainly affects the vertical position of the g-g diagram.

Figure 4.8: Effect of elevation

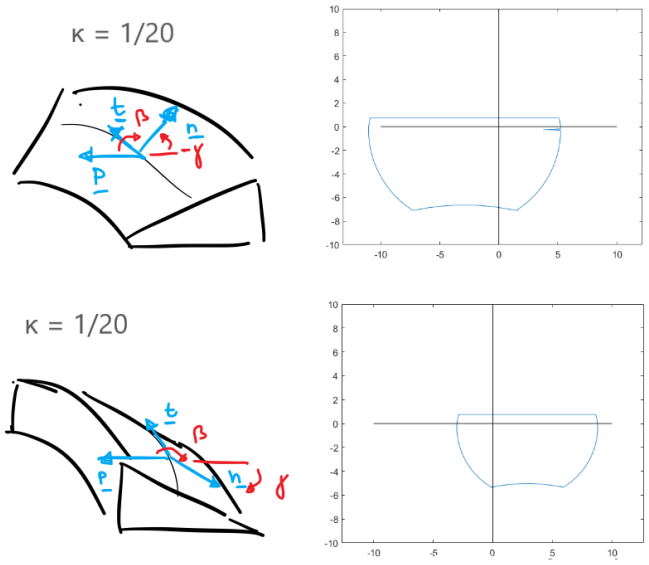

Figure 4.9: Note that the axis scaling is the same in both graphs. The value of kappa is the same, but the effect of enlarging kappa in both situations results in the opposite expansion effect. At the left situation, the normal forces will increase with kappa, at the right situation they will decrease when kappa increases.

diagram. Three locations are chosen since it is impossible to run a multiple regression analysis for every location on the diagram. The $F_x = 0$ position is located at the largest lateral width of the diagram, and the $F_y = 0$ position monitors the deceleration limit. Together, they can tell something about position shifts, and lateral and horizontal shape changes. The remaining position monitors the shape of the g-g diagram. For this, 320 random samples have been taken by selecting random variable values from specified ranges, and calculating the corresponding a_x and a_y. The ranges are found in appendix H. Statistically significant variable correlations are not present (no multicollinearity). To make sure that the relations between the predictors and the dependent variable (a_x and a_y) are linear, some variables (β, κ and χ) are transformed to meet the requirement for a linear multiple regression. They have been transformed to $|\sin(\beta)|, |\sin(\kappa)|$ and $\cos(\chi)$. Graphs of the correlations between the dependent variable and the independent variables are found in appendix I.

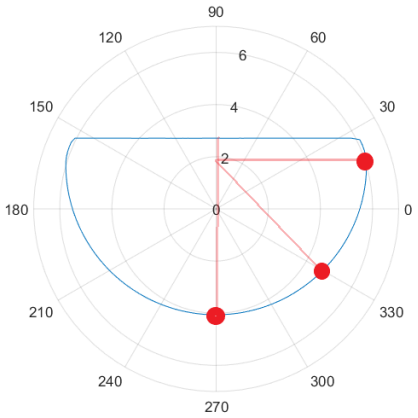

Figure 4.10: An indication of possible $F_x = 0, F_y = 0$ and $F_y = -F_x$ positions. This g-g diagram is based on a downwards slope.

4.3.3. results

$F_x = 0, a_x$

These variables statistically significantly predicted a_x, $F(1,97) = 211, p < .0005, R2 = 0.845$. Three variables ($v, \psi$ and $\cos(\chi)$) added statistically significantly to the prediction, p < .05. The respective standardized coefficients of v, ψ and $\cos(\chi)$ are -0.4478, -0.7733 and -0.1140.

$Fx = 0, a_y$

These variables statistically significantly predicted a_y, $F(1,97) = 3.66, p < .0005, R2 = 0.0861$. Four variables ($V, |\sin(\beta)|, |\sin(\kappa)|$ and $\cos(\chi)$) added statistically significantly to the prediction, p < .05. The respective standardized coefficients of $V, |\sin(\beta)|, |\sin(\kappa)|$ and $\cos(\chi)$ are 0.1502, -0.1454, 0.1128 and 0.1640.

$F_y = 0, a_x$

These variables statistically significantly predicted a_x, $F(1,97) = 9.02, p < .0005, R2 = 0.188$. Three variables ($v, |\sin(\kappa)|$ and $\cos(\chi)$) added statistically significantly to the prediction, p < .05. The respective standardized coefficients of $v, |\sin(\kappa)|$ and $\cos(\chi)$ are -0.3617, -0.1294, and 0.1910.

$Fy = 0, a_y$

These variables statistically significantly predicted a_y, $F(1,97) = 27.1, p < .0005, R2 = 0.41$. Only ψ and γ add statistically significantly to the prediction, p < .05. The standardized coefficient of ψ and γ are -0.0911 and 0.6153

$-F_x = F_y, a_x$

These variables statistically significantly predicted a_x, $F(1,97) = 7.56, p < .0005, R2 = 0.163$. Only $v, |\sin(\kappa)|$ and $\cos(\chi)$ added statistically significantly to the prediction, p < .05. The respective standardized coefficients of $v, |\sin(\kappa)|$ and $\cos(\chi)$ are -0.2976, -0.1635 and -0.1785.

$-F_x = F_y, a_y$

These variables statistically significantly predicted a_y, $F(1.97) = 4.13, p < .0005, R^2 = 0.096$. Only $v, \gamma, |\sin(\kappa)|$ and $\cos(\chi)$ added statistically significantly to the prediction, p < .05. The respective standardized coefficients of $v, \gamma, |\sin(\kappa)|$ and $\cos(\chi)$ are 0.2038, 0.1143, 0.1182, and 0.1206

4.3.4. analysis of the results

All regression analyses show that the variables statistically significantly predict a_x and a_y. However, the coefficients of determination (R^2) indicate varying quality of the predictions. A very low R^2 such as with the a_x prediction at $F_x = 0$ indicates that only 8,6% of the variance is explained through the prediction. The value of a_x at $F_x = 0$ and the value of a_y at $F_y = 0$ can be predicted with most of the variance accounted for by the model (84,5% and 41,0% respectively). This shows that the variables that significantly contribute to this prediction indeed deliver a large contribution to the values of the dependent variable. It is doubtful whether the variables that contribute significantly to the other predictions are important for the prediction of the dependent variable at all. Therefore, mainly the two predictions that provide good fits will be discussed.

Since only two multiple regressions resulted in good fitting models, they will be analyzed in more detail. Variable v has a negative correlation with the longitudinal acceleration at the line where the forces in the x direction are zero. This can be

Table 4.1: The results of the multiple regression analyses

	a_x		a_y	
	var	stand coef	var	stand coef
$F_x = 0$	v	-0.4478	v	0.1520
	ψ	-0.7733	$\|\sin(\beta)\|$	-0.1454
	$\cos(\chi)$	-0.1140	$\|\sin(\kappa)\|$	0.1128
			$\cos(\chi)$	0.1640
$F_y = 0$	v	-0.3617	ψ	-0.0911
	$\|\sin(\kappa)\|$	-0.1294	γ	0.6153
	$\cos(\chi)$	0.1910		
$F_x = F_y$	v	-0.2976	v	0.2038
	$\|\sin(\kappa)\|$	-0.1635	γ	0.1143
	$\cos(\chi)$	-0.1785	$\|\sin(\kappa)\|$	0.1182
			$\cos(\chi)$	0.1206

explained by the fact that air drag increases when velocity increases. Variable ψ also has a negative correlation with the longitudinal acceleration. When the forward elevation is negative, the slope is downward. So a downward slope that is getting steeper will cause the longitudinal acceleration limit to increase at the $F_x = 0$ line. The third correlation is between $\cos(\chi)$ and the longitudinal acceleration. When the value of the cosine decreases, the longitudinal acceleration increases. This happens for extreme values of χ. The second prediction that accounts for most of the variance is that of the lateral acceleration at the $F_y = 0 line$. There, the predictor with the highest coefficient is the banking, γ. With increased banking, lateral acceleration increases to the right. Positive values of banking describe a road where the left side is higher than the right side. Due to gravity a force is always pulling the cyclist to the right, shifting the g-g diagram. The other predictor is the forward elevation. A steeper downward slope causes higher lateral acceleration at the bottom of the g-g diagram. This could be the effect of the stoppie limit. The steeper the downward slope, the earlier the stoppie limit is reached as it becomes easier to topple over the steer.

4.3.5. discussion

Variables that did not significantly contribute to any predictions, are n and $\dot{\beta}$. The shared factor of those variables is that they only influence the g-g diagram when χ does not equal zero. χ is a special case in any way. When looking at the equations of steady motion, χ does not influence the g-g diagram when it has a value around zero. It is debatable and it differs per track if χ can be assumed to be zero. Generally, χ is expected to be around zero for relatively narrow tracks, where the turns are not too tight. Neglecting χ means automatically that n and $\dot{\beta}$ do not influence the g-g diagram anymore. This saves a lot of computation time. Therefore, it should be discussed whether χ will play a large role before a minimum-time optimisation is made for a specific case.

4.3.6. conclusion multiple regression

Four of the multiple regression outcomes show a lot of unaccounted variance. Those models are not a good fit to the data. The two models that do account for most of the variance suggest that ψ is the main contributor to the vertical position of the $F_x = 0$ line, and that γ is the main contributor to the horizontal position of the $F_y = 0$ line. From the equations it can be predicted that both these variables mainly shift the g-g diagram. Variables n and $\dot{\beta}$ were never significant contributors to the predictions.

4.4. conclusion

The g-g diagram is influenced by many parameters. A systematic study was held to identify the effects of the rider and bicycle parameters on the g-g diagram. The height and longitudinal position of the CoM were the most influential parameters. As for the environment parameters, the friction coefficient influences the size of the g-g diagram whereas the air density does not play a large role (mainly because it does not differ much). From track parameters, some overall effects can be seen. ψ influences the vertical position of the diagram, and γ influences the horizontal position. n and $\dot{\beta}$ do not play a significant role. χ can hugely influence the diagram, but from the equations it can be seen that this is only the case when it has extreme values. In practise (with normal road cycling) it might be defensible to assume it to be around zero.

5

Case: The L218 near Vossenack, Germany

To demonstrate the capabilities and shortcomings of the model, a minimum-time optimisation was solved for a mountain road in Germany. The outcome is discussed and compared to measurements of the descent of elite cyclists on the same track.

5.1. case description

The L218 near Vossenack, Germany, was the subject of a study about braking behaviour of elite racing cyclists [51]. For this study, track data was gathered that can be used to model this track. The road segment has a length of 1.85 km, and the average descent gradient (ψ) is 5 percent. In the experiment the riders were assigned to descent as fast as possible, while staying safe. They were informed to use only the right half of the road, to ensure road safety. Therefore, only the right half of the track will be modeled to use in optimisation. The track was split up into eight segments with different cycling behaviour (see figure 5.1). The data of this track is used to solve a minimum-time optimisation. The results of the optimisation can be compared to the measurements conducted on-site.

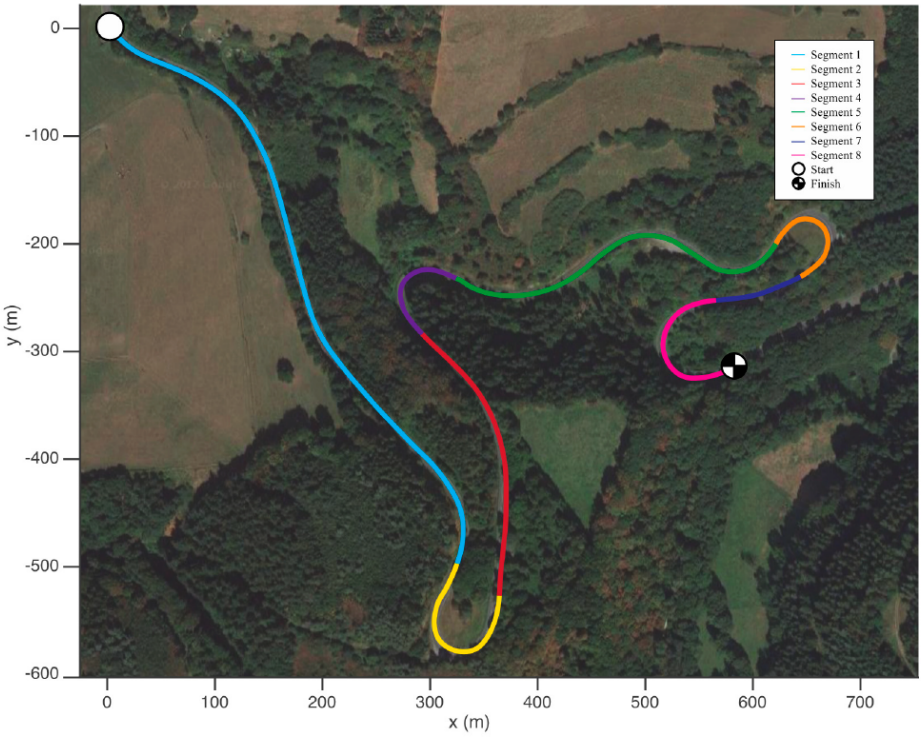

Figure 5.1: The part of the L218 near Vossenack, Germany, that was used for measurements. Figure from [51].

5.2. goal and research question

The goal of this case study is to compare the descent strategies of elite cyclist and the outcome of the minimum-time optimisation. An analysis of the measurements by Chris van Trigt pointed out that the fastest rider won time with respect its competitors by producing more power, and lost time while cornering [67]. Therefore, a special interest is taken towards tight corners. In straight segments, performance differences are due to differences in power usage, air drag and weight. In tight turns, it comes down to braking strategies. The segment where the riders experience the tightest turn is at segment 6. Therefore, next to an optimisation of the entire descent, segment 6 is optimised separately. There, the initial positioning and velocity of the measured cyclists are used, in order to compare the segment performance in the best way. The main research question for this case study is:
How does the optimal descent strategy differ from descent strategies practised by elite cyclists?
A hypothesis for the main question is that the braking strategy in sharp corners is the main difference.
Therefore, an important important subquestion is:
How does the optimal cornering strategy differ from strategies practised by elite cyclists?
A hypothesis is that using the optimal braking strategy allows the cyclists to brake harder, and accelerate more in general during the turn. The braking is expected to end at the same moment, so that the location of the minimum velocity is equal.

To be able to compare descent strategies, it should be known what is defined as a good performance. There are three scores that can be given to the performances. The most important metric is, of course, time. Furthermore, the performance can be measured by determining the percentage of the distance spent on decelerating, accelerating ($a_x > 0.1 m/s^2$ and $a_x < -0.1 m/s^2$) and the mean velocity / total time. Theoretically, the fastest descent time is obtained by accelerating very fast to the maximum velocity and minimize decelerations or perform these also as fast as possible. Those metrics that describe deceleration/acceleration percentages are especially interesting to compare performance for segment 6. In this segment, initial velocities at the start of the segment differ between riders. Those different initial velocities cause the segment times to differ, regardless of cornering performance quality. For segment 6 a fourth metric can be determined, which is the exit speed of the turn. This metric is often used to compare cornering performance of Formula One race cars.

5.3. method

In this section, the detailed inputs and settings for the minimum-time optimisations are discussed. The description of the OCP as presented in chapter 2 was used to run the optimisations, complimented by the details provided in this section. Some parts of the method differ between the optimisation of the full track and the separate optimisation of segment 6. If there is a difference, this is indicated.

5.3.1. track conditions & initial conditions

full track-
For the full descent, the following initial conditions were set:

v = 3 m/s, n = 0 m (center of the right lane), χ = 0.

The initial velocity differs from the initial velocity that was used for the measurements. There, cyclists had a standing start (v = 0 m/s). This was not used for the optimisation, since from experience it was found that the solver gets stuck in a restoration phase when the speed is below $3 m/s$. To make sure that a solution was reached for this large a problem, the track width was set to a constant value of 6.6 meters (average track width in the corners). The full track length is optimised at once; this means that for every optimisation iteration, new variable values are found for every node along the track.

segment 6-
For segment 6, the states of one of the riders at the start of the segment ($s = 1480 m$) were taken as the initial conditions:

v = 16.7 m/s, n = -3.3 m (left lane boundary), χ = 0.

The initial lateral positions of all the riders were not within the road boundaries at this location. The riders used the left side of the road (even though this was not allowed). The initial lateral position for the optimisation was however placed within the road boundaries, at the left track boundary to approximate the initial position of the elite cyclists at best as possible. As initial velocity, the lowest initial velocity of the measured descents was chosen. This was done to see if the overall time spent would be even lower than for cyclists who had a higher initial velocity.

Since the riders determine their controls (accelerations) based on where they come from and where they are going, it is important to not only model segment 6 specifically, but also take into account its surroundings. In this case segment 6 consists of a distance of 160 meters, but 30 meters extra are modelled at the end. At the start of the segment, the initial conditions are set to meet the riding behaviour of the elite cyclists. The end conditions are not fixed, to give the model

freedom to determine the optimal strategy. For segment 6, the measured track width was used as a boundary condition for n as a function of s.

5.3.2. power limit

An amount of 500 Watt is set as the power limit for both optimisations, since from the measurements it was seen that a maximum of 500 W could be sustained by the elite cyclists during the descent. This power can be sustained by the theoretical model until infinity, while real cyclists cannot sustain this amount of power for longer time spans. Further bicycle and rider details can be found in appendix E.

5.3.3. solver settings

The solver settings are reported to ensure replicability of the study. Discretisation is done via Legendre-Gauss-Radau (LGR) polynomials, which can provide accurate and smooth results. Smooth results are expected when looking at the measurement data and equations of motion. Furthermore the benefit of LGR polynomials is that the weights and nodal points (mesh points) can be updated by a mesh refinement function by the software such that the approximation is more accurate in areas where state values change rapidly. With other methods the nodal points are often fixed beforehand, and less accurate approximations can be created. The mesh refinement method was not used in this case however. For the full descent, 200 intervals with each 5 nodal points on fixed distances were used. This yielded a total number of 5000 variables to solve for. For segment 6, 30 intervals with 2 nodal points were used, yielding 300 variables. For the jacobian calculation, finite differencing is used. The software Adigator can approximate the jacobians better, but sadly in this specific case a bug was encountered [1].

5.3.4. run strategy

A mountain road is analyzed. As this is a long road, many variables (6000, three variables and their derivatives on 1000 nodes) need to be optimized. The g-g diagram optimisation model is not directly implemented inside the minimum-time optimisation. This would cause very long run-times. Instead, the previously discussed option of a prefabricated database was used. The adherence radii that result from a set of input conditions were stored in six dimensional database. The g-g diagrams were the function of 5 variables: cycling velocity v, elevation angle ψ, banking angle γ, twist angle β, and the center line curvature κ. Several more variables can influence the g-g diagram. However, the relative cyclist orientation χ was assumed to approximate zero. As the lateral position and twist rate only influence the g-g diagram when χ is not zero, they were left out as well. Since the adherence radius also corresponds to a certain adherence orientation, the corresponding database has six dimensions. The database was interpolated cubically with the multidimensional interpolation function from MATLAB, *interpn*. The variable ranges that were taken into account are reported in appendix H.

Due to the interpolation of a large database, the optimisation is slow. To help the optimisation with convergence, the optimisation is first run with help of a simple mock-up function instead of the database. This mock-up function is a simple circle that moves up and down as a function of the forward slope. It expands with banking, while banking is assumed to always be positive. The propulsion limits are the same as in the database. The outcome of this run is used as the initial guess for the real run. As problems were experienced with banking, banking was introduced gradually. First, a solution was found where 0% banking was taken into account. Then this solution was used as an initial guess for a run where 20% banking was taken into account. This cycle was repeated until a solution was found for the road with 100% of its banking.

5.4. results

In this section the outcomes of the two minimum-time optimisations are compared to four trials of the fastest cyclist from the L218 study (of those trials, the data was complete at segment 6 at the very least). The results were checked for global optimality, but this cannot be guaranteed (see appendix F). First, the general results will be discussed. After that, some interesting segments will be looked upon in more detail. Detailed results of all segments can be found in appendix G. For segment 6, results of the separate minimum-time optimisation are presented, so that braking strategies can be compared.

5.4.1. total descent

trajectory-

The optimal trajectory is the combination of two logical strategies. For lower speeds, the shortest possible route is taken. For higher speeds, the largest turn radius is created such that the cornering speed is the highest cornering speed possible. Looking at figure 5.2, this is confirmed by the optimiser. There are two differences between the measured trajectory and the calculated optimal trajectory.

[1] The author of Adigator has been notified of the bug.

1. On relatively straight segments, the optimal trajectory switches from the right side to left side of the lane quicker than the cyclist.
2. The optimal trajectory gets closer to the right lane boundary than the cyclist, sometimes even touching it.

The first difference theoretically yields a non-optimal solution for the optimisation. The shortest distance would be covered when the lateral displacement is stretched over a distance that is as long as possible. Instead, this is done is a shorter distance than possible. Still, the optimiser marks this as the optimised output. One possibility is that the proposed trajectory is due to the inaccuracy of the road measurement data. The calculated curvature might deviate from the actual curvature. When calculated curvature is larger than the actual curvature, the model will try to cut a (slight) turn that does not actually exist.

The second difference is probably due to a combination of several factors. First of all, a cyclist needs some lateral space to be able to control the bicycle in case of an unexpected perturbation (think of sudden wind, a bump in the road) or steering errors. Secondly, the road quality at the side of the road is often worse than in the middle of it. Degradation, plant growth, sand and puddles can often be found there. Both of these factors also explain why only the right side of the lane is avoided by the cyclists; the left side of the lane is the center line of the two-lane road. The cyclist can use the other lane to make steering corrections and the road quality is also often good there.

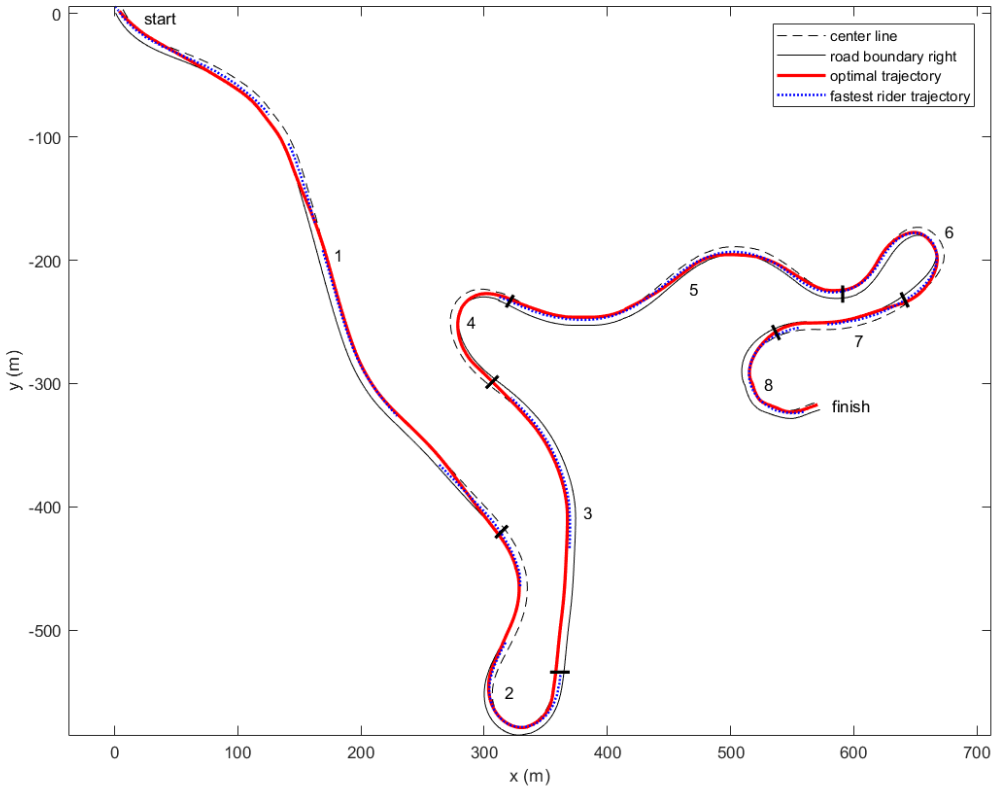

Figure 5.2: Top view of the trajectory (red) of the cyclist on the right lane of the L218, which was modelled with a constant width of 6.7 meters. The GPS data of the cyclist is plotted in blue dots.

velocity profile-
The velocity profile shows multiple strange outcomes (figure 5.3).

1. In segment 2 and 4, the optimal velocity is much higher than the measured velocities.
2. In segment 3 and 4, the measured velocities are extreme and the rate of change is very high.

For outcome 1, there can only be two explanations. Either the minimum-time optimisation has an error somewhere, or the track data variables were inaccurate. As for the track data, the curvature data, banking data, twist angle data and friction coefficient have the largest influence on the maximum cornering speed. When the used curvature is lower than it actually is, the maximum cornering speed will be higher in the optimisation than in reality. When the used twist angle

and banking angle are larger than they actually are, the same effect is seen. The curvature used in segment 2 and 4 are both around 0.03, or a radius of 33 meters. Calculations show that the maximum cornering speed is about 15 m/s. The optimised cornering speed is higher. The twist angle was recorded to be small, such that it does not influence the cornering speed. The banking angle is 2 degrees, this too is not of great effect. It could be that the road was locally in such condition that the friction coefficient was very different from the final segments of the track, where the calculated cornering velocities are realistic. As a conclusion, the track data needs to be checked. If that does not explain the optimal velocity profile, there might be an error in the model.

As for the second strange outcome, the velocities measured in segment 3 and 4 cannot be correct. To accelerate from less than 10 m/s to 30 m/s within 100 meters requires a huge amount of power (more than 4000 W). Even when using their absolute maximum power, this cannot be executed by the riders at all. This leads to the conclusion that the acceleration measurements (from which the velocity can be found) are incorrect. The acceleration data is measured with an IMU with axial accelerometers. The acceleration data received by the author was already filtered into the three fixed inertial axis directions. The IMU however records the accelerations in the frame of the IMU. Built-in functionalities recalculate the accelerations in the correct directions, using gravity as a reference.

There are also some results that show great correspondence with the velocity measurements.

1. In segment 1, the velocity profiles overlap. This indicates that total propulsion limit is correct. The individual estimations of power output, drag area, and elevation might still be somewhat incorrect.
2. In segment 6 and 8, about the same maximum cornering speeds are reached. This indicates that the turns are handled well by the optimiser.

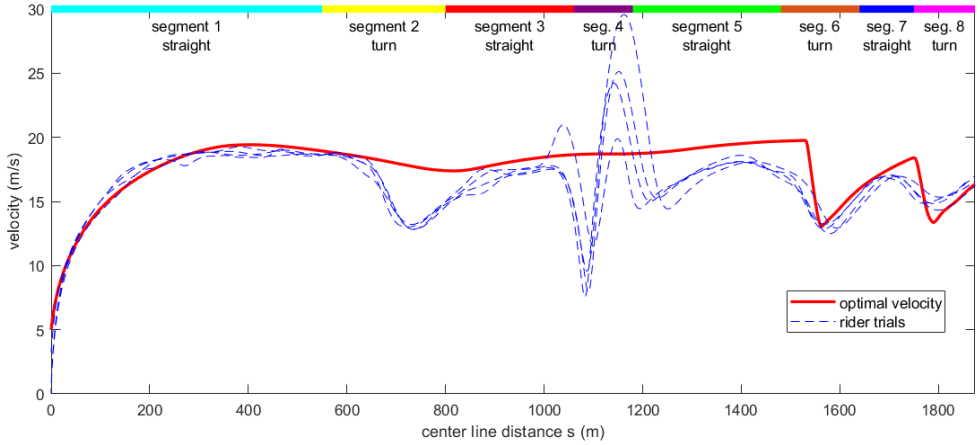

Figure 5.3: The optimal velocity profile compared to the rider trials.

g-g diagram comparison-
In this thesis, the so called numerical method was used to describe g-g diagrams. Following this method, theoretical acceleration limits are found making use of the steady motion equations. It has been used in several studies [19, 48]. Another method that is used is the experimental method. In this method, acceleration data is simply plotted, and a g-g diagram is fitted around it. The data can also be gathered by simulation using a vehicle and driver model, as done by Ni et al [39]. The downside of using the experimental method is that it is unknown why certain acceleration limits exist. To validate the g-g diagram model for cyclists, a comparison was made between the experimental and numerical g-g diagrams. For this, the acceleration measurements taken at the L218 study were compared to the found optimised accelerations.

The resulting comparison shows much correspondence (see figure 5.4). Almost all data points fall within the predicted acceleration limits. There are however several points that lie outside of the predicted g-g diagram. The points above the diagram might come from power peaks, but the accelerations are generally so high that it would be impossible to produce them with physical power alone. The acceleration data is prone to errors, so it is expected that there will be more extreme accelerations than happened in reality. The part of the g-g diagram that is not filled is the bottom. This is expected, since the bottom of the diagram is where the largest risks are. Too much longitudinal braking can cause a stoppie to happen, and combined cornering and braking can cause slipping when overdone. It is surprising to see that in pure lateral acceleration, the cyclists dare to get close to the maximum acceleration limits. Still, there is room to improve their performance within the acceleration limits.

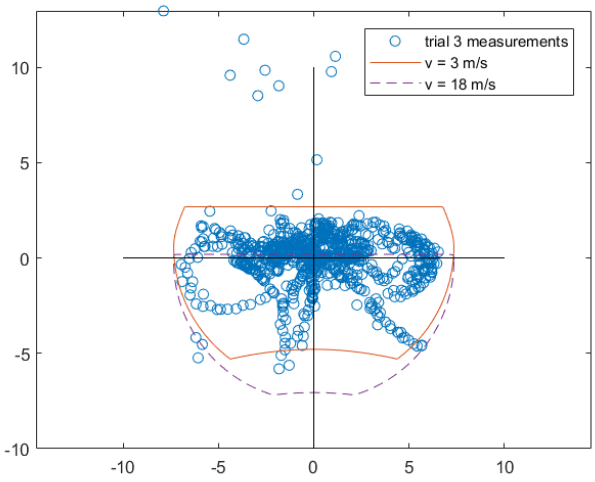

Figure 5.4: The experimental g-g diagram compared to the numerical g-g diagrams. The diagrams were created using the average slope, and zero banking.

metrics-
A third way to compare the outcome of the minimum-time optimisation to the measurements is through the previously mentioned metrics (results can be found in table 5.1). As expected, the optimal descent time is shorter than that of the measurements. The fastest measured descent time was 114 seconds, this is a difference of a little more than 7 seconds: 6 % of the total descent time. From the velocity profile however it could be seen that this comes partly from the strangely high cornering velocities in segment 2 and 4. Time spent on decelerating was much lower in the optimal strategy, following the Pontryagin Maximum principle. Time spent on acceleration is also lower. Due to the absence of braking in segments 2 and 4, the maximum velocity is reached for a large part of the descent, and further acceleration is impossible (mainly due to air drag). In the measurements cyclists do break in those segments and have to accelerate again. This likely causes the difference in time spent on acceleration.

Table 5.1: The scores for the performance metrics for the optimal control strategy and the measurements from the trials (n = 4) for the full track.

	optimal strategy	mean measurements	std measurements
% s decelerating	15.95%	34.15%	3.87 %
% s accelerating	39.47%	52.25%	3.32%
descent time (s)	106.9	118.8	2.2

To look further into the events at segment 2 and 4, those segments will be discussed in more detail.

5.4.2. segment 2

Segment 2 of the descent contains a left hairpin turn. In this segment, the optimal cornering velocity was found to be much higher than in the measurements. To look into this, the trajectory, velocity profile and the g-g diagram are discussed in more detail.

trajectory-
The optimal trajectory has one remarkable difference from the measured trajectories: the turn is exited at the inside, instead of at the outside of the lane (figure 5.5). This behaviour is not expected for such tight turns. For a tight turn, it is often efficient to ride in the largest possible turn radius, in order to maximize the cornering speed. It indicates that the maximum cornering velocity that is calculated by the optimisation model might be even higher than the measured cornering velocity. Furthermore, as indicated earlier, the optimal trajectory touches the right lane boundary while the cyclist does not even get close to it. The cyclists needs a lateral control safety margin, which the optimisation does not take into account.

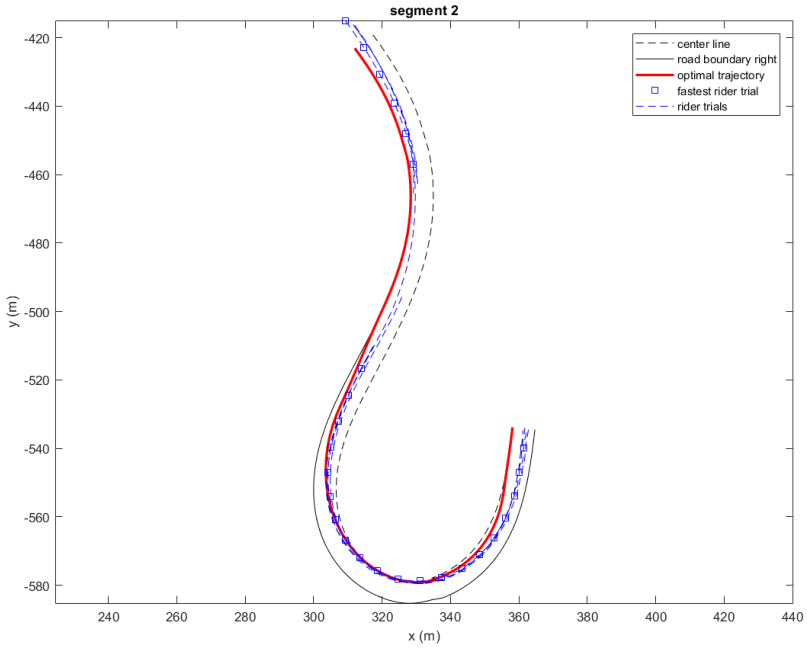

Figure 5.5: The optimal trajectory compared to the measured trajectories in segment 2.

velocity profile-
When looking at the velocity profile (figure 5.6), the same conclusion can be drawn as when looking at the trajectory; the calculated cornering speed is much higher than the cyclists dare to reach. Still, some deceleration is seen in the optimal velocity profile. It does however not relate to the turn, as the optimal velocity keeps decreasing even after the apex of the turn. This deceleration is causes by a decrease in forward slope (from 4.3 deg to 1.6 deg) that started in segment 1. This reduces the propelling effect of gravity and therefore lowers the acceleration limit and the maximum possible velocity.

g-g diagram-
This numerical g-g diagram shows where the differences in the velocity profiles come from (see figure 5.7). The optimal cyclist does not brake in the segment. The measurements show braking during the right turn, the straight part and the left turn. The only parallelism is found in the cornering; both plots show that turns happen. The g-g diagram confirms that there is something wrong with either the model or the track data that it has been fed. The measurement data shows the continuity of the measurements beautifully; the sequence of the control actions can be followed by following the line of dots.

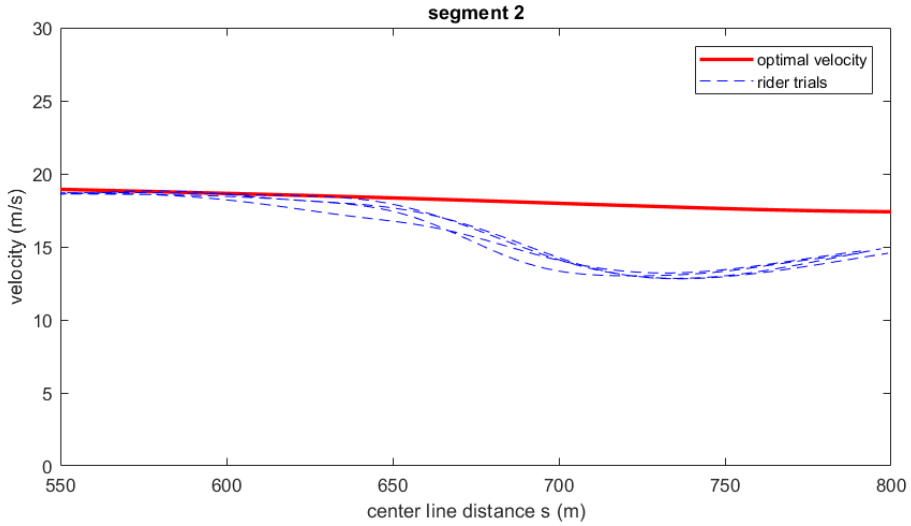

Figure 5.6: Comparison of the optimal velocity to the measured velocities in segment 2.

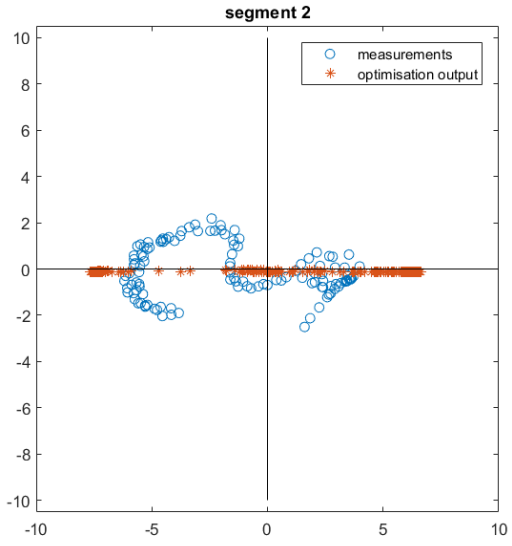

Figure 5.7: The numerical g-g diagram compared to the optimal controls for segment 2.

5.4.3. segment 4

Segment 4 is a sharp tun to the right. In this turn, the velocity measurements are incorrect. Furthermore, the optimal cornering velocity is much higher than expected for the curvature.

trajectory-

The optimal trajectory differs from the single GPS trajectory record that was not disturbed (figure 5.8). The GPS signal was lost because of all the trees surrounding the road in this segment. The cyclist crossed the road center line, to the left (forbidden) half. While the optimisation was constrained to find a solution within the lane boundaries, one still would expect the optimal trajectory to approach the measured trajectory. This is not the case; the optimisation shows the complete opposite. The optimised trajectory does not show an effort to enlarge the turn radius in order to increase the cornering velocity. As discussed previously, this is either caused by the track data or an error in the minimum-time optimisation model. To find out which of the possibilities is true, the track data is reviewed once more in the discussion (section 5.5).

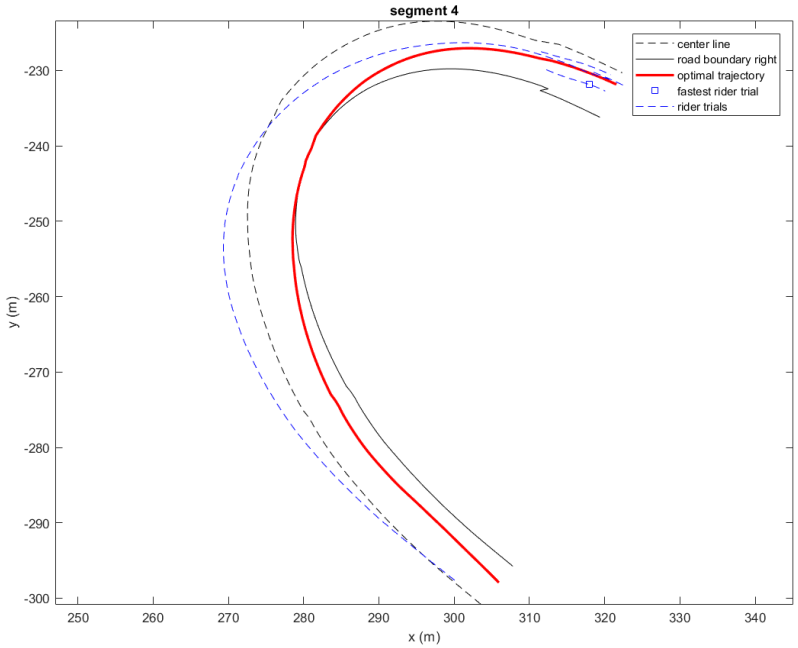

Figure 5.8: The optimal trajectory compared to the measured trajectories in segment 4.

velocity profile-

The velocity profiles do not look alike at all (see figure 5.9). As mentioned before, the large accelerations are not humanly possible. More than 3600 W would be needed to reach them. It is therefore certain that measurement or filtering errors were made. Common difficulties of IMU's connected to bicycles include the effect of roll on the measurements. It couples the measurements of the vertical and lateral accelerations (seen in the $\mathcal{D}$ frame). This would however result in virtually lower lateral accelerations than actually happen. In this figure however, higher accelerations are seen. To check the velocity measurements, the velocity data was derived from the GPS data as well. This shows the same high accelerations as the IMU data. At the end of the segment, the velocity is suddenly lower. It is unclear why.

g-g diagram-

The g-g diagram confirms that the acceleration measurements must be incorrect, as the accelerations shown are as large as 10 m/s^2 (see figure 5.10). Such high accelerations are impossible to reach for a car on a road with a friction coefficient of 0.75, let alone a cyclist who cannot deliver close to such power. Since the measurements are off, it is impossible to compare the accelerations of the cyclist and the theoretically optimal accelerations. However, it was still expected that braking is required in such a tight turn. The solution of the optimal control problem does not include braking in this segment.

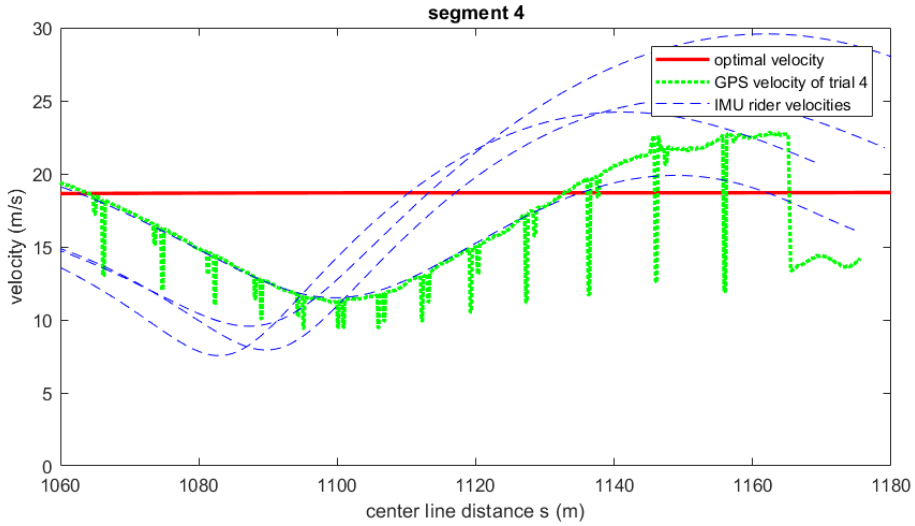

Figure 5.9: Comparison of the optimal velocity to the measured velocities in segment 4. Additionally, the velocity as derived from the GPS data is shown.

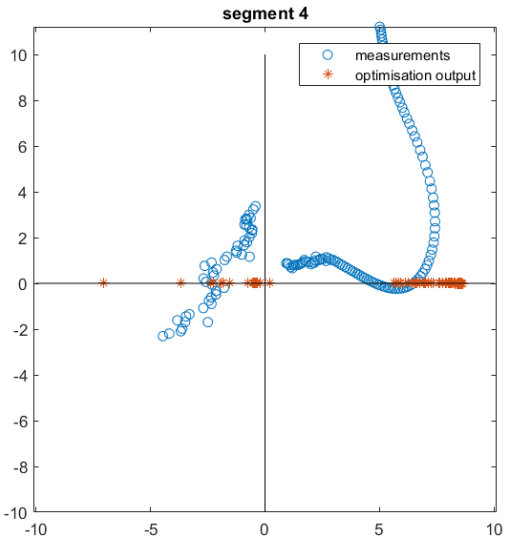

Figure 5.10: The numerical g-g diagram compared to the optimal controls for segment 4.

5.4.4. segment 6 - detailed optimisation

In this section, the separate optimisation of segment 6 will be discussed. The initial velocity of this optimisation was set to the entry velocity at segment 6 of the fastest rider trial. This is done in order to be able to compare the strategies better (e.g. the segment time), as the entry velocity of segment 6 in the full descent optimisation was much higher than the entry velocity of the cyclists.

trajectory-

The optimal trajectory shows a wider turn radius than that of the cyclists (figure 5.11). The distance with respect to the track boundary is much smaller, leaving no space for control actions. The trajectory of the fastest total descent trial is also the trajectory which is the most similar to the optimal trajectory. This confirms the profit of the strategy.

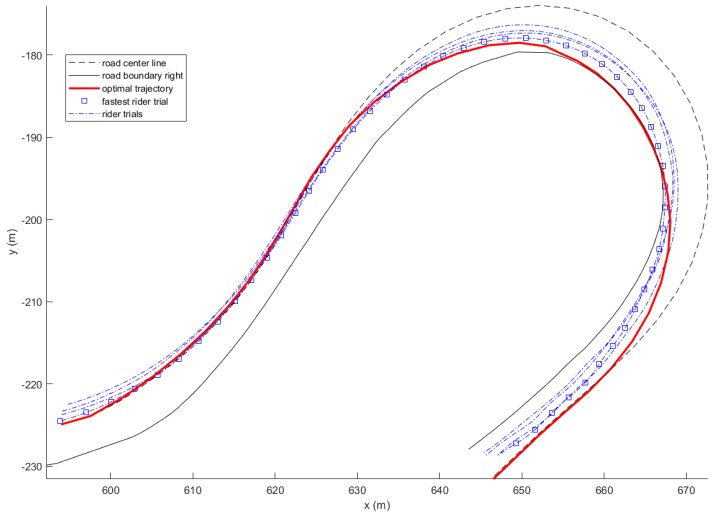

Figure 5.11: The optimal trajectory. The cyclist has a power limit of 500 W, and the friction coefficient is 0.75. The optimal trajectory touches the inside of the turn earlier, and shows a wider trajectory at the end of the turn. This way, the turn radius can be maximized. The fastest trial that is indicated, is from the fastest overall trial (the best overall performing cyclist).

g-g diagram comparison-

The g-g diagram shows a few outliers in the measured data (see figure 5.12). Those are due to measurement errors (as again, the accelerations are higher than possible for cyclists). Otherwise, the accelerations are comparable. The strategy of the cyclists is more conservative. The lateral acceleration capability is not fully used, and the cyclists decelerate two times slower than the optimisation deems possible. The lateral acceleration difference can come from safety margins, or from a possible error in friction coefficient estimation.

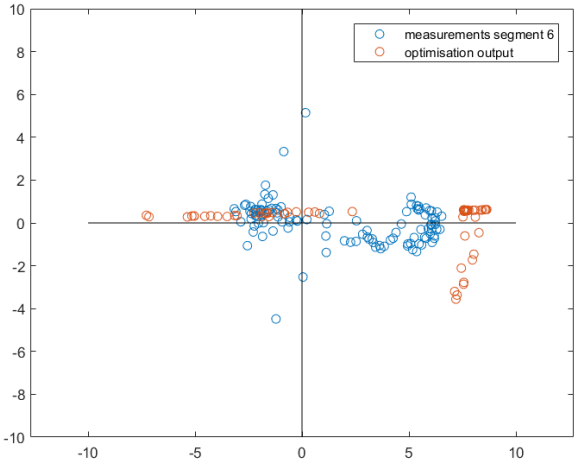

Figure 5.12: The measured longitudinal and lateral accelerations compared to the optimal accelerations.

velocity profile-
The optimal velocity profile differs a lot from the measured profiles 5.13. Braking is initiated later, stopped earlier and a lot more braking force is used. Due to the optimal braking strategy applied in the model, the adherence radius is larger than for front brake use only. Therefore, this effect was expected. The most unexpected difference is the fact that the minimum speed is reached much more early in the turn. At the graph of the lateral acceleration (the third graph of figure 5.13) it can be seen that earlier in the turn the lateral acceleration as carried out by the optimal cyclist is lower than the acceleration at the point of the turn where the curvature is the largest. Since the cyclist is braking, there can be less lateral acceleration due to the circular shape of the diagram. Therefore the third figure shows that the cornering strategy follows the acceleration limits. What's more, is that cyclists can either handle more lateral acceleration later in the turn than they think, or the friction coefficient was estimated wrongly. In the discussion, this will be analysed further. In figure 5.14 it is again shown that the minimum velocity is reached very early in the turn.

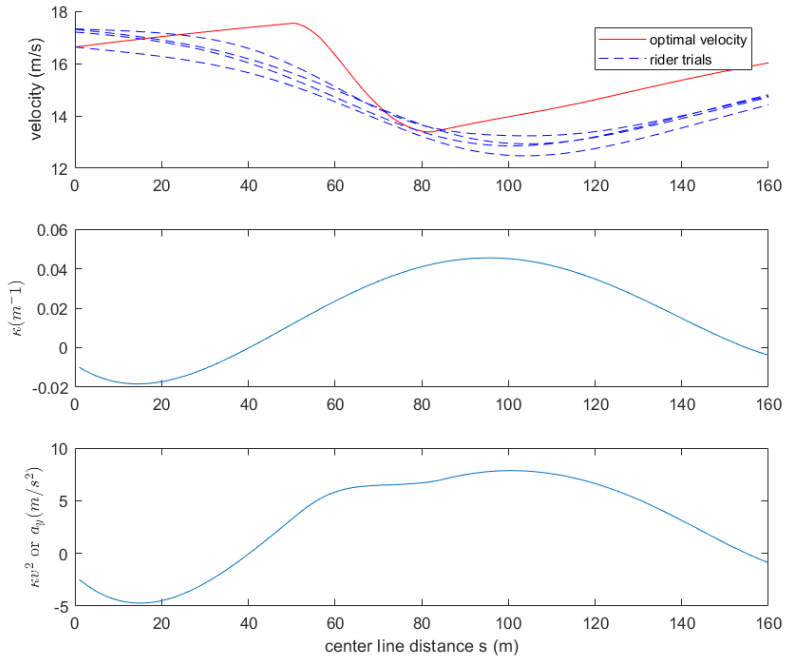

Figure 5.13: (1) The optimal velocity profile. Braking is initiated later and stopped earlier, reaching the minimum velocity earlier in the turn. From the slope of the velocity profiles at the end of the segment can be seen that the used power was estimated well. The optimal cyclist is able to accelerate as fast as the elite cyclists. (2) The curvature of segment 6. (3) The lateral acceleration as acted out by optimal the cyclist.

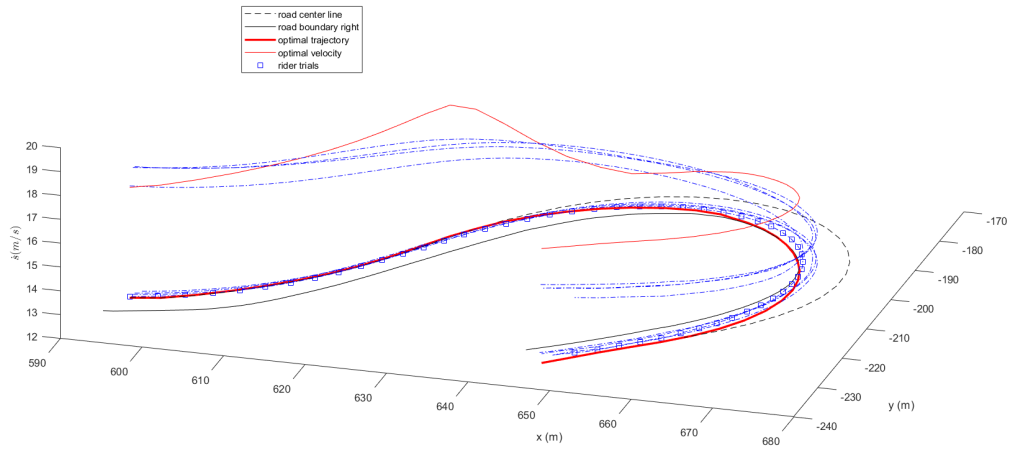

Figure 5.14: The optimal trajectory as well as the optimal speed shown together. The minimum speed is reached at an early point in the turn, especially compared to the elite cyclists.

metrics-
The scores of the performance metrics all show that the optimal control performance is indeed better. A significant time difference is measured: the optimisation 15% is faster. This shows that there is room for much improvement. It should be noted that this time reduction is not realistic, since no safety margins were built in the optimisation, while humans do use safety margins. However, it is expected that even when adhering to safety margins, time savings can be made, since the time difference is so large. The time difference is reflected in the metric that indicates the percentage of time spent on deceleration. The optimal cyclist spends as little time as possible on deceleration. Spending less time on decelerating means that more time is available for acceleration. Furthermore, every metric confirms that the optimal control performance is better than the performance of the cyclists.

Table 5.2: The scores for the performance metrics for the optimal control strategy and the measurements from the trials (n=4).

	optimal strategy	mean trials	std. dev. trials
time	9.47 s	11.12 s	0.20 s
exit speed	16.04 m/s	14.70 m/s	0.177 m/s
% time decelerating	15%	57%	<1 %
mean velocity	15.58 m/s	14.47 m/s	0.27 m/s

5.5. discussion

In this discussion, three main subjects will be discussed. The first is about the strange behaviour that showed in segment 2 and 4. The optimal velocity profile showed unexpected high velocities. The questions is whether the model is mistaken, or the inputs for the model (track, cyclist, environmental parameters) are incorrect. The second subject is the optimal braking and cornering strategy. How does it differ, and can cyclists perform better than they do now? Lastly, the convergence towards a local minimum of the cost function will be discussed.

5.5.1. braking anomalies

One of the goals of this case study was to find out if the minimum-time optimisation model works as expected. In the results, a large difference between the measurements and the optimisation output was found. In segment 2 and 4 the cyclists break in the measurements. In the optimised results however, no braking is used and the cornering velocity is much higher than acted out by the cyclists. Why is this? To find out whether the model is faulty or not, several checks have been carried out. To start off, it is interesting to find out what the maximum cornering velocity is for segment 2 and 4 according to the optimisation.

maximum cornering velocity check-
To find out what the maximum cornering velocity is according to the model, the propelling force can be made higher. Staying true to the track properties like elevation, this can be done through reducing the drag area or increasing the available power. A reduced drag area has the most effect on high speeds. A minimum-time optimisation was run where the drag area was halved. The resulting velocity profile shows that the maximum cornering velocity is about 20 m/s for the turns in segment 2 and 4 according to the model (see figure 5.15). The minimum-time optimisation does take into account the turns, but suggests that the maximum cornering velocity is very high. Furthermore, a small bump is seen in the braking sequence in segment 2. Both the bump and the high cornering velocities are unexpected. If the model is correct, either the track data or the estimated friction coefficient are not describing reality well. First, the track data will be looked into.

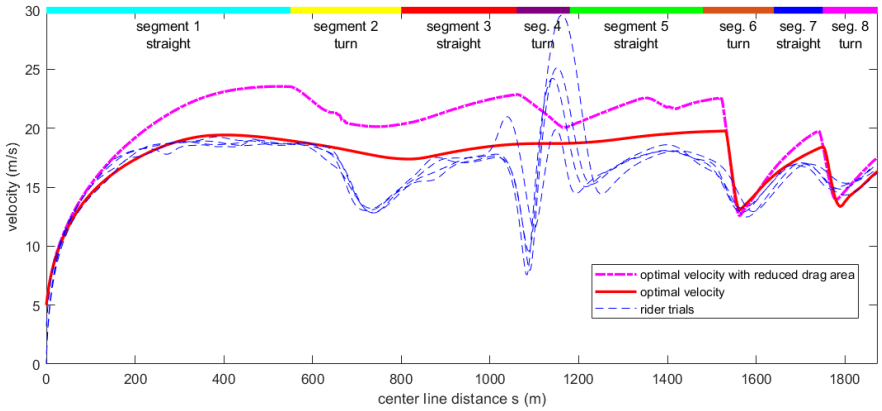

Figure 5.15: The velocity profile for a study with only half of the estimated drag area ($0.16m^2$ vs $0.32m^2$). The results show the maximum cornering velocities that did not show when the higher $C_d A$ value was applied.

track data check-
The track variable that influences the maximum cornering speed the most is the curvature. To check whether the curvature data is realistic, the curvature was plotted. From figure 5.16 it can be seen that the curvature in every segment except segments 6 and 8 is 0.03 or lower. A curvature of 0.03 equals a radius of 33 meter. When making good use of the road width, this can be extended to 39 meters. The maximum cornering speed of a flat turn with a radius of 39 m is 16.9 m/s (using the friction coefficient that is also used in the model). This is interesting, as the cyclists show a lower cornering velocity (13 m/s). This indicates that the (safe) friction coefficient as estimated by the cyclists is lower than the one used in the model. The fact that the cornering speed could be higher than 16.9 m/s according to the optimisation, can have three logical reasons: (1) the turns are positively banked, increasing the lateral acceleration capacities, or (2) the optimisation model includes an error.

To check for banking, another run was analyzed. This optimisation is the full track minimum-time optimisation, but banking is set to zero (this automatically sets beta almost to zero as well, for this specific track). The expectation is that in segment 2 and 4, the maximum cornering velocity is equal to 16.9 m/s. As visible in figure 5.17, the cornering velocity is almost equal to the expected value. In both turns, it is a little bit above it (17.4 m/s and 17.5 m/s), it could be that the largest possible riding radius was even larger than 39 m. This result shows that the minimum-time optimisation does not

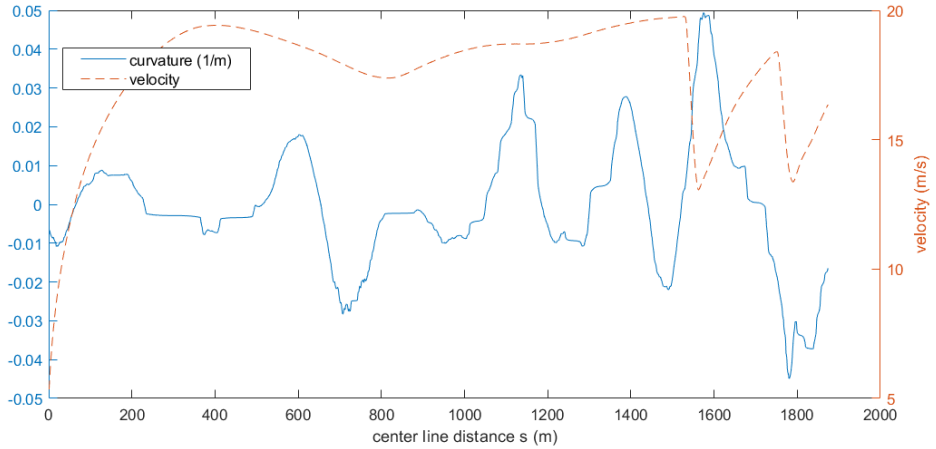

Figure 5.16: The curvature of the road as derived from the road GPS data. It is compared to the found optimal velocity profile, to see if the braking behaviour corresponds correctly to the curvatures values. Note that this is the curvature of the center line, the cyclist can enlarge the turn radius (lower curvature) by using all of the road width.

have strange errors, but behaves as expected. However, it is still unclear why the cornering velocity of the cyclists is much lower than the calculated cornering velocity. One option is that the friction coefficient as estimated by the cyclists differs from the one used in the model. To find out, the friction coefficient is analyzed next.

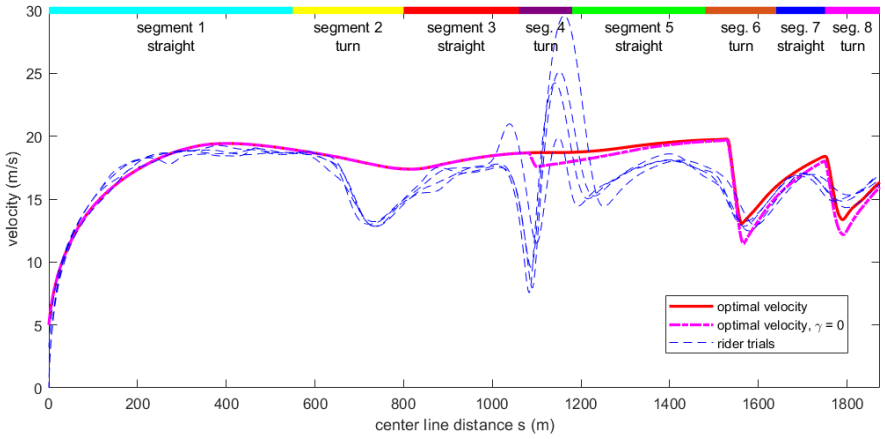

Figure 5.17: The effect of banking on the velocity profile. The red line shows the velocity profile when the banking of the road does have effect, the magenta line shows the profile when the banking has been set to zero. It is visible that segment 4, 6 and 8 have positively banked turns.

friction coefficient check-
The friction coefficient that was chosen to use in the model, was based on the information that the cyclists rode over asphalt, and the assumption that the asphalt was dry. When searching for information about the state of the track, a remark made by a rider was overlooked. He had said: "3rd or 4th corner is very wet". How this rider counts the track corners is unclear, but is clear from this remark that the road was not completely dry, and that some segments were more wet than others. To see how a rider would descent on a really slippery road ($\mu = 0.3$), another optimisation was run (see figure 5.18).

This optimisation shows a velocity profile where the cornering velocities of segment 2 and 4 are even below those measured. This means that the friction coefficient estimated by the cyclists on those segments is higher than 0.3 but lower than 0.75. A friction coefficient of about 0.5 would describe a wet road, with some safety margin. To test this hypothesis, the problem should be reformulated with a friction coefficient of 0.5 for the first 4 segments, changing to a coefficient of about 0.7 for the last segments. The presented approach however uses a fixed friction coefficient over the entire length of the track. It is possible to run such a problem, by making sure that the adherence radius database is switched when a certain center line distance is reached. It was not done in this project, as new databases should be produced to do so, and this costs a lot of time.

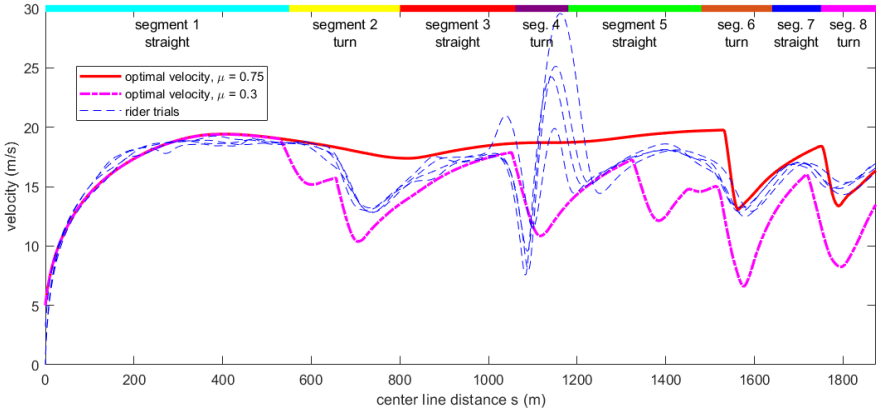

Figure 5.18: The resulting velocity profile of a run where the friction coefficient was lowered to 0.3 (indicating a very slippery road).

Next to the expected braking events that now show for segment 2 and 4, some extra braking events are seen that were not measured. In segment 2, extra braking is initiated before the sharp turn initiates. Before the sharp turn, there is a turn to the right with a smaller turn radius. The fact that the cyclists did not break for this turn is because their estimated friction coefficient is higher than 0.3. In segment 5, two extra braking events can be seen. The first shows a cornering velocity that is almost equal to the one in segment 4. This is surprising, as on a first glance the right turn that is positioned in segment 5 has a much larger turn radius. The curvature data however shows a curvature of 0.027 for the turn in segment five, while the one in segment 4 has a curvature of 0.030. This indicates that the curvature estimation of segment 5 is too high with respect to the rest of the calculated curvatures. The second (smaller) braking event can be linked to a left turn, that comes right before the sharp turn in segment 6. At this distance over the track, the friction coefficient has increased (as can be seen by the correspondence between results of the high friction coefficient and the measurements) and the cyclists can easily take this small turn without having to decrease their velocity.

With this analysis it was shown that the friction coefficient applied in the optimisation was much higher than the friction coefficient estimated by the cyclists, for segment 2 and 4. A remark made by a professional cyclist during the measurements confirms this. However, alongside a difference in friction coefficient estimation, there could have been one extra factor that created the difference in cornering velocities between the cyclists and the optimisation: the road width.

road width-
The road width was modelled with a constant value of 6.7 m, since convergence was problematic when taking into account the variable road width. This value of 6.7 meters was chosen according to the maximum road width in segment 6. The real road width is sometimes more narrow, however. To investigate the difference road width can make, a test was run with segment 6. In the test, three different road widths were taken into account: a fixed road width of 6.7 meter, and half of that road width taken both at the right and at the left side of the lane. The resulting velocity profile can be seen in figure 5.19.

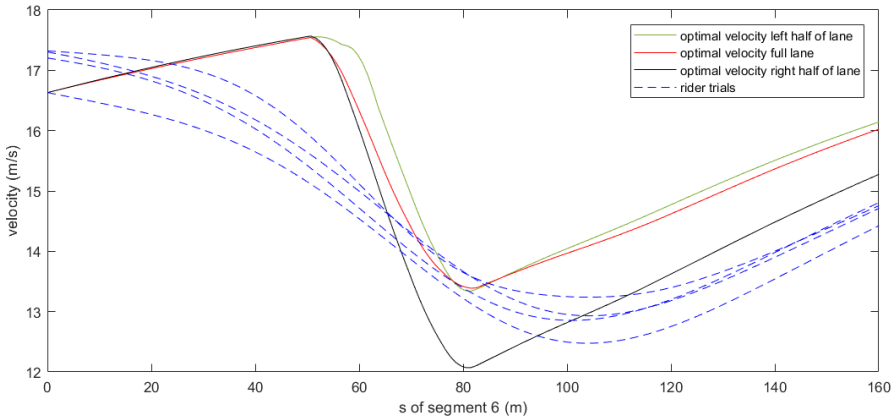

Figure 5.19: The velocity profiles resulting of three different road width configurations of segment 6.

The results show how much difference road width can make. The cornering velocity that results from cornering at the inside half of the road is much lower than than that of the full road width. The difference is almost 2 m/s, more than 10

percent of the total speed. Cornering at the inside half of the road reduces the turn radius spectacularly. The difference between cornering velocities experienced by riding on the side of the lane that is positioned towards the outside of the turn and riding on the full width lane is non existent. The turn radius is approximately the same in both these cases, but on the outside of the turn more path distance (not center line distance) is covered. This is why it seems like the rider can brake harder in the latter scenario in figure 5.19, but actually he covers more path length in the same center line distance, which means that he probably brakes just as hard as in the normal situation. The extra path length also explains the late braking. The turn is effectively shifted a few meters, so that the initial braking point is shifted. The center of the turn is still at the same center line distance however, so the moment of lowest velocity is reached roughly at the same point. This road width analysis shows that the optimiser takes road width into account in a correct way. Furthermore, it is shown that road width can have a large effect on the outcome, and that working with the exact road width at s could possibly result in a velocity profile more alike the ones measured.

conclusion-
As a conclusion, the model reacts to track and rider conditions as expected. The track data used to run the optimisation seems to be reasonable. The friction coefficient applied in the model was much higher than the friction coefficient estimated by the cyclists, for segment 2 and 4. A remark made by a professional cyclist during the measurements confirms this. A combination of an estimated friction coefficient difference and the absence of accurate road width variation over the track together cause the difference found between the measured and optimised velocity profiles.

5.5.2. braking strategy

One of the main goals was to find out if the optimal cornering strategy differs from strategies practised by elite cyclists. There are two main differences. (1) The location in the turn where minimum velocity is reached differs greatly. This is for example visible in segment 6, in figure 5.14. Even when cyclists would brake harder, their timing is wrong according to the optimisation. But (2) the most striking dissimilarity between the strategies is the magnitude of braking, as seen specifically in the results of segment 6. The optimal deceleration for segment 6 is almost two times higher than the performed deceleration. Why is this? There are three main factors can cause a difference in braking performance:

1. front brake only vs optimal braking
2. friction coefficient estimation
3. safety margins

Of those three, the friction coefficient has already been discussed. The other two factors are further looked into.

front brake vs optimal braking-
When the front brake only strategy is used, there is a smaller adherence radius possible when turning and braking at the same time (see figure 5.20). This can prevent cyclists from reaching the optimal decelerations shown in the minimum-time optimisation solution.

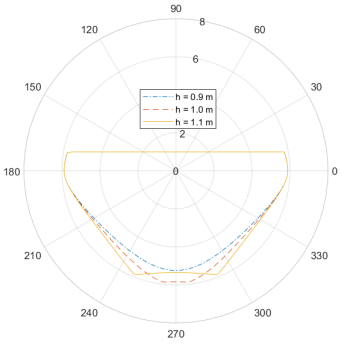

Figure 5.20: A g-g diagram of a front brake only strategy, where the height of the CoM was varied. The diagram shows that the adherence radius is not maximized when turning and braking happen at the same time.

safety margins-
It was discussed that cyclists brake less hard than what the optimisation deems possible. The hypothesis was that this is partly caused by safety margins that the cyclists unconsciously use. To look further into the concept of safety margins, a study was done where approximations of safety margins are applied. There are at least two types of safety margins that can be thought of. First of all, a control safety margin. To be able to control a bicycle when a perturbation is experienced (this can be as simple as an unexpected bump in the road or a strong breeze of wind) some lateral space is necessary. This makes it possible to steer as a response to the perturbation. In a study by Schwab and Meijaard it was found that the

minimum lateral distance necessary to control a bicycle when perturbed is 15 cm from the center line of the movement [9]. The perturbations used in this study were not large, so in reality the distance that cyclists want to take from the road boundary might be even larger. The second safety margin is a safety margin for acceleration. When seeking the lateral acceleration limits, a cyclist risks slipping when a road condition is slightly different than expected. When braking, an uncontrolled stoppie is risked. It is difficult to estimate at which points of the g-g diagram the safety margins are largest. It is however clear that for pure acceleration, there is no safety margin.

To model those two safety margins, a simple approach was used. For the lateral positioning safety margin, the study of Schwab and Meijaard had shown that a cyclist should stay clear from the roadside with at least 15 cm. When looking at the measured trajectories, cyclists stay clear at least 0.5 m from the side of the road. Therefore, the right road boundary was reduced with 0.5 cm from the center line. The left road boundary was left unchanged, as there is another lane of the road on that side that allows for lateral control actions. The acceleration safety margin was applied through shrinking the g-g diagram radius by $1.2 m/s^2$, except for the forward acceleration part (see figure 5.21).

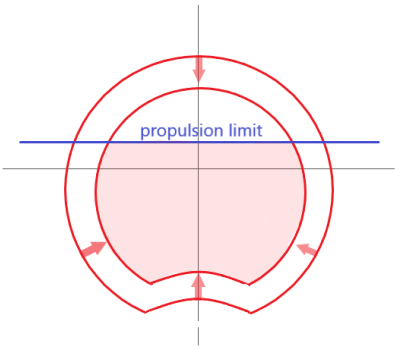

Figure 5.21: The safety margins as implemented. The power limit is left untouched.

There was no optimal solution found for the study, instead a maximum number of iterations was reached (6000). The absolute errors of the variables are small compared to the variables values. The results of this study show that the safety margins only partly explain the difference in performance between the measurements and the optimised descent. The total descent time was 106 seconds without safety boundaries, and 108 seconds with safety boundaries. The cyclists fastest time was 114 seconds. In figure 5.22 it is seen that the general trajectory does not differ much.

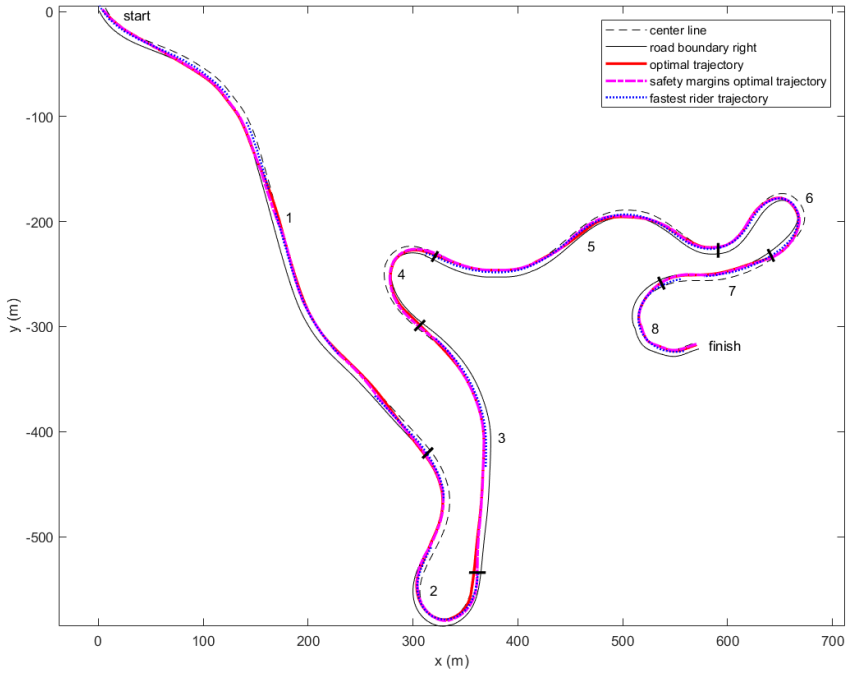

Figure 5.22: The resulting trajectory from the minimum-time optimisation where safety margins are approximated.

The velocity profile shows the expected differences (see figure 5.23). The safety margins lower the maximum cornering speed, but in the turns in segment 2 and 4 no difference is seen at all. This makes sense, since the calculated maximum cornering velocity is around 20 m/s. The safety margins do not lower the cornering velocity enough to change the velocity profile with respect to the base results. This is confirmed by the results for segment 6 and 8. There it is seen that the cornering velocity is only reduced by about 2 m/s, which means that velocity in segment 2 and 4 is still lower than the reduced maximum cornering velocity. In segment 6 and 8 it is also seen that the cyclists can brake harder than they did, while adhering to the safety margins. This indicates that the safety margins are larger in the longitudinal direction than in the lateral direction. The fact that the only velocity profile difference is seen at segment 6 and 8, means that the time difference of 2 seconds between the two optimisation runs comes almost solely from the performance in two turns. When a more precise friction coefficient is taken into account, the effect of safety margins is expected to play a role in the performance in the turns of segment 2 and 4 as well. This means that safety margins have a significant effect on performance. Getting cyclists to reduce their safety margins even slightly can make the difference between winning and losing. The great question is then how to distinguish between a necessary safety margin and one which is falsely exaggerated.

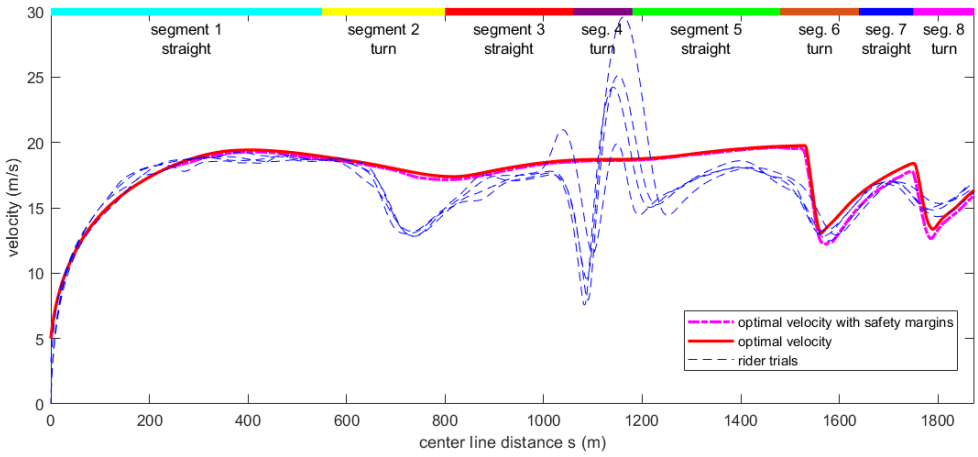

Figure 5.23: The velocity profile that results from the minimum-time optimisation where safety margins are approximated.

5.5.3. convergence

One of the outcomes of this case study is that the model has a lot of difficulty with convergence. After a few tests most of the difficulty appeared to be caused by the banking and twist angle. This is why the results were obtained in several steps, as explained in the method section. This convergence behaviour is curious, as there were little problems with the elevation angle, compared to the banking and twist angle. Both the elevation angle and banking angle cause a shift of the diagram. However, while a gradual change in forward elevation can only lead to gradual changes in the optimal solution (for example gradual changes in braking intensity/timing), banking can lead to sudden changes. An example: negative banking can cause two almost equally good options (a local minimum). Negative banking causes the cyclist to lose normal force in the corners. This lowers the maximum cornering speed. If it is critically lowered, it could be that the optimal trajectory is suddenly different; the turn radius should be increased, instead of decreased as much as possible. Those two opposing tactics can result in convergence errors. The opposite can be said for positive banked corners.

This hypothesis implies that due to increased banking, results suddenly change a lot. To investigate this, a test is run where the banking is set to zero. The results are compared to the baseline case study results where banking is included. The resulting trajectories were exactly equal. This shows that a sudden switch in optimal tactics did probably not happen when increasing the banking. In figure 5.24 it can be seen that in segment 6 and 8, larger cornering velocities can be reached due to banking. However, this velocity change is a gradual change, that evolves with the banking rather than change suddenly. As a conclusion, the theory that banking effected convergence because it can create a sudden 'switch' in optimality was not confirmed. There might be other underlying reasons why banking caused problems with convergence for this case study.

5.5.4. accuracy

In the method section it was described how 1000 nodes were used in the optimisation, with a maximum distance of 2.8 m between them. This amount of nodes was chosen to make sure a minimum amount of information was provided per center line distance. However, in practise this choice might fall short in describing the states accurately when interpolating in between the mesh nodes. In events where states and/or inputs change rapidly, more mesh points are needed.

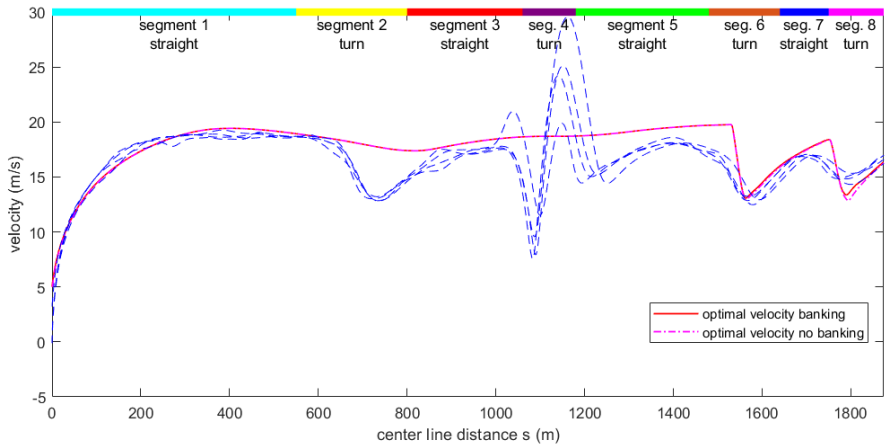

Figure 5.24: The velocity profiles of test runs that do and do not consider banking. The only difference is found during the braking sequences at segment 6 and 8.

While LGR discretisation allows for mesh refinement, mesh refinement was not used to solve this case study. To check whether the current optimisation resulting states and inputs change rapidly between sequential nodes, the largest differences were looked upon. For v this is 0.98 m/s, for n this is 0.59 m and for χ it comes down to 0.058 rad. While an orientation change maximum of 3 degrees is acceptable, the velocity change and lateral positioning changes are large. For the results, requirements can be set up that describe the maximum state differences between sequential nodes, to ensure accurate results. For the inputs, interpolation can even be a larger problem. Longitudinal acceleration can change very sudden from full propulsion to full braking. When two nodes are 2.8 m apart and the calculated inputs on those nodes are as different can be, what happens in between? It could well be that in the middle of this node interval sudden braking should be initiated. But with regular interpolation, a gradual change towards braking is calculated. This makes it hard to set a requirement for inputs, as it is possible that even between nodes that are as much as 0.1m apart, there are large differences.

When are results accurate enough? This depends entirely on what it planned with the results of the optimisation. For this case study, it makes sense to set the internodal variable change limit to a few percent of the maximum reached variable value. In the case of velocity, this could be 0.2 m/s (1% of 20 m/s). For lateral positioning 0.2 m (3% of 6.7 m), and for orientation χ a few degrees. It is however impossible to directly apply these requirements into ICLOCS2. Instead, the results need to be checked to see if they meet the requirements. To achieve higher accuracy, either more nodes can be added, or nodes can placed more strategically. Mesh refinement used both of the options at ones.

To find out if higher accuracy can be reached with the help of mesh refinement, two runs with mesh refinement were compared to one without (the original run of which the results are covered in this chapter). One mesh refinement starts with the same number of nodes as the original optimisation, 1000. The second mesh refinement starts out with only 500 nodes. The mesh refinement is carried out a maximum of 6 times per run. The results are displayed in table 5.3. Surprisingly, the mesh refinement that starts out with the least amount of nodes performs the best. The internodal changes of the parameters are generally small. The most noticeable are the values for the input changes. The maximum input changes are much lower for the second mesh refinement than for both other runs. This means that knowledge about when braking takes place exactly has improved immensely. The amount of nodes has increased drastically in segment 6 and other sharp turns, and on straight segments the amount of nodes has dropped. Why a mesh refinement that starts out with less initial nodes yields better results is unclear. It might be that it is easier for the software to correctly place the nodes than to reposition them.

Table 5.3: Differences between results from optimisations with and without mesh refinements. The mesh refinement runs have started out with different amounts of initial nodes.

	base run	mesh refinement 1 (#nodes$_0$ = 1000)	mesh refinement 2 (#nodes$_0$ = 500)
max $\lvert\Delta v\rvert$ (m)	0.98	0.80	0.68
max $\lvert\Delta\chi\rvert$ (rad)	0.058	0.107	0.088
max $\lvert\Delta n\rvert$ (m)	0.59	0.71	1.27
max $\lvert\Delta a_x\rvert$ (m/s^2)	3.18	1.83	1.7
max $\lvert\Delta a_y\rvert$ (m/s^2)	13.53	8.07	5.29
#nodes$_f$	1000	1026	737
max Δs (m)	2.8	4.6	9.18
min Δs(m)	0.53	0.0033	0.0079

5.6. conclusion

The optimal trajectory of the L218 has been defined robustly. A large difference was found between the measured and optimal velocity profile. It was established that this is mainly the result of a difference between the friction coefficient used in the model, and the friction coefficient as estimated by the cyclists. The model reacted as expected to parameter changes, qualitatively showing good results.

Furthermore, differences between braking strategies have been shown. The optimal cyclist can brake harder for a shorter period of time, even when adhering to safety margins. Next to that, the results indicate that the optimal location of the minimum velocity is positioned earlier in the corner than where cyclists locate it.

It can therefore be concluded that the model is a nice tool to help analyse cycling performance. But only when there is sufficient data and knowledge about the road, cyclist and bicycle at hand.

6

Discussion & Recommendations

In this chapter limitations of both the minimum-time optimisation as a whole and the g-g diagram model are discussed. The choice of working with the free-trajectory OCP with QSS constraints is debated. The assumptions and simplifications made in the g-g diagram model are further analyzed and recommendations are made towards a more accurate model. Furthermore, an outlook is given towards possibilities of the presented model. More suggestions for cycling scenario's where this model can be used are discussed. This is extended even further by discussing applicability for other sports. Lastly, the translation of the model results into practical instructions for rider training is explored.

6.1. chosen method review

At the start of this project, the free-trajectory OCP with steady motion constraints approach was chosen. There were two reasons for this; the method was shown to be computationally fast compared to the transient approach, and the OCP is simple. It is debatable whether the free-trajectory steady motion minimum-time optimisation approach is indeed the best approach for the case of a bicycle descent. While the approach guarantees that all of the acceleration limits are captured in a few g-g diagrams in a 2D case, the number of situation-dependent g-g diagrams that should be applied increases exponentially when looking at 3D situations. In this project, this has been handled by using multiple variable interpolation on a very large database. This is computationally slow and there is a risk of incorrectness of the found interpolated value. Therefore one of the two presumed benefits of the free-trajectory steady motion approach ended up being untrue; the computational effort is not as low as presumed. The remaining benefit is still true; the optimal control problem can be formulated with only 3 variables. For future research it would be interesting to compare the computational speeds of this approach and the transient approach, to find out how they compare for this specific use.

6.2. g-g diagram model limitations

Many assumptions were made in order to keep the g-g diagram model workable and simple. The consequences of choices made for the power model, bicycle model, mechanical rider model, behaviour rider model, tire model, aerodynamic drag modelling and road model will be discussed in this section.

6.2.1. power model

The power constraint for the g-g diagram is chosen to be a constant power limit, for simplicity reasons. However, this does not represent acceleration possibilities for cyclists well. In physical sports research, optimal power distributions are researched. The outcome is called an 'optimal pacing strategy'. They have been determined through fixed-trajectory optimal control problems. Instead of a g-g diagram as a constraint, a power or exertion model is used. An idea for a future improvement of the g-g diagram model of this project is to use the g-g diagram as a baseline constraint, and an exertion model to determine the optimal power at a certain point on the track.

Which exertion model should be used? The general belief is that exertion models that mimic more of the physiological phenomena are automatically better. The exertion model that is seen as the most advanced, is the Margaria-Morton (M-M) model [20]. From all the available models, it takes the most physiological phenomena into account. The M-M model accounts for $\dot{V}O_2$ kinetics in addition to the lactic and alactic components of anaerobic work. Therefore, it is recommended to investigate the implementation of the M-M model as an addition to the g-g diagram. However, as a first step a more simple model can be taken. While the critical power (CP) model ([33]) is often judged as oversimplified and inaccurate, a new adaptation to the model makes it a robust method of assessing exhaustion [57]. This adaptation is a model of the W' balance. W' can be seen as the work capacity available above the CP threshold. The principle is illustrated in figure 6.1. The work capacity can be imagined as a battery that can charge and drain, depending on the power expenditure of the cyclist. One great advantage of the model is the possibility to calculate the status of the W'

'battery' online, while cycling, so that it is easy to compare the optimal battery status to the actual battery status. Recently this combination of both trajectory finding and the determination an optimal pacing was explored by Zignoli & Biral [7]. This study incorporates a road model that accounts elevation (no banking), and uses the transient method to solve the optimal control problem. Their cost function tries to minimize the travel time, while also minimizing the power output variation and steering angle variation.

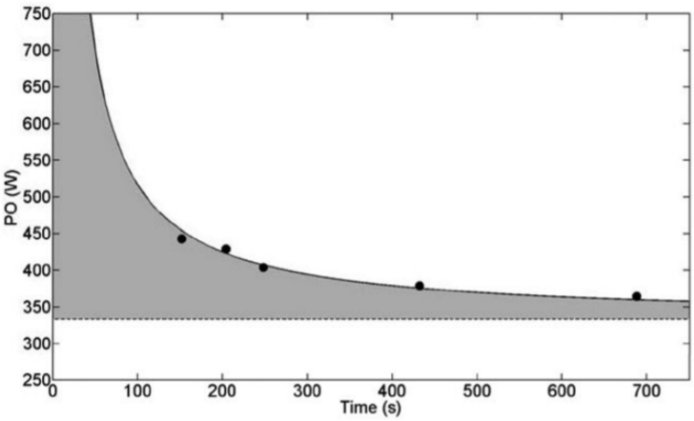

Figure 6.1: Example of the W' battery principle. The dashed line shows the critical power, and the grey area above it is the available battery capacity. The available power decreases, as the cyclist gets exhausted because it pedals 360 W, which is above their CP. Figure from [21]

As a conclusion, it is recommended to look into the use of the M-M model to include optimal pacing in the optimisation. With this addition, the minimum-time optimisation model can be used on more cases than descents only. If a more simple model is sought (e.g. as a first step) the CP model with the work capacity adaptation is recommended.

6.2.2. bicycle model

In the g-g diagram model, the bicycle and rider are represented in a very simplified way. They are modelled together as a single point mass. This simplifies the equations of motion, but makes them less accurate. Bicycle characteristics such as countersteering are completely ignored. A more elaborate way to describe the bicycle would be to describe its different parts as separate rigid bodies that interact. As established in the Whipple model [42], the bicycle can be modelled as four rigid body parts: the front and rear wheels, the main frame and the steering axis. Examples of such single-track vehicle models focused on steady state cornering are by Fu and Koenen [30, 43]. The model by Fu does not include a rider, and the model by Koenen does. Application of such models can increase the accuracy of the optimisation and make sure that bicycle characteristics such as countersteering are accounted included.

6.2.3. mechanical rider model

Next to the bicycle, the rider can be represented in more accurate ways too. Riders are modelled in several ways. They are sometimes assumed to be a point mass connected rigidly to the rear frame. As an extension of that model, the driver can be modelled as two point masses, one rigidly connected to the rear frame and one as an inverted pendulum above it. One of the most complex model used for humans as inactive controllers has two degrees of freedom:lateral position with respect to the bike and rolling rotation of the upper body [25]. Those are all possible mechanical rider models that can improve the representation of reality in the current model.

6.2.4. behavioural rider models

Next to mechanical driver models, the drivers behaviour can be modelled. Tactically changing position while cycling can influence the resulting drag area, or it can help with braking. Another example is the position of the legs while cornering. In the following sections the modelling of such behavior will be discussed.

CoM positioning-

In the g-g diagram model, the CoM positioning is assumed to be constant over the entire track distance. In reality, cyclists move a lot during a race, for multiple reasons. The cyclists positioning behaviour influences other parameters that are important in minimum time-lap simulations. One is the frontal area that is needed for the calculation of aerodynamic drag force. When a driver switches to sitting on the top tube during a straight section of the descent, the air drag changes drastically. The same effect is seen when standing up during braking. This effect was modelled by Limebeer and Leonelli

through implementing a 'prone' (accelerating) air drag and a 'standing' (braking) air drag [45]. A smooth transition between the air drags is made by a function designed by the researchers. A similar function can be used for the modelling braking behaviour. Riders often reposition their CoM to the back of the bicycle, to prevent passing the stoppie limit. This can be modelled through a brake dependent longitudinal CoM position. As a conclusion, CoM positioning influences both braking and the drag area. Modelling CoM positioning changes over the course of a track could give insights in CoM positioning strategies.

roll angle limits-
The g-g diagram model that was build in this thesis assumes that the rider has the ability to exert power while making a turn. This means that the cyclist should be able to pedal. In practise this is not always possible, as the roll angle can become so large that the pedal at the inside of the turn touches the ground. This inflicts great risks. Therefore, it is interesting to analyse the effect of a roll angle limit. This limit is only necessary when pedalling is necessary, during braking the cyclist can lift the pedal at the inside of the turn upwards so that it has more space to roll. To determine the maximum roll angle, a calculation (see appendix J) was compared to the angle reported by the US national commission on product safety [54]. The maximum roll angle was found to be 28.5 degrees.

In figure 6.2 a comparison can be seen between the g-g diagram that results from the model described in this thesis, and two different roll angle limitations. The first limitation takes into account that the roll angle is always limited, so that cyclists can corner with they inner turn foot down. This is a simple boundary condition, that implies vertical lines as constraints. The second limitation limits the roll angle only when the cyclist is pedalling during a turn. It creates an extra concave shape. This concave shape might provide more problems with convergence than the concave shape created by the stoppie limit. This is because the stoppie limit always lies in the center of the symmetry axis of the diagram, while the roll limit area does not. Since the roll limitation creates a seriously different shape at a critical location (the transition between longitudinal acceleration and pure cornering), this condition is important to take into account for future bicycle g-g diagrams.

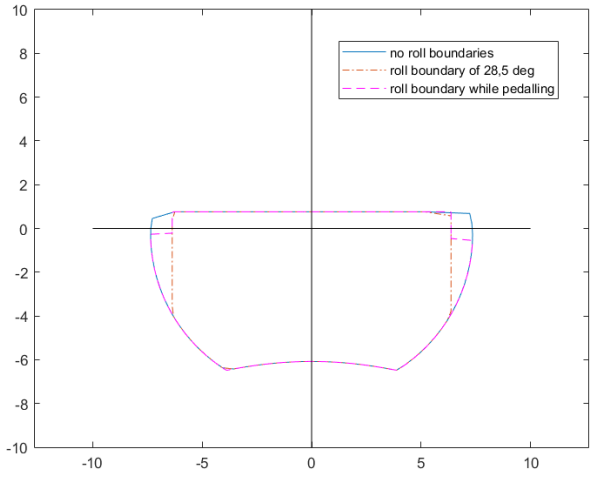

Figure 6.2: A basis g-g diagram that was created for a flat road is compared to diagrams created for the same condition, only with two different roll angle limitations added to it. The slight difference between the left and right side height of the roll limit is the result of the numeric discretisation of the adherence orientation that was applied to create the diagram.

6.2.5. tire model

The tire model forms the basis of the g-g diagram, since it determines which forces the tire can handle. In this work, a very simplified model is used. However, it is to be expected that tires are more complex in reality. As en example, effects such as roll probably result in asymmetrical diagrams, due to asymmetrical contact patch shapes. At the moment there are no bicycle tire models, but research is done on the subject by Andrew Dressel and hopefully others. An option to investigate before bicycle-specific tire models emerge, is the Pacejka motorcycle tire model [56]. While motorcycle and bicycle tires are quite different, Pacejka's model does take into account very important characteristics like the camber angle, that are left out in car tire models. It would be interesting to see the difference between g-g diagrams that result from such a model and the friction ellipse, and in the future a bicycle tire model.

While the tire model helps to predict tire force limits, a specific tire characteristic should be taken into account while con-

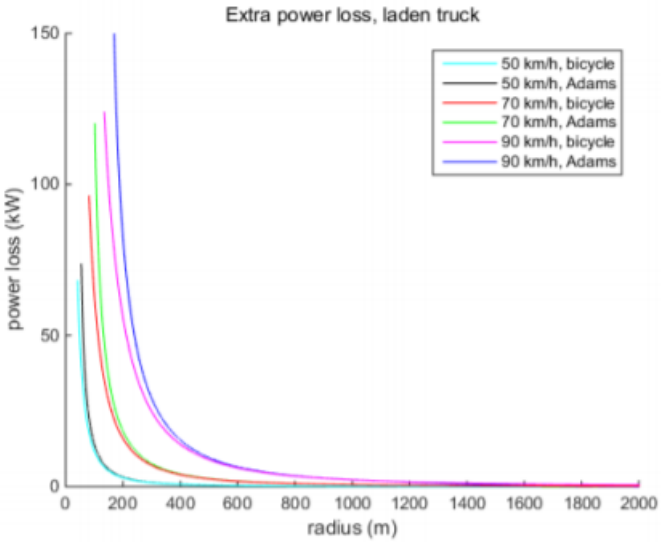

Figure 6.3: Here the effect of cornering on the power loss due to rolling resistance is seen for a heavy loaded truck. As a comparison, the total power loss (mainly caused by air drag) on a straight segment is 15 W for this truck. For a bicycle the magnitude of the rolling resistance coefficient is expected to be different (lower) due to the load difference, but the general effect is the same. Figure from [53]

sidering external forces on the bicycle model. Rolling resistance is now not taken into account. While rolling resistance is indeed very low while driving straight (0.005 time the normal force), cornering enlarges this resistance effect. The cornering force that is created when a small slip angle exists correlates directly with the magnitude of the rolling resistance coefficient [53]. An example of this effect can be seen in figure 6.3.
As a conclusion, the tire model that is chosen influences the g-g diagram greatly. The friction circle is not based on actual tire characteristics. Therefore it is recommended to apply a model that is based on tire dynamics. To enhance tire modelling further, lateral acceleration dependant rolling resistance should be applied.

6.2.6. aerodynamic drag

The influence of drag on cycling performance is huge. To quote Debraux et al. [55]:

> When cycling on level ground at a speed greater than 14 m/s, aerodynamic drag is the most important resistive force.

Aerodynamic drag is caused by a combination of pressure drag and skin friction drag. The effective frontal area (the drag coefficient times the projected frontal area), together with speed and air density, is a determinant parameter of the drag force. Where the projected frontal area describes the specific position, the drag coefficient describes the aerodynamic feasibility of that position. Both of those parameters can change over time. Next to this, wind can play a significant role. In the current g-g diagram model, aerodynamics are implemented in a rather static way. The drag is assumed to be generated by the speed of the cyclist only, without taking into account wind coming from any direction. What's more, is that a position change is not taken into account. Air density change is assumed zero. And lastly, drag reduction caused by other cyclists cycling nearby is not modelled.

This raises the question whether such effects could be implemented into the model. Currently, the (simple) equation used to calculate drag force makes use of the vehicle speed. To include wind in the longitudinal direction, the relative speed of the cyclist with respect to the speed of the wind can be used instead of the cycling speed (see equation 6.1).

$$Fd = 0.5\rho_a C_d A(v_{cyclist} - v_{wind})^2 \tag{6.1}$$

However, now the wind is modelled to blow into the longitudinal direction of the cyclist only, while the cyclist may change direction with respect to the wind. It is more complex to change the wind direction. For the current g-g diagram model, the road can be reduced to a single plane, where the orientation and position in the xy plane did not matter. When adding wind, the orientation does suddenly matter. What could be done however is determine the projection of the wind direction onto the longitudinal direction, to determine which part of the wind will work in the longitudinal direction. With this simplification, lateral wind effects will not be taken into account. Such an approach is for example used by Zignoli and Biral [7].

Due to the large effect of drag, drag reduction due to other cyclists can play a large role. There are two types of cases where such drag reduction can play an interesting role. The first is a scenario where it is known in which position the

cyclist will ride (behind or in front of other riders). Here, drag force reduction can be calculated through multiplying the drag force with a reduction percentage. In the second scenario, the riding strategy changes due to positioning choices. The trajectory and riding strategy takes into account that a cyclist could take aerodynamic advantage of both opponents and allies. Here, the positioning with respect to other riders is an OCP variable (example in figure 6.4). Due to the many options of positioning, this would make the calculation of the g-g diagram complicated. The usage of a pre-setup database is almost impossible.

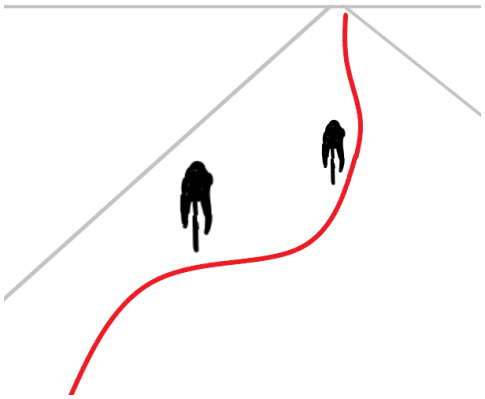

Figure 6.4: The possible optimal trajectory for overtaking manoeuvres using aerodynamic advantages.

Drag area changes due to position changes can be approximated relatively easily, as described in section 6.4.2. However, thorough knowledge of the specific rider behaviour and drag area is necessary before the drag area changes can be implemented. Along with the drag area, the center of pressure (CoP) might change. In the current model, the center of pressure was assumed to be located at the center of mass. In practise, the location might differ. Implementation of a different CoP location is simple, especially as long as it is located in the sagittal plane (symmetry).

Lastly, the air density can change over the length of the track. For this to happen, large height differences should be present. To give an idea, the air density in Colorado Springs (height of 1.84 km) is 0.94, whereas the air density at sea level is 1.20 (considering a temperature of 20 degrees Celsius in both situations) [55]. Air density will only play a role at long and steep descent routes. This is even more true when considering that the temperature at higher altitudes is often lower than at ground level. When the temperature drops, the air density increases. This effect negates some of the air density differences caused by height. In the majority of cases, the air density will not change significantly over the course of a track.

To summarize, it is possible to implement the effects of longitudinal wind. Strategies that involve multiple riders are further discussed in the outlook sections. Lastly it can be concluded that the air density can be considered constant.

6.2.7. road model

In this optimal control problem, the road is modelled as a ribbon. The ribbon road model describes the road as a "chain" of planes. It makes it easy to describe the orientation of the road and the cyclist. However, lateral road curvature is not modelled. For cycling, the author suspects that lateral curvature is small. Although it could not be checked with data for the specific L218 case, since only the center line and road boundaries were recorded.

Next to lateral curvature, another road model assumption is made. Namely, that the friction coefficient is constant over the track. In reality certain parts of the track may contain sand, or even puddles, which can drastically change the friction coefficient. If the friction coefficient changes over the length of the track, the friction coefficient could just be another input parameter for the g-g diagram model. This makes everything computationally hard, especially since the coefficient can change instantly. This will have huge effects on the convergence of the OCP. When there are lateral friction coefficient differences, it is complex to implement his.

As mentioned by Perantoni and Limebeer, the ribbon road model does not take into account short-wavelength road features [32]. Examples are small bumps or holes in the road, that can be there because of wear or tree roots. Such road distortions can cause riders to take a different trajectory because they do not want to fall over, or to slow down. The roughness can cause short moments of ground contact loss, where the cyclist won't be able to accelerate or decelerate at all. Since those moments are short, and often disturbances are small (according to the author's experience), the rider controls are not expected to differ much.

In short, for applications of this model in track cycling the most important road parameter is the friction coefficient. Lateral curvature is almost non existing on public roads, and short-wavelength road features are kept to a minimum.

The friction coefficient can however change drastically over the course of a track. To gain accurate time predictions it is recommended to map those friction changes and add those as an extra parameter in the model.

6.3. convergence

The convergence of the minimum-time optimisation is the main focus after the optimal control problem has been defined. How can performance be maximized, and how certain is it that a global optimum was found?

6.3.1. improve convergence

The convergence of the problem mainly depends on the shape and continuity of the constraint space. This is discussed in appendix D. However, the shape of the constraint space is a part of the problem definition, and cannot be changed. The user and solver settings can however influence convergence too. There are two main contributors to the convergence performance of IPOPT: a good initial guess and proper scaling [6].

initial guess-
A good initial guess is important as it can prevent the solver to get stuck in local solutions or crash and it can save a lot of time. An example of a crash can be found when an initial guess of a variable is chosen such that a division by zero is created. If the initial guess were to be any other value, this would have been prevented. The question remains, how a good initial guess should be found. In this project, the optimisation was run with mock-up path constraints first. The results from this run were then fed to the optimisation with the correct constraints, reducing the total run time significantly.

scaling-
To achieve the best solving performance, an optimisation problem should be scaled properly. But what is 'proper' scaling? Proper scaling consists of two aspects. Firstly, the magnitude of the absolute derivatives of the different variables should be about the same magnitude. For the cycling optimisation problem, this is an issue. The derivative for the velocity can generally be much larger than that of the relative orientation. The second aspect is the magnitude of the separate derivatives. The magnitude should not be very small or very large. To comprehend this, a simple Newton-Raphson problem can be thought of. In a root finding problem, a gradient approaching zero means that the tangent will never (or not within the bounded area) cross the x-axis. Almost the same holds for a very large gradient, approaching infinity. Here, the same x-value will be found over and over again.

6.3.2. global or local optimum

In principle, the solver will find a local optimum. The algorithm tries to steer towards a global optimum however, by applying a filter and a penalty function. The filter avoids cycles of iterations. It checks the iteration with respect to a part of the iteration history. In a regular situation, this enables the program to find global, rather than local solutions. Another option to guide the solver towards a global solution is to use a penalty function. The penalty function makes sure that the constraint exceedances are penalized [59]. The penalty parameter, that describes the severity of the penalty, is updated such that the cost gradient is negative.

6.4. outlook: ideas for use cases

To provide some insights in how this approach of minimum-time optimisation can be used in elite cycling, a few ideas are presented and discussed in this section.

6.4.1. multiple cyclists

In both track cycling and road cycling, an important part of strategy is determining how to overtake other cyclists. This can potentially be modelled by setting the states of one cyclist as fixed, while optimising for a second cyclist. The difficulty here is that the minimum-time optimisation is built up out of stages defined by distance s, instead of stages built up out of time instances. This means that driving behind one another is hard to model, since the cyclists drive in the same position at the same track distance s, only the time variable differs and this is generally not taken into account. Still there could be a way to model this. To do this, the lateral position of the "fixed" cyclist should be available as a function of time. To compare it to the lateral position of the second cyclist at a certain time instance, this information should be found for the second cyclist as well. The time spent on a certain distance is known as it is the outcome of the cost function. The time found for a certain distance ridden by cyclist 2 can be used to check the lateral position at cyclist 1 at the same time instance. A path cost function can be set up to compare the two:

$$|n_1(t) - n_2(t)| - d \leq 0 \tag{6.2}$$

This makes sure that at least distance d is kept laterally between the wheels of the two cyclists. Another boundary should make sure that for example the rear wheel of the first rider does not touch the front wheel of the second. This can be done by using the same path constraint, only now the lateral position of the first rider is evaluated at an earlier time instant:

$$|n_1(t-e) - n_2(t)| - d \leq 0 \tag{6.3}$$

where e describes the time distance that should be present between the two cyclists. The same can be done to make sure that the second cyclist does not move in front of the other cyclist too early. With this strategy, the model can be used to solve more strategic problems. It should be noted that aerodynamic drag plays a large role in overtaking strategies. It can be more convenient to stick behind the back of another cyclist for some time to save energy. To make optimal use of this possibility it is therefore important to incorporate both a power model and a model for aerodynamic drag, that takes into account slip streams and wakes (pressure drops behind moving cyclists, providing reduced drag for both the front and rear cyclist).

6.4.2. velodrome sprint qualifiers

In the qualifiers for the track cycling event called "sprint", the cyclist rides two or three warm up rounds. After that, the final 200 m are completed in a sprint. The tactic for this is to use the warm-up rounds to gain height, so that the cyclist can use the acceleration caused by the "drop" to the black line to initiate the final round (see figure 6.5). The interesting part about this is the drop. Which trajectory will create the fastest lap? Is it a straight line towards the center of the turn, or is it beneficial to get down to the black line very fast, to reduce the travelled distance? This model is perfect to find the solution. In this case, the value of χ is of great importance, as without it the drop effect is not taken into account. Due to the many input variables of the g-g diagram the problem will take long to solve, but it can be done. The objective is then to lower the time spent on the 200 m, and as an initial condition the position at the top of the track is given.

Figure 6.5: Natasha Hansen of New Zealand competing in the Women's team sprint qualifying during day 2 of the The UCI Cycling Track World Championships 2020, at The Veledrom, Berlin Germany. She is right in the middle of the drop. Photo from [35]

6.5. outlook: applicability rider feedback system

The possibilities of minimum-time optimisation are great. But how can the results of a minimum-time optimisation be communicated to the cyclists, in such a way that they can get the most out of it? A discussion with Rado Dukalski, PhD candidate in the field of feedback solutions in sports, was held to explore the possibilities.

First of all, it needs to be established what the most important information is for the cyclist. Since the cyclist has its own idea of how to perform optimal, it is a logical choice to focus on differences between this idea and the outcome of the minimum-time optimisation. In the case study of chapter 5, we have seen that there are several differences between what the rider does and what he should do: the trajectory is different, and the braking behaviour. Specifically, the location of the minimum velocity and the duration of braking.

Secondly, a way of communicating should be found. While augmented reality (for example glasses that add layers of information to reality) would be a way to safely show the optimal trajectory, it is very complicated and costly to build this in practise. State-of-the-art image recognition is necessary to line up the ever-changing angle of the horizon with the trajectory images. Recognition of depth is even more complex. Estimating depth from a single image was only successfully implemented since this year (2020) [62]. This makes it complex and costly to implement augmented reality. Other options should be lookud upon. Since many cyclists use their phone on their bike along with ANT+ or apps like Strava and Training Peaks, using that phone for communication is a possibility. Dukalski has used a phone as a feedback device to help cyclists with pacing. The results showed that participants adhered better when an aggregated presentation of data was given (see figure 6.6). One brainstorm outcome was to show a short (3 sec) video of the approach of a turn during an earlier straight segment of the route.

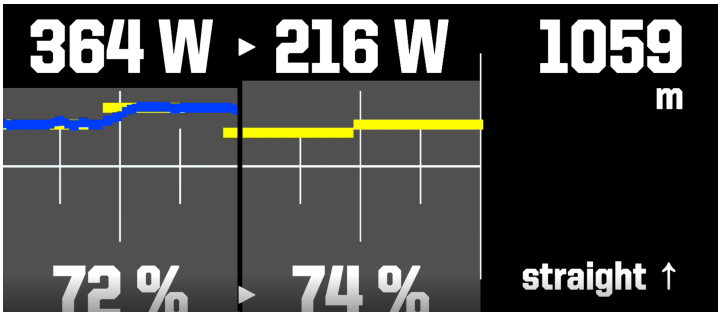

Figure 6.6: Aggregated information presentation as used in the study by Dukalski et al. On the left the past and present power output as well as goal power output is seen. In the center, the present and future power output goal is seen. On the right, navigation information is visible. The color scheme was chosen for high contrast and lack of value attribution. Figure from [58]

One of the main discussion points was whether the cyclist needs to know a goal velocity or a goal power output. Cyclists generally have a good feeling of how a certain wattage feels, while estimating velocity is harder. However, in certain conditions (like during a braking procedure) there is no power output while the velocity is still important.

As a conclusion, several instructions for the cyclist are needed, making communication complex. Researching which base instructions can be used to effectively inform the cyclists is an interesting project on it's own. A possible option for the communication of those instructions is through a phone, mounted on the bike.

6.6. outlook: extension to other sports

As this minimum-time optimisation approach was converted from formula-1 and motorcycle racing to cycling and to 3D, there might be possibilities to use this model or an adaptation in other sports as well. With the current model (one without a power model), the most relevant sports are downhill sports. Sports like bobsledding, skeleton and luge can be considered. For these sports, a different track model is necessary since lateral curvature is an important aspect of it. There are no such optimal control models right now for those sports. An analysis was conducted by Gong et al based on simulations, which shows correlations between certain control strategies and descent times [15]. But this does not show the optimal trajectory, and that is where the minimum-time optimisation model presented in this model can be of help.

Another sport where descent plays an important role is mountain biking. However, the fact that the bike loses ground contact often makes it impossible to use this model. One of the consequences of working with g-g diagrams is the automatic assumptions that there is always ground contact. Furthermore, the dexterity of mountain bikers is much higher than that of cyclists in other cycling categories. Due to this dexterity, the location of the CoM moves a lot and this should be modelled.

7

Conclusion

A free-trajectory steady motion optimal control model for the descent of elite cyclists was presented. This model is among the first generation of free-trajectory cycling optimisation models. It is the first to take into account all important 3D road aspects such as elevation, banking, and the change of gradient. As constraints, the model features g-g diagrams that depend on the current rider states and local road geometry. Those g-g diagrams are the first g-g diagrams that are determined specifically for bicycles. When comparing the numerical g-g diagrams to experimental data, they show great correspondence. This indicates that the numerical g-g diagrams represent reality well.
The model was shown to robustly predict comparable trajectories to those of elite cyclists. It contributes to the understanding of cycling acceleration limits, varying with both the vehicle states and track configuration. The model is fit to be used for descents specifically, since the power output of the cyclists was simplified. To summarize, the overall model is promising, and shows qualitative correspondence to reality.

The most important recommendation is to add a power model to the optimisation. With this addition, the model can be used in multiple categories of bicycle racing. It would be possible to predict the optimal strategies for track cycling, road cycling and time trials while calculating the optimal trajectory and their mutual effects at the same time. When aerodynamic effects of drafting are taken into account, it is also possible to use the model for team events or events where riders are riding closely together.

It is debatable whether the free-trajectory steady motion approach is the best for this case. Where it provides calculation simplicity and a decrease of calculation time for a 2D road case, for 3D it gets complex anyway. For a 3D case there are 9 variables for the g-g diagram that likely change over the track distance, where there is only 1 for the 2D case. In many cases some of the variables can assumed to be zero or fixed, for example when the road has almost no banking. A comparison to a transient model could be made to establish which one is faster. A benefit of the steady motion model is that the g-g diagrams give insight in the acceleration capabilities for a specific situation.

With this kind of models, elite cycling performances can be improved further. The model results can be used for training purposes, theoretical gear optimisation, and gear selection for specific courses. Next to that, a better understanding of the currently existing racing strategies can be created. The model paves the road towards more advanced cycling analytics.

Bibliography

[1] G. Cusimano V. Bulsink A. Cooke B. Koopman A. Doria, M. Tognazzo. Identification of the mechanical properties of bicycle tyres for modelling of bicycle dynamics. *Vehicle system dynamics*, 51(3):405–420, 2013.

[2] A. Rahman A. Dressel. Measuring sideslip and camber characteristics of bicycle tyres. *Vehicle system dynamics*, 50 (8):1365–1378, 2012.

[3] A.L. Schwab A. Dressel, J. Papadopoulos. Bicycle tire measurements and steady-state models, for use in vehicle dynamic simulations. In *International Tyre Colloquium, 4th, 2015, Guildford, United Kingdom*, 2015.

[4] J. Hauser A. Rucco, G. Notarstefano. An efficient minimum-time trajectory generation strategy for two-track car vehicles. *IEEE Transactions on Control Systems Technology*, 23(4):1505–1519, 2015.

[5] T. Masuda A. Shinagawa, H. Nozawa. Data analysis of motorcycle in a motard race. In *Proceedings, Bicycle and Motorcycle Dynamics 2019 Symposium on the Dynamics and Control of Single Track Vehicles*. BMD2019, 2019.

[6] L.T. Biegler A. Wächter. On the implementation of an interior-point filter line-search algorithm for large-scale nonlinear programming. *Mathematical programming*, 106(1):25–57, 2006.

[7] F. Biral A. Zignoli. Prediction of pacing and cornering strategies during cycling individual time trials with optimal control. *Sports Engineering*, 23(1):1–12, 2020.

[8] A. Rahman A.E. Dressel. Measuring dynamic properties of bicycle tires. In *Symposium on Dynamics and Control of Single Track Vehicles*. Proceedings of Bicycle and Motorcycle Dynamics, Delft the Netherlands, 2010.

[9] J.P. Meijaard A.L. Schwab. Assessment of the necessary width of a bicycle lane by means of multibody simulations on a bicycle-rider system.

[10] Y. Toparlar T. Andrianne B. Blocken, T. van Druenen. Aerodynamic analysis of different cyclist hill descent positions. *Journal of Wind Engineering and Industrial Aerodynamics*, 181:27–45, 2018.

[11] D. Crolla B. Siegler, A. Deakin. Lap time simulation: Comparison of steady state, quasi-static and transient racing car cornering strategies. Technical report, SAE Technical Paper, 2000.

[12] Bill Boston Bicycles. Bottom bracket ht., 2014. URL `http://www.billbostoncycles.com/bottom_bracket_height.htm#:~:text=With%20170%20mm%20cranks%2C%20a,are%20using%20170%20mm%20cranks.`

[13] Bicycling. Are tour de france riders healthy?, 2018. URL `https://www.bicycling.com/training/a20004655/1/#:~:text=No%20surprise%20here%2C%20Tour%20riders,just%20132%20to%20145%20pounds.`

[14] Bikefit. Bicycle stance width and q factor: Origins, examples, and solutions, 2018. URL `https://blog.bikefit.com/bicycle-stance-width/`.

[15] S. Turnock E. Rogers C. Gong, C. Phillips. Analysis of performance indices for simulated skeleton descents. *Procedia engineering*, 147:712–717, 2016.

[16] D. Casanova. On minimum time vehicle manoeuvring: The theoretical optimal lap. 2000.

[17] V. Cossalter. *Motorcycle dynamics*. Lulu.com, 2006.

[18] Cyclist. Bike fit variables: No. 3 wheelbase, 2018. URL `https://www.cyclist.co.uk/in-depth/5444/bike-fit-variables-no-3-wheelbase`.

[19] D. Williams D. Metz. Near time-optimal control of racing vehicles. *Automatica*, 25(6):841–857, 1989.

[20] M. Tinnsten D. Sundström, P. Carlsson. Comparing bioenergetic models for the optimisation of pacing strategy in road cycling. *Sports engineering*, 17(4):207–215, 2014.

[21] J.J. de Koning D.A. Noordhof, P.F. Skiba. Determining anaerobic capacity in sporting activities. *International journal of sports physiology and performance*, 8(5):475–482, 2013.

[22] T. Dahmen. Optimization of pacing strategies for cycling time trials using a smooth 6-parameter endurance model.

[23] A.V. Rao D.J.N. Limebeer. Faster, higher, and greener: vehicular optimal control. *IEEE Control Systems Magazine*, 35 (2):36–56, 2015.

[24] G. Perantoni D.J.N. Limebeer. Optimal control of a formula one car on a three-dimensional track—part 2: Optimal control. *Journal of Dynamic Systems, Measurement, and Control*, 137(5), 2015.

[25] R.S. Sharp D.J.N Limebeer. Bicycles, motorcycles, and models. *IEEE Control Systems Magazine*, 26(5):34–61, 2006.

[26] A.E. Dressel. *Measuring and modeling the mechanical properties of bicycle tires*. PhD thesis, The University of Wisconsin-Milwaukee, 2013.

[27] A. de La Fortelle F. Altché, P. Polack. A simple dynamic model for aggressive, near-limits trajectory planning. In *2017 IEEE intelligent vehicles symposium (IV)*, pages 141–147. IEEE, 2017.

[28] M. Piccinini F. Biral. Path planning and control of self-driving vehicles at the limits of handling. *thesis*, 2019.

[29] R. Lot F. Biral. An interpretative model of gg diagrams of racing motorcycle. In *Proceedings of the 3rd ICMEM International Conference on Mechanical Engineering and Mechanics. Beijing, Repubblica Popolare Cinese, Ottobre*, pages 21–23, 2009.

[30] H. Fu. Fundamental characteristics of single-track vehicles in steady turning. *Bulletin of JSME*, 9(34):284–293, 1966.

[31] D.J.N. Limebeer G. Perantoni. Optimal control for a formula one car with variable parameters. *Vehicle System Dynamics*, 52(5):653–678, 2014.

[32] D.J.N. Limebeer G. Perantoni. Optimal control of a formula one car on a three-dimensional track—part 1: Track modeling and identification. *Journal of Dynamic Systems, Measurement, and Control*, 137(5):051018, 2015.

[33] S. Gordon. Optimising distribution of power during a cycling time trial. *Sports Engineering*, 8(2):81–90, 2005.

[34] A. Gray. Osculating circles to plane curves. *Modern Differential Geometry of Curves and Surfaces with Mathematica,*, pages 111–115, 1997.

[35] Mitchell Gunn/Espa-Images. The uci cycling track world championships, velodrom, berlin, germany. 27 february 2020, 2020. URL `https://sportsphotographer.photoshelter.com/gallery-image/Latest-images/G0000.2AT607zz4s/I0000h5O0AcSvgII`.

[36] V. Hanacek. Hairpin turn on stelvio pass mountain road free photo. URL `https://picjumbo.com/hairpin-turn-on-stelvio-pass-mountain-road/`.

[37] Issi. Pedal stance width—and why it's important, 2016. URL `https://rideissi.com/articles/stance-width-and-why-its-important`.

[38] G.J. Olsder A.L. Schwab J. De Jong, R. Fokkink. The individual time trial as an optimal control problem. *Proceedings of the Institution of Mechanical Engineers, Part P: Journal of Sports Engineering and Technology*, 231(3):200–206, 2017.

[39] X. Li B. Xu J. Zhou J. Ni, J. Hu. Gg diagram generation based on phase plane method and experimental validation for fsae race car. Technical report, SAE Technical Paper, 2016.

[40] K.M. Powell W. Cole T.F. Edgar J.D. Hedengren, J.L. Mojica. Apopt and bpopt: New nlp and minlp solvers for differential algebraic systems with benchmark testing, 2012. URL `https://apm.byu.edu/prism/uploads/Members/minlp_apopt_informs2012.pdf`.

[41] J.D.G. Kooijman A.L. Schwab J.K. Moore, M. Hubbard. A method for estimating physical properties of a combined bicycle and rider. In *International Design Engineering Technical Conferences and Computers and Information in Engineering Conference*, volume 49019, pages 2011–2020, 2009.

[42] A. Ruina A.L. Schwab J.P. Meijaard, J.M Papadopoulos. Linearized dynamics equations for the balance and steer of a bicycle: a benchmark and review. *Proceedings of the Royal society A: mathematical, physical and engineering sciences*, 463(2084):1955–1982, 2007.

[43] C. Koenen. The dynamic behaviour of a motorcycle when running straight ahead and when cornering. Technical report, 1983.

[44] E. Kreyszig. Differential geometry, 1991.

[45] D.J.N. Limebeer L. Leonelli. Optimal control of a road racing motorcycle on a three-dimensional closed track. *Vehicle System Dynamics*, pages 1–25, 2019.

[46] Cycling Power Lab. Cycling aerodynamics, 2018. URL `https://www.cyclingpowerlab.com/CyclingAerodynamics.aspx`.

[47] M. Tanelli L. Fabbri M. Corno, S.M. Savaresi. On optimal motorcycle braking. *Control Engineering Practice*, 16(6): 644–657, 2008.

[48] M. Massaro M. Veneri. A free-trajectory quasi-steady-state optimal-control method for minimum lap-time of race vehicles. *Vehicle System Dynamics*, pages 1–22, 2019.

[49] M.S. Seif M.A. Yengejeh, H. Mehdigholi. Planing craft modeling in forward acceleration mode and minimisation of time to reach final speed. *Ships and Offshore Structures*, 10(2):132–144, 2015.

[50] J.P. Meijaard. Modelling and simulation of longitudinal tyre behaviour. In *Non-smooth Problems in Vehicle Systems Dynamics*, pages 161–170. Springer, 2009.

[51] A.L. Schwab M.M. Reijne, D.J.J. Bregman. Measuring and comparing descend in elite race cycling with a perspective on real-time feedback for improving individual performance. In *Multidisciplinary Digital Publishing Institute Proceedings*, volume 2, page 262, 2018.

[52] M. Gadola N. Dal Bianco, R. Lot. Minimum time optimal control simulation of a gp2 race car. *Proceedings of the Institution of Mechanical Engineers, Part D: Journal of Automobile Engineering*, 232(9):1180–1195, 2018.

[53] H. Olofson. Rolling resistance during cornering-impact of lateral forces for heavy-duty vehicles, 2015.

[54] United States. National Commission on Product Safety. *Industry Self-regulation: Supplemental Studies*. Number v. 2. 1970. URL `https://books.google.nl/books?id=nYiI9jotxX0C`.

[55] A.V. Manolova W. Bertucci P. Debraux, F. Grappe. Aerodynamic drag in cycling: methods of assessment. *Sports Biomechanics*, 10(3):197–218, 2011.

[56] H. Pacejka. *Tire and vehicle dynamics*. Elsevier, 2005.

[57] A. Vanhatalo A.M. Jones P.F. Skiba, D. Clarke. Validation of a novel intermittent w model for cycling using field data. *International journal of sports physiology and performance*, 9(6):900–904, 2014.

[58] A.L. Schwab P.J. Beek F.M. Brazier R. Dukalski, S. Lukosch. Exploring the effect of pacing plan feedback for professional road cycling. In *Multidisciplinary Digital Publishing Institute Proceedings*, volume 49, page 58, 2020.

[59] J. Nocedal D. Orban R.A. Waltz, J.L. Morales. An interior algorithm for nonlinear optimization that combines line search and trust region steps. *Mathematical programming*, 107(3):391–408, 2006.

[60] D.A. Alianello R.S. Rice. A driver characterizing function, the gg diagram. *CAL Report No. VJ-2882-K*, 1970.

[61] M. Massaro M. Peretto S. Bobbo, V. Cossalter. Application of the “optimal maneuver method” for enhancing racing motorcycle performance. *SAE International Journal of Passenger Cars-Mechanical Systems*, 1(2008-01-2965):1311–1318, 2008.

[62] L. Wolf S. Gur. Single image depth estimation trained via depth from defocus cues. In *Proceedings of the IEEE Conference on Computer Vision and Pattern Recognition*, pages 7683–7692, 2019.

[63] L. Pomeroy S. Moss. *Design and behaviour of the racing car*. W. Kimber, 1963.

[64] R. Capitani C. Annicchiarico T. Novi, A. Liniger. Real-time control for at-limit handling driving on a predefined path. *Vehicle System Dynamics*, pages 1–30, 2019.

[65] H. Winner T. Völkl, M. Muehlmeier. Extended steady state lap time simulation for analyzing transient vehicle behavior. *SAE International Journal of Passenger Cars-Mechanical Systems*, 6(2013-01-0806):283–292, 2013.

[66] R. Lot L. Fabbri V. Cossalter, M. Da Lio. A general method for the evaluation of vehicle manoeuvrability with special emphasis on motorcycles. *Vehicle system dynamics*, 31(2):113–135, 1999.

[67] C. van Trigt. Exploring bicycle braking during a descent (msc thesis), 2019.

[68] HP Wizard. Tire friction and rolling resistance coefficients, 2012. URL `http://hpwizard.com/tire-friction-coefficient.html`.

[69] S. Yamamoto. Optimal pacing in road cycling using a nonlinear power constraint. *Sports Engineering*, 21(3):199–206, 2018.

A

Acceleration calculations

In section 2.3, it is shown how the state equations are found that describe the change of position and orientation of the cyclist. This appendix provides a detailed elaboration of the exact calculations. It was stated that through the transport theorem, the accelerations of the cyclist can be described like in equation A.1, with the angular velocity build up out of the relative angular velocities of the frames.

$$\begin{bmatrix} a_x \\ a_y \\ a_z \end{bmatrix} = \begin{bmatrix} \dot{v} \\ 0 \\ 0 \end{bmatrix} + {}^{D}\boldsymbol{\omega}_{D/N} \times \begin{bmatrix} v \\ 0 \\ 0 \end{bmatrix} \tag{A.1}$$

$$\boldsymbol{\omega}_{D/N} = \boldsymbol{\omega}_{D/B} + \boldsymbol{\omega}_{B/C} + \boldsymbol{\omega}_{C/N} \tag{A.2}$$

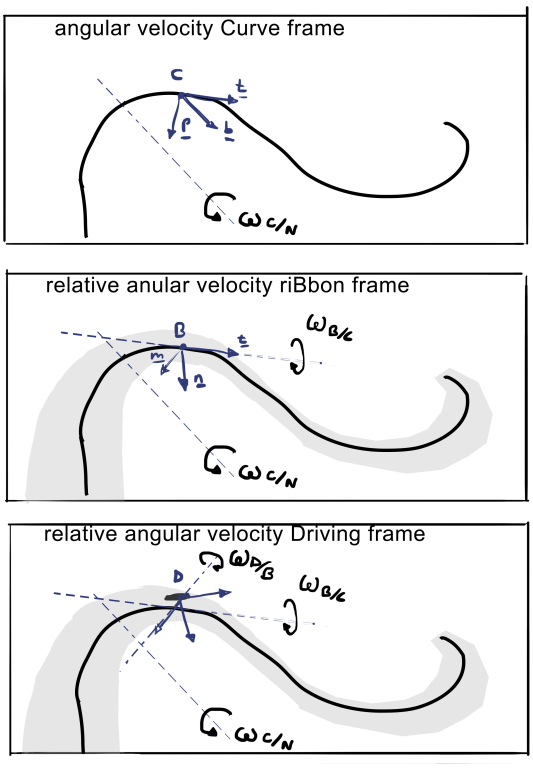

Figure A.1: Build up of the angular velocity vector, out of the relative angular velocity vectors of the frames, from i$\mathcal{N}$ertial frame to $\mathcal{D}$riving frame.

Here $\boldsymbol{\omega_{C/N}}$ can be seen as the angular velocity of the center line or curve frame with respect to the i$\mathcal{N}$ertial frame. $\boldsymbol{\omega_{B/C}}$ can be seen as the twist angular velocity of the ri$\mathcal{B}$bon frame with respect to the $\mathcal{C}$urve frame, and $\boldsymbol{\omega_{D/B}}$ is the angular velocity of the $\mathcal{D}$riving frame with respect to the ri$\mathcal{B}$bon frame, that is a result of the change of the angle χ.

$$ {}^{D}\boldsymbol{\omega}_{C/N} = \frac{\dot{s}}{\rho}\,{}^{D}\mathbf{R}_{C}\,{}^{C}\boldsymbol{b},\ {}^{D}\boldsymbol{\omega}_{B/C} = \dot{\beta}\,{}^{D}\mathbf{R}_{B}\,{}^{B}\boldsymbol{t},\ {}^{D}\boldsymbol{\omega}_{D/C} = \dot{\chi}\,{}^{D}\boldsymbol{m} \tag{A.3} $$

The rotations are all defined according to the right hand rule. The rotation matrices that describe the rotations mentioned in equation A.3 can therefore be defined in the following way:

$$ {}^{B}\mathbf{R}_{C} = \begin{bmatrix} 1 & 0 & 0 \\ 0 & \cos(\beta) & \sin(\beta) \\ 0 & -\sin(\beta) & \cos(\beta) \end{bmatrix},\ {}^{D}\mathbf{R}_{B} = \begin{bmatrix} \cos(\chi) & \sin(\chi) & 0 \\ -\sin(\chi) & \cos(\chi) & 0 \\ 0 & 0 & 1 \end{bmatrix} \tag{A.4} $$

For clarity, the unit vectors $\boldsymbol{b}$, $\boldsymbol{t}$ and $\boldsymbol{m}$ in their respective frames are given as well.

$$ {}^{C}\boldsymbol{b} = \begin{bmatrix} 0 \\ 0 \\ 1 \end{bmatrix},\ {}^{B}\boldsymbol{t} = \begin{bmatrix} 1 \\ 0 \\ 0 \end{bmatrix},\ {}^{D}\boldsymbol{m} = \begin{bmatrix} 0 \\ 0 \\ 1 \end{bmatrix} \tag{A.5} $$

Now the angular velocity vectors can be found. To find the expression for $\boldsymbol{b}$ in the $\mathcal{D}$ frame, successive rotation matrices are used.

$$ {}^{D}\boldsymbol{\omega}_{C/N} = \begin{bmatrix} \cos(\chi) & \sin(\chi) & 0 \\ -\sin(\chi) & \cos(\chi) & 0 \\ 0 & 0 & 1 \end{bmatrix} \begin{bmatrix} 1 & 0 & 0 \\ 0 & \cos(\beta) & \sin(\beta) \\ 0 & -\sin(\beta) & \cos(\beta) \end{bmatrix} \begin{bmatrix} 0 \\ 0 \\ \frac{\dot{s}}{\rho} \end{bmatrix} = \frac{\dot{s}}{\rho} \begin{bmatrix} \sin(\chi)\sin(\beta) \\ \cos(\chi)\sin(\beta) \\ \cos(\beta) \end{bmatrix} \tag{A.6} $$

$$ {}^{D}\boldsymbol{\omega}_{D/C} = \begin{bmatrix} \cos(\chi) & \sin(\chi) & 0 \\ -\sin(\chi) & \cos(\chi) & 0 \\ 0 & 0 & 1 \end{bmatrix} \begin{bmatrix} \dot{\beta} \\ 0 \\ 0 \end{bmatrix} = \dot{\beta} \begin{bmatrix} \cos(\chi) \\ -\sin(\chi) \\ 0 \end{bmatrix} \tag{A.7} $$

$$ {}^{D}\boldsymbol{\omega}_{D/C} = \begin{bmatrix} 0 \\ 0 \\ \dot{\chi} \end{bmatrix} \tag{A.8} $$

The total angular velocity vector for the rider with respect to the inertial frame can then be calculated by adding the found angular velocity vectors.

$$ {}^{D}\boldsymbol{\omega}_{D/N} = \begin{bmatrix} \frac{\dot{s}}{\rho}\sin(\chi)\sin(\beta) + \dot{\beta}\cos(\chi) \\ \frac{\dot{s}}{\rho}\cos(\chi)\sin(\beta) - \dot{\beta}\sin(\chi) \\ \frac{\dot{s}}{\rho}\cos(\beta) + \dot{\chi} \end{bmatrix} \tag{A.9} $$

Filling this information in into equation A.1, the accelerations are determined. a_x is a function of $\dot{v}$, y is a function of $\dot{\chi}$ and a_z is not a function of the derivatives of the state variables, only of the geometry at a specific situation.

$$ \begin{bmatrix} a_x \\ a_y \\ a_z \end{bmatrix} = \begin{bmatrix} \dot{v} \\ \frac{\dot{s}}{\rho}\cos(\beta)V + \dot{\chi}V \\ -\frac{\dot{s}}{\rho}\cos(\chi)\sin(\beta)V + \dot{\beta}\sin(\chi)V \end{bmatrix} \tag{A.10} $$

This equation tells a lot about how the optimisation works. The direction of turn is determined by β. Consider a 2D road. Since $\boldsymbol{n}$ always point to the right side (from the perspective of the cyclist) according to our definition, β determines if the principal curvature is to the right, yielding $\cos(\beta) = 1$, or to the left, yielding $\cos(\beta) = -1$. Since all the other variables are per definition positive, β indicates the turn direction.

What is also clearly represented, is that a_z consists of two kinds of acceleration. The first one describes the centrifugal acceleration that is experienced when the elevation is not constant. This acceleration is greatest when β has the values 0.5π and 1.5π, indicating that the principal curvature points in or out of the road plane. That situation is like driving over a top of a hill or down through a valley. The second kind of acceleration is experienced when β changes, and the cyclist has an orientation different from the tangent direction of the curve. The largest effect occurs when the cyclist would ride sideways on the road, while β is changing a lot. When you ride sideways, and the banking angle or principal curvature direction (or both) suddenly changes, it can feel like you ride down or up a slope suddenly. This effect mostly has a small influence, due to the fact that χ will remain small and $\dot{\beta}$ as well when considering existing roads. Roads are designed such that they are smooth and the driver does not need to perform extreme steering actions.

B

Velocity projected on the center line

In this thesis, the velocity projected on the center line is simplified. To explain why this was done and what the implications are, first the idea and theory behind this projected velocity, $\dot{s}$, is explained.

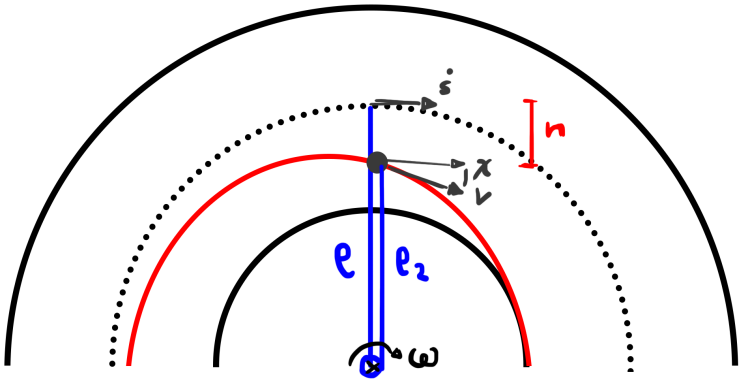

Figure B.1: A flat road with a turn, seen from above. The red trajectory is the trajectory of the point mass. The dotted line represents the center line.

We will start from the most simple situations. A point mass is moving in the turn of a flat road. It is cutting the corner by moving at the inside of the turn (see figure B.1). The projected speed is calculated with help of the notion of angular velocity. The idea is that the angular velocity of a projection of the point mass on the center line is the same as the angular velocity of the point mass, when it is moving in the same direction as the tangent direction of the center line. The angular velocity of the projection on the center line can be described by $\frac{\dot{s}}{\rho}$. The angular velocity of the point mass moving in the same direction as the center line can be described by $\frac{\cos(\chi)v}{\rho_2}$. ρ_2 can actually be written in terms of ρ, as it is equal to $\rho - n$. The angular velocities are per definition equal to each other, giving the following expression:

$$\frac{cos(\chi)v}{\rho - n} = \frac{\dot{s}}{\rho} \tag{B.1}$$

This can be solved for the projected velocity:

$$\dot{s} = \frac{\cos(\chi)v}{1 - n\kappa} \tag{B.2}$$

Now an expression for the projected velocity has been found. The nominator describes the projection of the velocity on the center line tangent. The denominator describes the cutting of corners; if n and κ have the same sign, the corner is cut

and the speed is scaled accordingly. The found expression however is fit for the condition of a flat road. For a 3D road, an expansion must be made.
This addition can be explained best through a situational figure (see figure B.2).

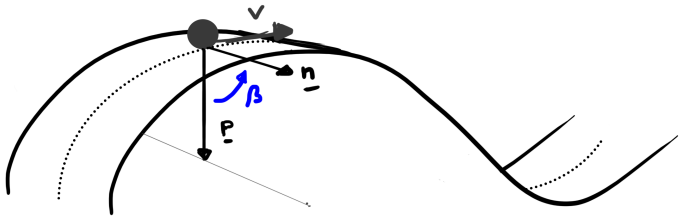

Figure B.2: A straight road which curves over a hill. In this situation, the principle curvature vector and the camber vector are perpendicular. A lateral shift of the point mass does not affect the radius of curvature.

In this situation, the lateral positioning does not result in cutting corners. This means that the denominator term of $\dot{s}$ should not be reducing the radius. this is accomplished through the introduction of an extra term:

$$\dot{s} = \frac{\cos(\chi)\, v}{1 - n\kappa\cos(\beta)} \tag{B.3}$$

In the particular situation from figure B.2, β equals 0.5π. This means that the term $\cos(\beta)$ is reduced to zero. The radius is not cut by the lateral positioning anymore. This expression for $\dot{s}$ is used in this thesis. However, the expression was build up using the velocity of a point mass on the ribbon plane that has no height or roll effects. The attribute of height together with roll can also influence the radius, so for an accurate calculation of the projected speed their effect should be included.

First, an expression for $\dot{s}$ will be discussed that includes height and roll. Then it will be explained why that expression was not used in this thesis. So how can roll influence the projected speed? Let's start with a simple situation. A cyclist is cycling on a flat road, that has a turn in it. This is illustrated in figure B.4. If the cyclist is positioned upright, without any roll, the distance from the CoM to the center of the osculating circle is the same as that from a location on the ground, between the wheels. When the cyclist starts to roll to the inside of the turn, the CoM gets closer to the center of the osculating circle. If the velocity is the same, but the radius is smaller, this means that the projected speed is relatively larger now (see equation B.1). Another example in which the CoM height can affect the projected speed is again the situation of figure B.2. Here, the height of the CoM adds up to the radius of curvature of the center line. A new expression for $\dot{s}$ that takes roll into account is presented in equation B.4.

$$\dot{s} = \frac{\cos(\chi)\, v}{1 - n\kappa\cos(\beta) - h\kappa\cos(\chi)\sin(\beta+\phi)} \tag{B.4}$$

The denominator has an extra term compared to the previous variant. This term compensates for the change in radius due to roll. An example for the compensation can be found in figure B.3.

The expression for $\dot{s}$ includes the roll angle, which is not a geometry variables nor an OCP variable. As the roll angle results from the lateral acceleration combined with the local road geometry, many more equations are necessary to find its value. Another option is to create a 6D database of values of ϕ, and interpolating it. Both of these options are computationally expensive. Next to that, the errors created by using expression B.3 for $\dot{s}$ are small. This can be explained while looking at a sharp turn (see figure B.4). For this example the measurements of the sharp turn in segment 6 of the L218 are taken. When a cyclist makes the turn here at a high speed, the roll angle is large. This means that the effective radius of curvature, from the center of the osculating circle to the CoM, differs with $h\sin(\phi)$ from the radius of curvature from the origin of the bicycle frame. Considering a maximum roll angle of 28.5 degrees, and a CoM height of 1 m, the maximum distance change is about 0.5 m. In segment 6, the maximized turn radius is about 20 m. Subtracting 0.5 m gives a maximum turning speed of 11.97 m/s, compared to 12.12 m/s when looking at the turn radius of the origin of the bicycle frame. The difference is only 1.3 % of the speed. The largest possible difference in curvature radius is the full height of the CoM. A situation in which this could happen is when the axis of rotation is parallel with the lateral bicycle direction, which can happen in a Velodrome. When the roll angle is zero, the radius is altered with distance h. With a a difference of 2.6% of the minimum speed, it can be concluded that (certainly when the error is small with respect to the road data uncertainty) the difference between the two speeds is negligible. This was also the conclusion of the authors of several bicycle and motorcycle studies [7, 24, 48]. Therefore, expression B.3 was used for $\dot{s}$ in this thesis.

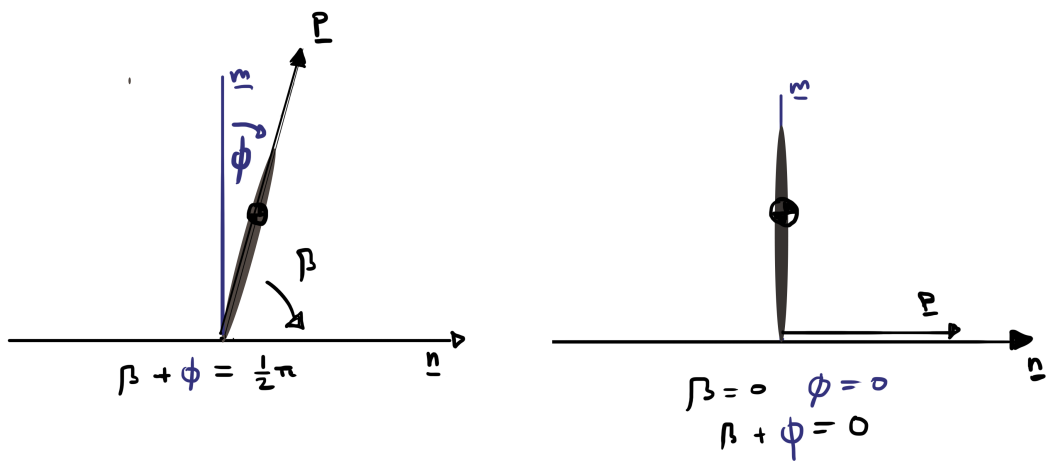

Figure B.3: In this figure, two example situations are reviewed. The cyclist is visible from behind. In the first situation, the cyclists roll direction is the same as that of the principal curvature. This causes the third part of the denominator expression to have maximum influence, as $\sin(0.5\pi)$ equals one. The expression then becomes $h\kappa\cos(\chi)$, which stands for the length with which the effective radius of curvature is reduced due to the full CoM height. In the second example, the direction of roll and the principle curvature vector are perpendicular. This means that the effective radius of curvature as seen from the wheel contact point is the same as from the CoM. The third part of the denominator expression now equals zero.

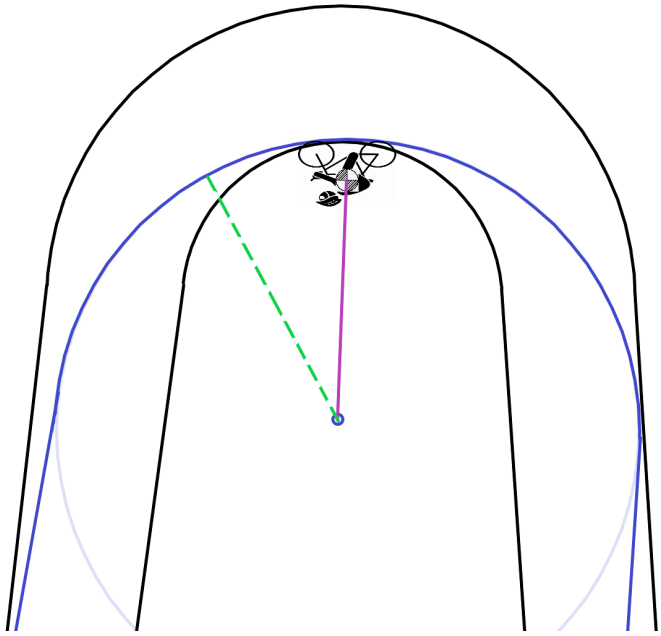

Figure B.4: Simplified turn in segment 6. The maximum turning radius is almost equal to the outer road boundary turn radius. The CoM of the rolled bicycle + cyclist reduces this radius of curvature.

C

G-G diagram solving approach

A normal approach for finding the g-g diagram is to first find the acceleration limits at $a_x = 0$ and $a_y = 0$, as it is easy to guess to results at those orientations [28, 48]. Then the orientation is changed slightly. To find the acceleration limits for the new orientation, the results from the previous orientation are used as initial guesses. With this method, the entire g-g diagram for a certain location on the road, a specific speed and a certain χ can be created. A final constraint for the model is necessary to make sure that the optimisation finds a solution (a maximized adherence radius) for a specified adherence orientation α.

$$a_x - a_y \tan(\alpha) = 0 \tag{C.1}$$

For a 2D situation with only 2 variables, the created data is then merged into a biquintic spline, which is smooth and fast to interpolate. However, there are many more input variables to the problem for this model compared to a 2D road model. The g-g diagram solution will have more dimensions than smooth splines can be created for with functions available at this moment.

C.1. solving for a g-g diagram with more than 2 variables

Therefore, a function was written that directly calculates the acceleration limit when given input variables $\{\alpha, v, \psi, \gamma, \beta, \dot{\beta}, \rho, n, \chi\}$, without starting from known values at a_x and a_y. To still provide somewhat accurate initial values for the optimisation variables, the orientation angles are sorted into a category, and receive the initial values for a known orientation (as shown in figure C.1).

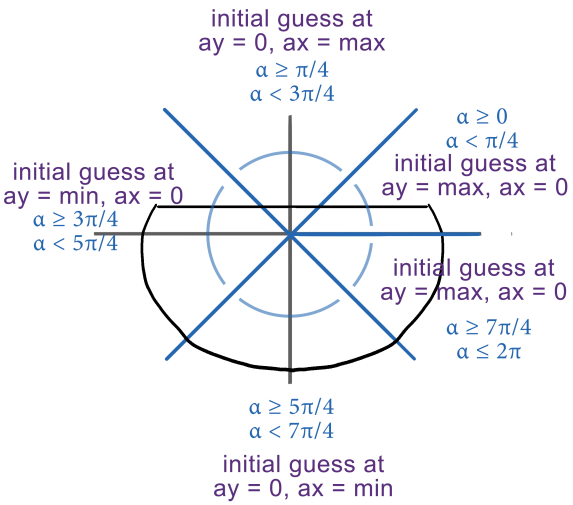

Figure C.1: An orientation is sorted into an area to provide the initial values from the nearest angle of which the initial values are known.

Testing has shown that when near enough to somewhat accurate initial guesses, the correct acceleration limits are found.

While the results are accurate, a downside of this approach is that it is slow, as an optimisation is run within an optimisation.

Another option is to create a multidimensional database that can be interpolated with the *interpn* MATLAB function. A linear interpolated is mostly not good enough to enable convergence. A cubic interpolation is fast and provides a much smoother function, to help convergence. This approach is less accurate but fast.

C.2. difficulties of g-g diagrams for 3D motion

Adding elevation and banking to a road brings along some computational differences. For example due to a steep elevation, the forward acceleration limit can drop below zero. This means that the g-g diagram does not surround the origin anymore. That is a problem, as a single adherence orientation can now have either zero or multiple maximum adherence radii r_{max} as a solution. To solve this, the solution is shifted so that the g-g diagram is expected to surround the origin again. The moves are based on three generalised effects that can be found:

1. the g-g diagram moves horizontally when γ changes.
2. the g-g diagram moves vertically when ψ changes.
3. the g-g diagram moves vertically when v changes, due to the higher aerodynamic drag.

Another effect that can be found is that β effects the surface size of the g-g diagram (expansion and reduction), but this does not influence the placement of the origin within the diagram.
So how much does the g-g diagram move when those effects happen? This can be predicted largely when looking at the orientation of the gravitational force. For example the forward acceleration a_x is influenced by the elevation orientation of the road. When χ is very small, this can be simplified to equation C.2

$$ma_x + mg\sin(\psi) = F_{xr} + F_{xf} - F_d \tag{C.2}$$

It is clear that the acceleration changes longitudinally with $mg\sin(\psi)$, and the g-g diagram is moved up or down with respect to a g-g diagram of a flat surface. To make sure that the origin is still located within the g-g diagram, the g-g diagram is moved. This is done through subtracting the generalised effects (not the exact effects) from a_x and a_y in the equations of steady motion that are used in the *fmincon* constraints. This looks like equation C.3.

$$a_{xnew} = a_x - F_d/m + g\sin(\psi), a_{ynew} = a_y - g\sin(\gamma) \tag{C.3}$$

It does not matter that the displacement caused by the elevation is not always completely undone, as long as the shifting is done consistently. But how is the shifted g-g diagram still useful when it does not have the correct values for r_{max}? The answer is to make sure that the inputs that are used in the control optimisation are treated in the same way. The values of a_x and a_y are moved as well, in an opposite manner to the one shown in equation C.3 (signs change). This is illustrated in figure C.2.

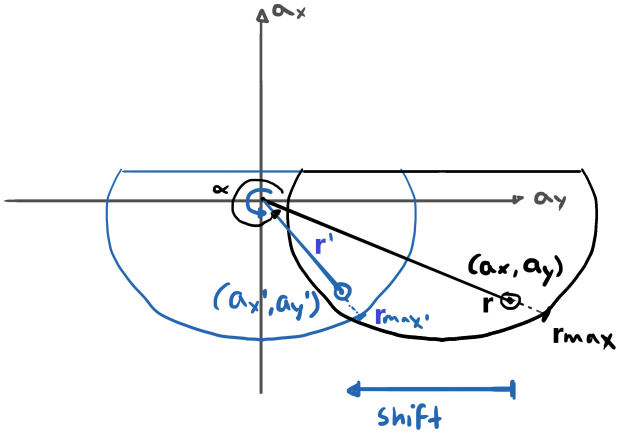

Figure C.2: An example of a shifted g-g diagram. Both r and r_{max}, as well as α are calculated taking into account the shift, so that they are still comparable. FIXME

D

Convexity and continuity of the g-g diagram

The feasible input region of the minimum-time optimisation for a certain combination of speed and local road geometry is described by a g-g diagram. A g-g diagram as an optimisation constraint only works if the g-g diagram is continuous, and preferably smooth. What also helps the convergence, is a convex g-g diagram. In a convex shape, all lines of which the endpoints lie within the shape lie fully within the shape. In other words: it is impossible to draw lines that start in the shape, leave it, and end within the shape again. A convex constraint indicates that any local minimum is a global minimum as well. In this appendix it will be discussed whether a g-g diagram is always continuous and convex.

The g-g diagram model described in this thesis is based on a friction ellipse. Under perfect conditions, the acceleration limits would look like the friction ellipse, which is a continuous and convex shape. Under imperfect conditions, acceleration limits 'cut' the ellipse in a different shape, that lies within the ellipse. When looking at those 'cutting' shapes, there are several that can be named. The easiest is the maximum power condition, that just cuts off the upper part of the ellipse in a straight line. The remaining shape is still convex. But when looking at the stoppie limit, this can cause an elliptic cut from the bottom of the diagram. Then, the shape is not convex anymore, but it is continuous. While the stoppie limit can make the shape of the g-g diagram convex, it is unlikely to cause much problems with finding global minima. This is because the stoppie limit shape is symmetric about the longitudinal axis: both sides of the axis stand for different cycling directions. It is not often the case that riding to the left and riding to the right are (almost) equally effective options to reduce the cost function. Therefore, the stoppie limit will not cause many convergence problems. Receiving a discontinuous shape would only happen when some boundary condition or constraint is active for a certain angle set only. Such conditions do not apply in this model. Therefore, it can be concluded that a g-g diagram set up in the way described in this thesis is sometimes non-convex (only when the stoppie limit is in play, while driving downward) and always continuous.

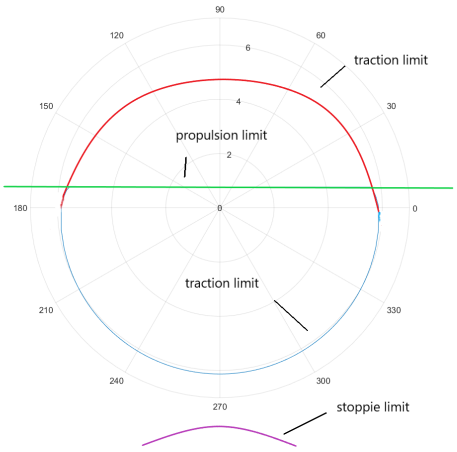

Figure D.1: Example of a g-g diagram. The stoppie limit can cut the lower part from the diagram in certain conditions, creating a non-convex shape. In this figure, the stoppie limit is not of influence.

E

Bicycle and rider parameters

Table E.1: Bicycle and rider parameters as used to create the database for the L218

symbol	description	value	
b	longitudinal distance of the center of mass to the rear wheel, in $\{F\}$ frame	0.4469	m
h	vertical height of the center of mass, in $\{F\}$ frame	1.00	m
w	wheelbase	0.993	m
m	mass of the bicycle + cyclist	80	kg
CdA	drag area coefficient	0.32	m^2
g	gravity	9.81	m/s^2
δ	air density	1.20	kg/m^3
P_{max}	maximum power available (often critical power)	0	W
μ_x	longitudinal friction coefficient	0.75	-
μ_y	lateral friction coefficient	0.75	-

motivation
The center of mass was estimated to be positioned just above the front of the saddle. The height of the upper side of the saddle was estimated at 1 meter [41]. As a rule of thumb, 45% of the rider weight is estimated to be distributed to the front wheel, in upright position on a flat surface [18]. This means that b consists of 45% of the wheelbase. The wheelbase size was taken from the Ultimate CF SL Disc 8.0 Di2 Canyon bike. The mass of the bicycle plus the cyclist is an estimate, where the bike makes up a minimum of 6.8 kg (UCI regulations). The weight of Tour de France cyclists is often around 70 kg [13]. Together this was rounded to 80 kg. The drag area coefficient was chosen to represent relatively optimised aerodynamics [46]. Air density was taken for 20° C and IUPAC standard pressure. The maximum power was set to zero, as in the comparison study ([51]) only coasting (no pedalling) is allowed. The friction coefficients are for a bicycle on a dry asphalt road [68].

F

Finding the global optimum

Having non-convex constraints makes it hard to verify if the found local optimum is also the global optimum. To try and check this, the minimum-time optimisation was run several times with different guesses for the state variables and input variables. The runs and found solutions of the runs are discussed in this appendix.

The run strategy that was used to find the results presented in chapter 5 uses a mock-up function first to quickly find a good guess of the results. This was then used to find the final results. To test if a global optimum was found, optimisations were run directly with the correct constraints. Because this is a very sensitive function, a slightly different setting was used in IPOPT to help prevent the optimisation to get stuck in the restoration phase. Specifically, the hessian approximation was set to "limited-memory" instead of the "exact" setting. The guess works in the following way: variable guesses are made for the start and end point of the track. The nodes that lie in between them receive a guess based on linear interpolation. Various tests have been run to confirm whether an optimal solution was found. The different guesses used will be discussed, then the output trajectories and velocity profiles will be compared.

F.1. overview of the initial guesses

The first run that was tested features the same initial guess as was used to run the mock-up model with. Now, it is run directly with the database, to see if the solution direction of the mock-up model and the database give the same results.

variable	x_0	x_f
v	15 m/s	15 m/s
n	0 m	0 m
χ	0 rad	0 rad
a_x	0 m/s^2	0 m/s^2
a_y	0 m/s^2	0 m/s^2

Table F.1: Run 1. This initial guess was used to run the mock-up function as well.

The second run explores whether the model can still find the same solution when the guessed trajectory is majorly different. The trajectory was set to lie on the right side of the lane over the whole course of the track.

variable	x_0	x_f
v	18 m/s	18 m/s
n	3.3 m	3.3 m
χ	0 rad	0 rad
a_x	0 m/s^2	0 m/s^2
a_y	0 m/s^2	0 m/s^2

Table F.2: Run 2. In this initial guess, the trajectory guess is located at the right side of the lane at all times. The speed is constant.

For the third run, the trajectory was set to change from the left to the right side of the track slowly.

variable	x_0	x_f
v	5 m/s	18 m/s
n	-3.3 m	3.3 m
χ	0.2 rad	-0.2 rad
a_x	1 m/s^2	0 m/s^2
a_y	1 m/s^2	-1 m/s^2

Table F.3: Run 3. In this initial guess the trajectory goes slowly over the course of the track from the left side of the lane to the right side.

The fourth run guess is most equal to the found solution, as the end velocity is about equal and the initial acceleration is represented.

variable	x_0	x_f
v	5 m/s	20 m/s
n	0 m	0 m
χ	0 rad	0 rad
a_x	1 m/s^2	0 m/s^2
a_y	0 m/s^2	0 m/s^2

Table F.4: Initial guess that is much like the expected result.

For run 5, the velocity profile was radically changed. Instead of the expected velocity increase, a decrease was used as a guess.

variable	x_0	x_f
v	15 m/s	5 m/s
n	0 m	0 m
χ	0 rad	0 rad
a_x	-1 m/s^2	0 m/s^2
a_y	0 m/s^2	0 m/s^2

Table F.5: Initial guess where the cyclist starts at a high speed and slows down over time. The opposite of the expected velocity profile.

F.2. results

The figures (F.1 and F.2) show that a wide range of initial guesses (run 1,3, and 4) result into the same solution. Run 2 and 5 resulted in the same local minimum, although they had very different initial guesses. As a conclusion, to the best of our knowledge the solution that was used in the case study results is a global minimum.

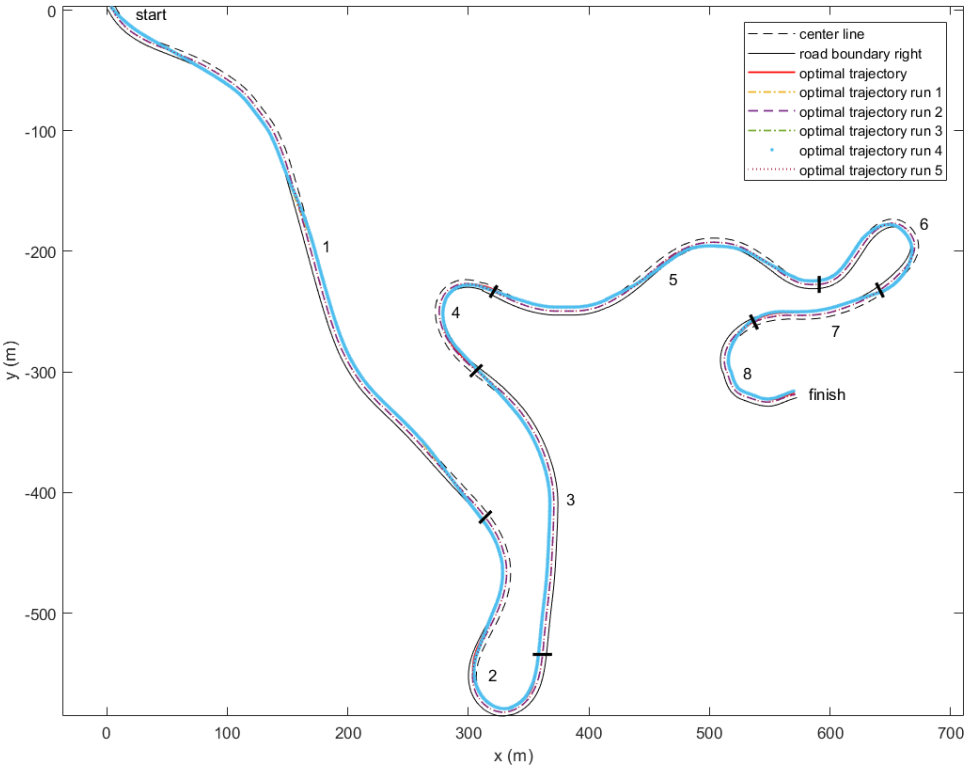

Figure F.1: The results show that the trajectories of run 2 and 5 remain around the center line, showing a local minimum solution. The other trajectories overlap, indicating that likely a global optimum was found.

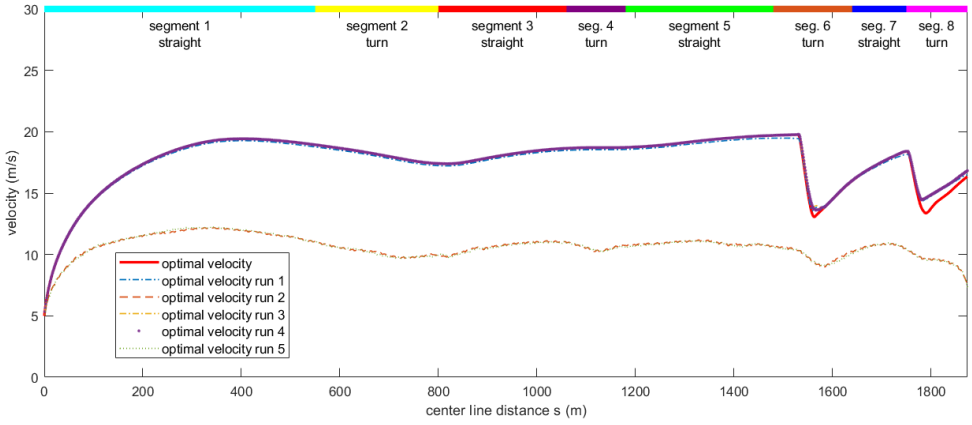

Figure F.2: The velocity profiles resulting from run 2 and run 5 differ and show a much much higher cost. The other results are about equal. The difference with optimal result found via the mock-up function might come from the fact that the optimal solution was not yet found for run 1,3 and 4. Their maximum amount of iterations was exceeded, the optimal solution was not yet reached.

G

Detailed results of the separate segments

G.0.1. segment 1

The separate segments will be discussed in more detail. The first segment of the descent is a long, relatively straight segment. The cyclists have a standing start, and race towards segment 2, which is a turn.

trajectory-
In figure G.1 the optimal trajectory can be seen, compared to the measured descents. Part of the GPS data is missing. Overall, the optimal trajectory corresponds well to the rider trajectory. There are several differences. The optimal trajectory is positioned to the furthest inside edge of the turns, while the cyclists do not go all the way to the side of the road. This can have several reasons. First of all, cyclists will always reserve some lateral space in order to be able to carry out control actions in case of unexpected perturbations. Furthermore, there is often sand and rubble at the side of the road. It can also be because the curvature is so small that they do not bother for the tiny time difference that this can possibly yield. Another notable difference is that the optimal trajectory crosses the road from right to left in a relatively short distance. Mathematically, the shortest distance to cross a straight road is when using the full distance to make the lateral position change. This is what the cyclists show too. As to why the solver might think that crossing more swiftly is better, this might have to do with the curvature determination from the track coordinates. If there is slightly more curvature determined than there actually is, it might be theoretically beneficial to move to the other side of the lane faster.

velocity profile-
The optimal velocity profile corresponds really well with the measured velocity profile (figure G.2). This indicates that the chosen power limit represents the experienced power limit well. The initial velocity of the optimisation is higher than the initial velocity of the cyclists (standing start). When taking this into account, the power limit might be slightly underrepresented for the start of the segment. Still, it is very close for an estimation based on noisy and incomplete power measurements.

g-g diagram-
The measurements show that this cyclist has braked during this segment (figure G.3). This is also seen in the velocity profile. There was no reason to break during this segment when solely considering the trajectory. However, the measurements were carried out on a road that was not closed off, allowing other road users to interfere with the descent. It is possible that a car interfered with this trial. This was reported for several trials. Since the data was anonymised, it is not certain if this happened during this trial. The rest of the g-g diagram overlaps and shows no divergent behaviour.

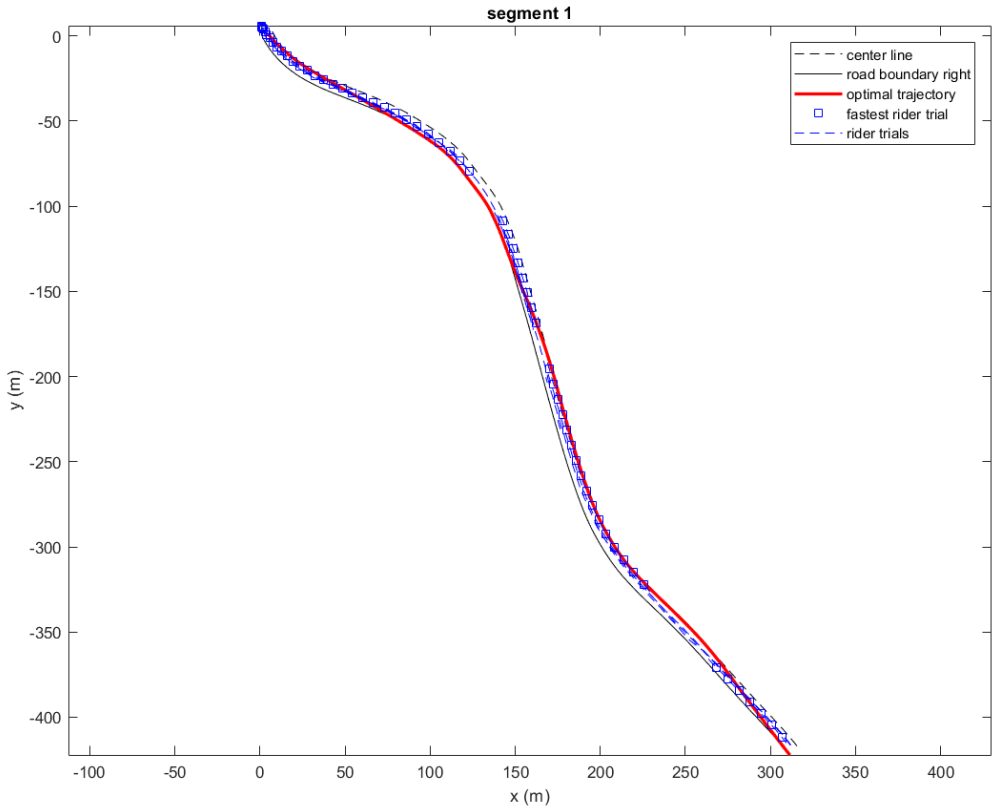

Figure G.1: The optimal trajectory compared to the measured trajectories in segment 1.

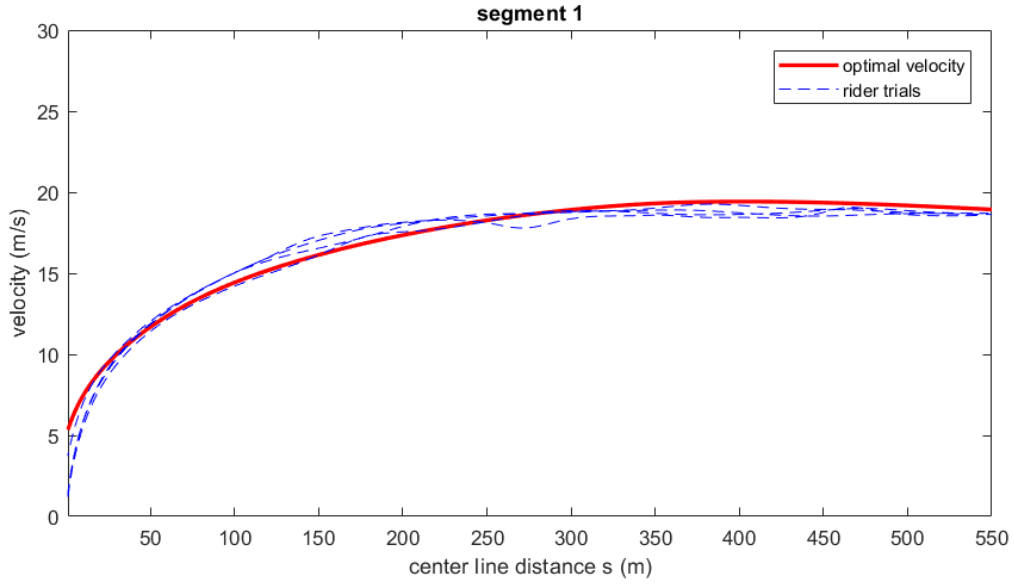

Figure G.2: Comparison of the optimal velocity to the measured velocities in segment 1.

G.0.2. segment 2

Segment 2 of the descent contains a left hairpin turn.

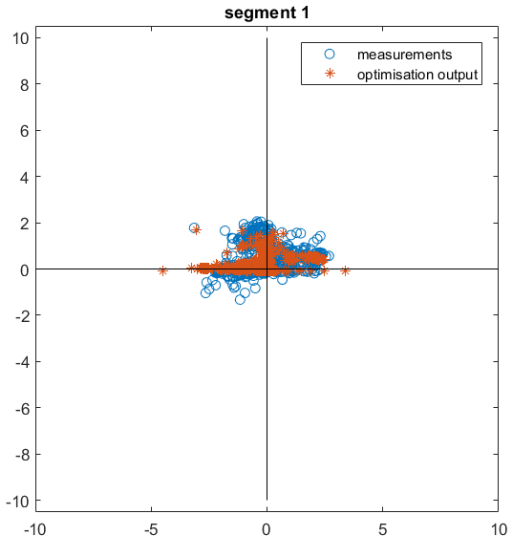

Figure G.3: The numerical g-g diagram compared to the optimal controls for segment 1.

trajectory-
The optimal trajectory has one remarkable difference from the measured trajectories: the turn is exited at the inside, instead of at the outside of the lane (figure G.4). This behaviour is not expected for such tight turns. For a tight turn, it is often efficient to ride in the largest possible turn radius, in order to maximize the cornering speed. This might indicate that the calculated curvature is incorrect.

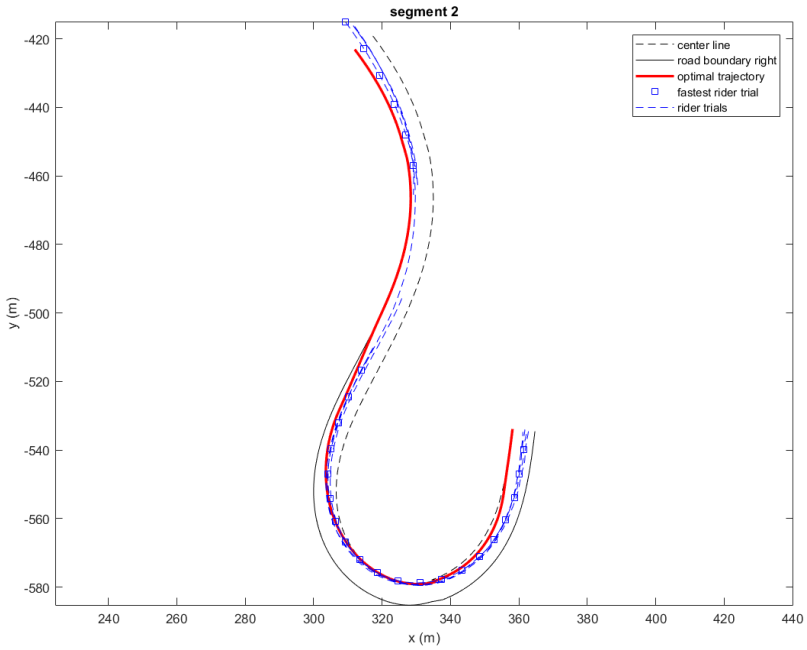

Figure G.4: The optimal trajectory compared to the measured trajectories in segment 2.

velocity profile-
When looking at the velocity profile (figure G.5), the same conclusion can be drawn as when looking at the trajectory; the calculated cornering speed is much higher than the cyclists dare to reach. While the cyclists will probably not reach the actual maximum possible cornering speed due their sense of risk, they will not be this far off.

g-g diagram-
This numerical g-g diagram shows totally different acceleration behaviour than the optimal solution (see figure G.3).

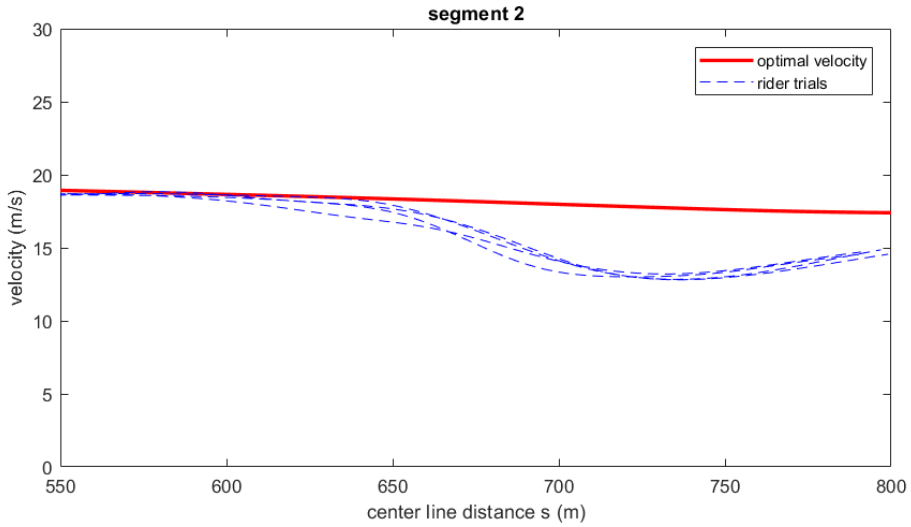

Figure G.5: Comparison of the optimal velocity to the measured velocities in segment 2.

The optimal cyclist does not brake in the segment. The measurements show braking during the right turn, the straight segment and the left turn. The only parallelism is found in the cornering; both plots show that turns happen. The optimal cyclist dares to act out a higher lateral acceleration, therefore less braking is needed. However, the difference in cornering speed is so high that this does not explain the complete behaviour. As mentioned before, the most likely explanation is that the curvature of this segment was too low.

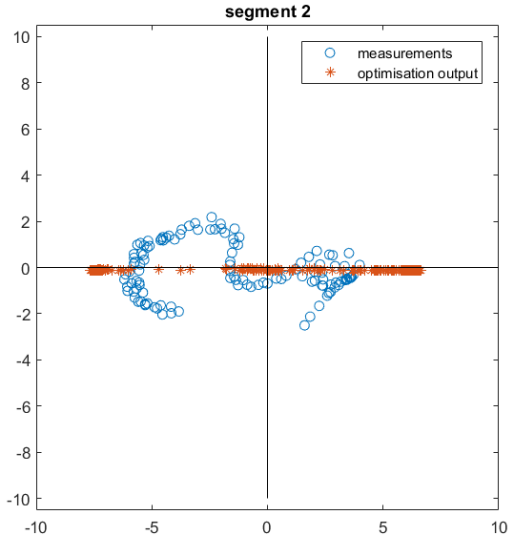

Figure G.6: The numerical g-g diagram compared to the optimal controls for segment 2.

G.0.3. segment 3

Segment 3 is a relatively straight segment, between two tight turns.

trajectory-
The start and end of the trajectory differ from the measured trajectories (see figure G.7). The start differs because in segment 2, the turn was exited at the inside instead of the outside. At the end of segment 3 lies another turn. The optimal strategy is to move to the inside of the turn much earlier than practised by the cyclists. In between the endpoints of the segment, the trajectory corresponds really well.

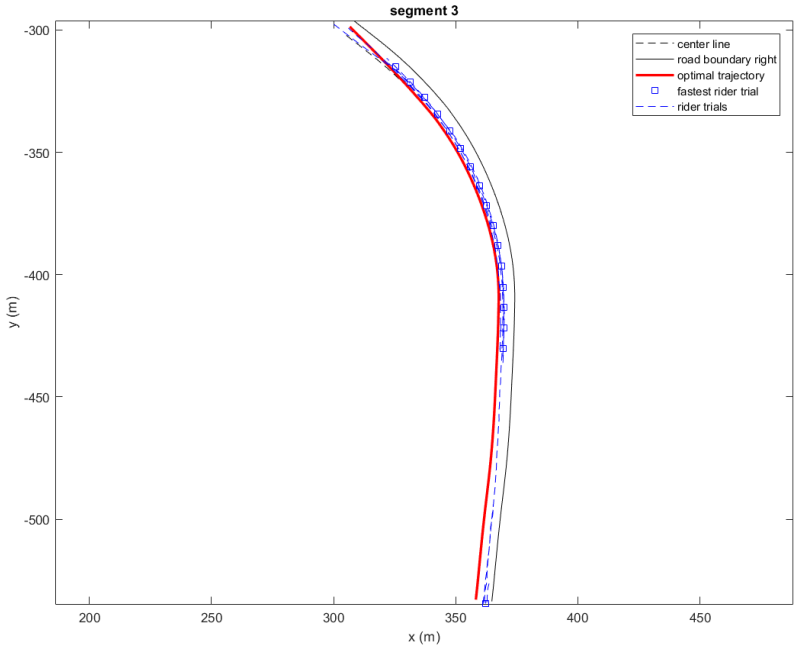

Figure G.7: The optimal trajectory compared to the measured trajectories in segment 3.

velocity profile-
The velocity profiles corresponds well (see figure G.8). The initial speed differs, because in the previous segment the optimal velocity was not reduced for the turn. The elite cyclists did reduce their speed in segment 2. Furthermore the cyclists start to brake at the end of segment 2, while this does not happen in the optimal velocity profile.

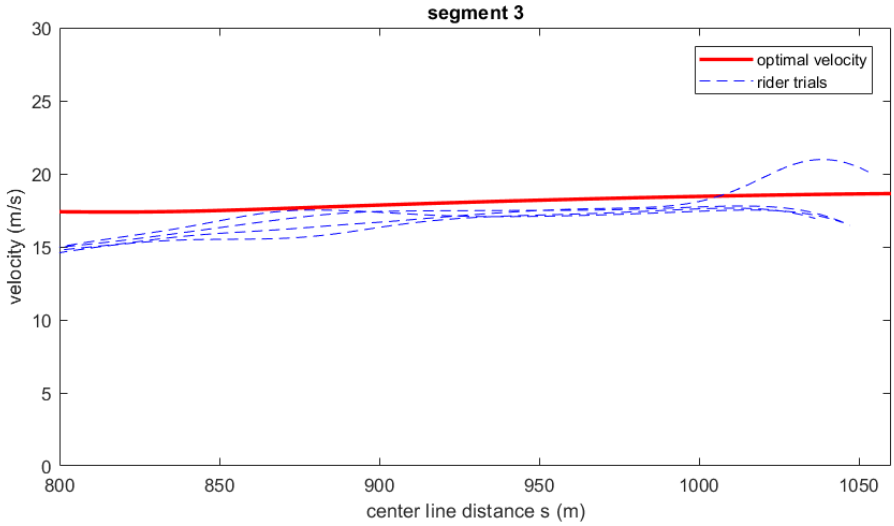

Figure G.8: Comparison of the optimal velocity to the measured velocities in segment 3.

g-g diagram-
This measured accelerations show a slight turn to the left, which is what happens in this part of the trajectory (see figure

G.9). However, they also show severe braking and acceleration. When looking at the velocity profiles, it it clear that the accelerations correspond with the profile where the rider accelerates and then brakes at the end of the segment. Still, the majority of the data points shows deceleration with about 2 m/s^2. This would mean that the cyclist is braking the majority of the time. This is not visible in the velocity plot however. This indicates a mismatch between the absolute velocity data (used for the velocity profile plot) and the directional velocity data that was used for the numerical g-g diagrams. This is probably due to the fact that the absolute velocity data was filtered.

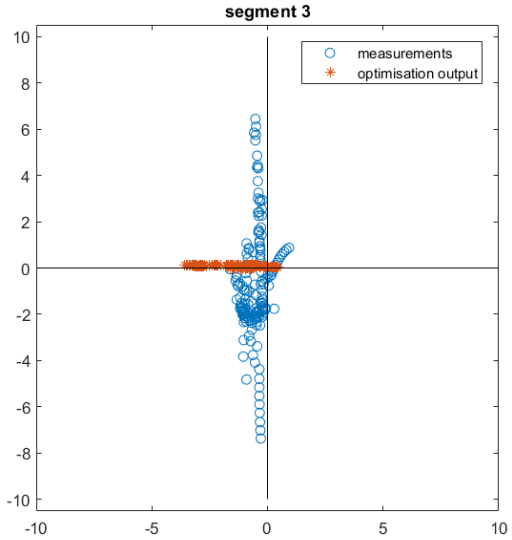

Figure G.9: The numerical g-g diagram compared to the optimal controls for segment 3.

G.0.4. segment 4

Segment 4 is a sharp tun to the right.

trajectory-

The optimal trajectory differs from the single GPS trajectory record that was not disturbed (figureG.10). The cyclist crossed the road center line, to the right (forbidden) half. While this is not allowed in this optimisation, one still would expect the trajectory to have a maximized turn radius. This is not the case. This can very well be another case that proves the difficulty curvature determination. This is hard to do, since it is based on the second derivative of the road coordinates. The noise of the GPS coordinates is amplified by taken the second derivative, resulting in very noisy curvature values.

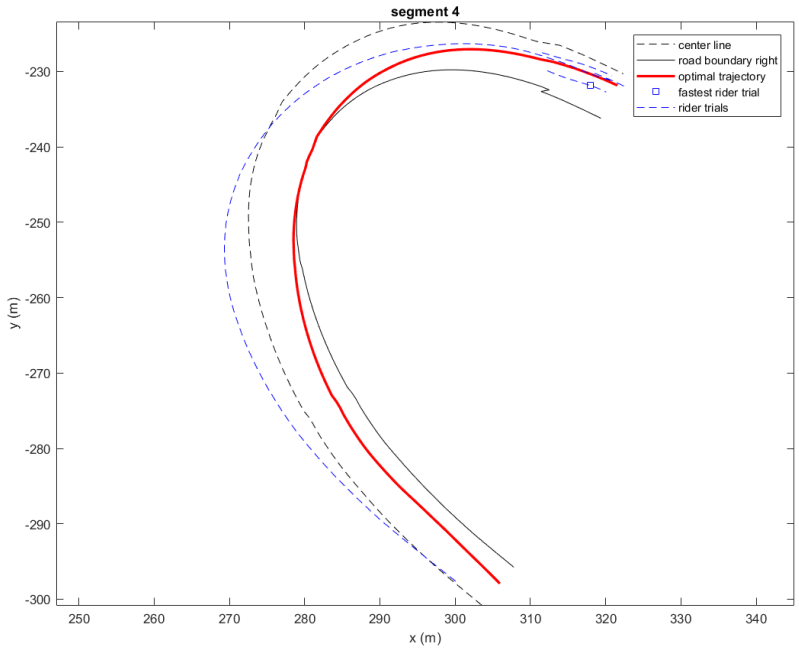

Figure G.10: The optimal trajectory compared to the measured trajectories in segment 4.

velocity profile-

The velocity profiles do not look alike at all (see figure G.11). As mentioned before, the large accelerations are not humanly possible. It is therefore certain that measurement or filtering errors were made. The IMU data in this specific corner was non-existent or of very bad quality for many of the trials. A more expected outcome would be that the riders break into the corner and then accelerate well into the next segment.

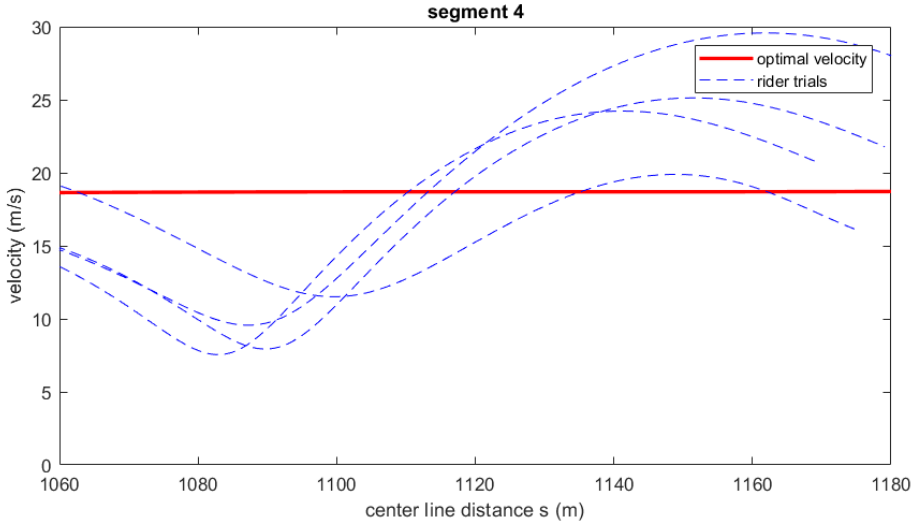

Figure G.11: Comparison of the optimal velocity to the measured velocities in segment 4.

g-g diagram-

From this g-g diagram it is clear that there are two things going wrong (see figure G.12). Firstly, the measurement data.

Those acceleration values are impossible to reach on a bicycle, so something in the measurement or filtering process has gone wrong. This could well be the translation of the accelerations from the IMU directional axes to the inertial x and y axes. However, this is unclear and unsolvable without the raw data. The second striking notion is that the solution of the optimal control problem does not include braking in this segment, while the cyclist is riding a speed higher than the maximum cornering speed (when making a rough estimate of the radius of curvature). This indicates that either the solution is incorrect, or the curvature fed to the OCP is incorrect. Since the author has experimented with various road geometries and the found maximum cornering speed was correct every time, the latter is strongly considered.

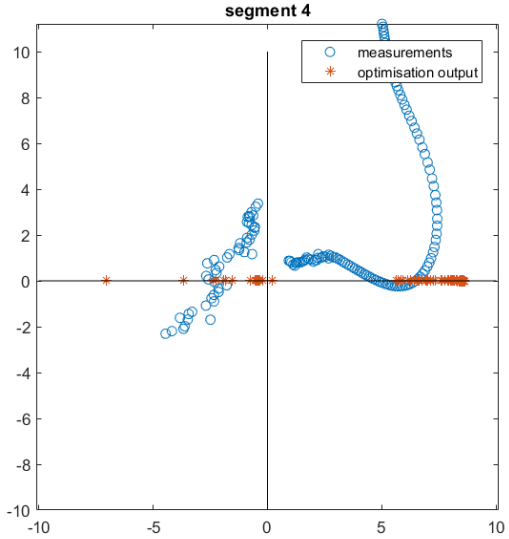

Figure G.12: The numerical g-g diagram compared to the optimal controls for segment 4.

G.0.5. segment 5

Segment 5 is a relatively straight segment. After this segment a sharp hairpin turn is situated.

trajectory-
The optimal trajectory and the measured trajectories correspond well (see figure G.13). The main difference is that the optimal trajectory touches the outside of the road more closely. At the center line of the road this difference is not seen. This indicates that the side of the road may be of bad quality, preventing the cyclists to ride on it. The left boundary of their lane is the center of the road, which is probably in a better shape.

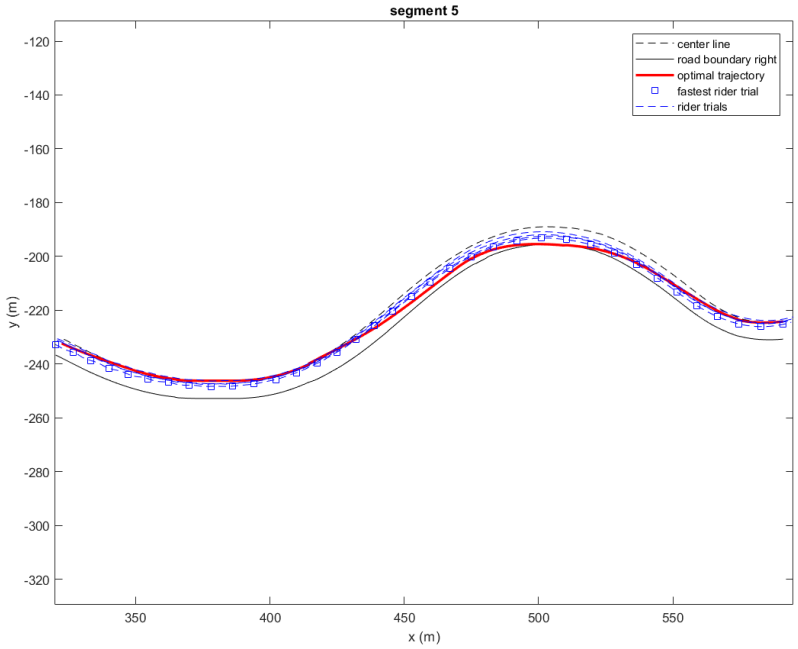

Figure G.13: The optimal trajectory compared to the measured trajectories in segment 5.

velocity profile-
The main differences in the velocity profile lie at the beginning and the end of the segment (see figure G.14). At the start of the segment, the odd speeds of segment 4 still have their effect. At the end of the segment, the cyclists already slightly decelerate before they enter segment 6. Segment 6 contains a sharp turn. It is more efficient to spend as little time as possible on braking. Braking hard and short will leave more time for acceleration. Therefore, no deceleration is seen yet in the optimal velocity profile.

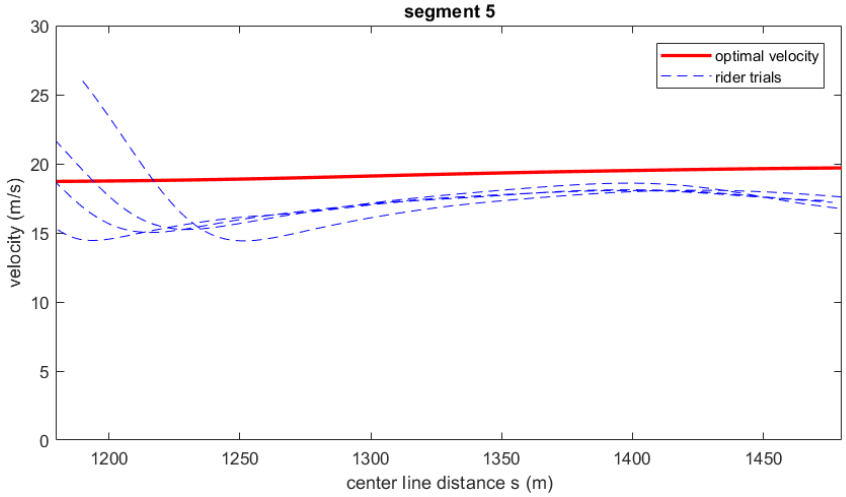

Figure G.14: Comparison of the optimal velocity to the measured velocities in segment 5.

g-g diagram-
Overall the g-g diagrams show much correspondence (see figure G.15). The measurements show severe braking, this is probably still a part of the extreme accelerations shown in segment 4. The cyclist can deliver a bit more acceleration than the optimal controls, since its speed is lower over the whole segment (less air drag). The cyclist also brakes at the end of the segment. This is a preparation for segment 6, a very tight turn. This is not optimal, as (according to the Pontryagin Maximum principle) it is better to control with short, extreme control actions.

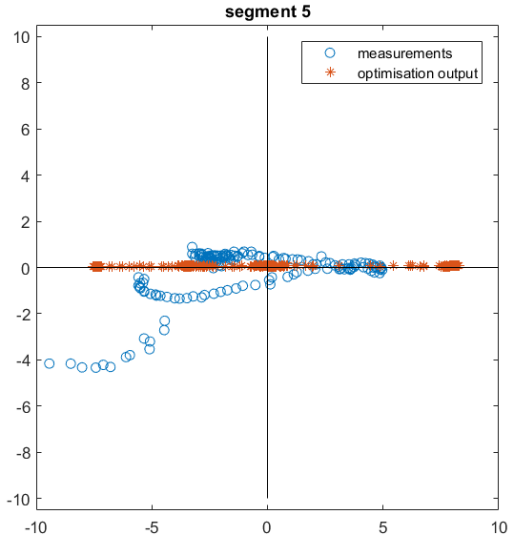

Figure G.15: The numerical g-g diagram compared to the optimal controls for segment 5.

G.0.6. segment 6

Segment 6 is the sharpest turn of the descent. The center of the right lane has a radius of curvature of about 20 meters.

trajectory-

The trajectory of the cyclists differs somewhat (see figure G.16). Steering into the corner happens earlier, and the path of the exit is more wide. The first aspect saves distance, and the second enlarges the turn radius of the cyclist, allowing a larger cornering speed.

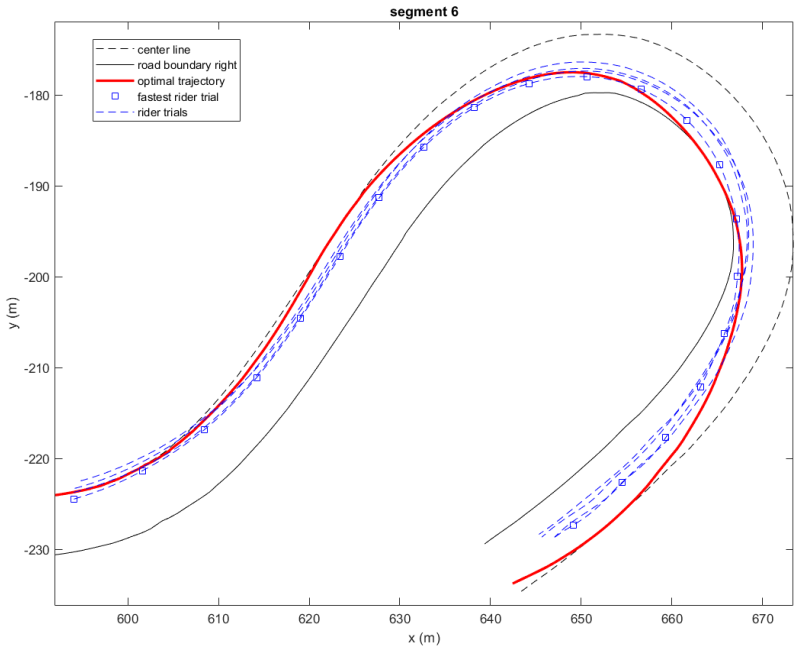

Figure G.16: The optimal trajectory compared to the measured trajectories in segment 6.

velocity profile-

The velocity profile differs in three aspects (figure G.17). (1) The speed at the start of the segment is higher. (2) The braking happens in a shorter period of time. (3) The cornering speed is the same, but the optimal minimum speed is reached earlier than that of the cyclists. As for (1), this is a result of some light braking that happens at the end of segment 5. This is not a result of the gradient. As explained earlier, (2) is efficient and optimal. The optimal deceleration can be higher than that carried out by the cyclists. The optimal cyclist knows no fear, and makes use of optimal braking to take fully advantage of the force capacity of the tires.

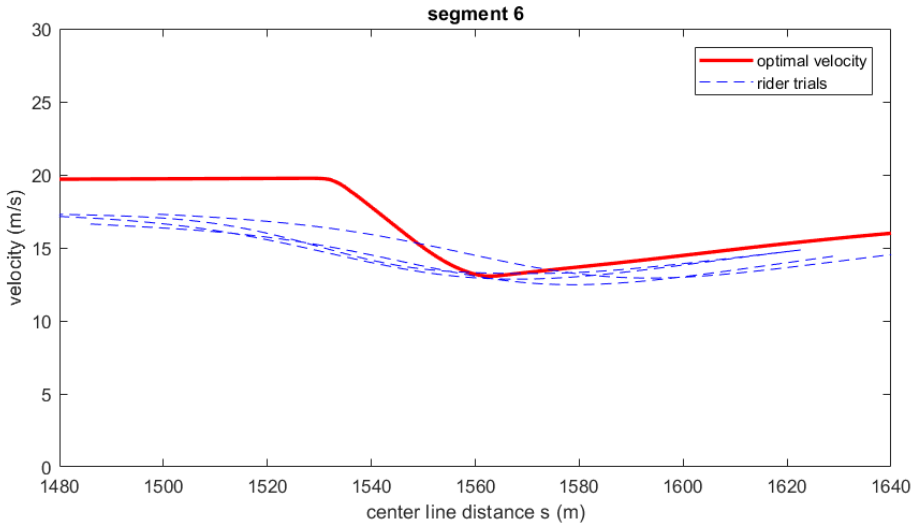

Figure G.17: Comparison of the optimal velocity to the measured velocities in segment 6.

g-g diagram-
This numeric g-g diagram shows beautifully how the accelerations succeed each other (figure G.18). This also shows that the rate of change of the accelerations (jerk) is constrained. This is an important difference between the optimal control solution and practice; in practise it is not possible to make a sudden lateral switch in accelerations due to transient dynamics while in the model steady motion is assumed. Next to this the main differences between the measured and optimal accelerations are the magnitudes. The optimal controls show higher decelerations and lateral accelerations than the cyclists dare to perform.

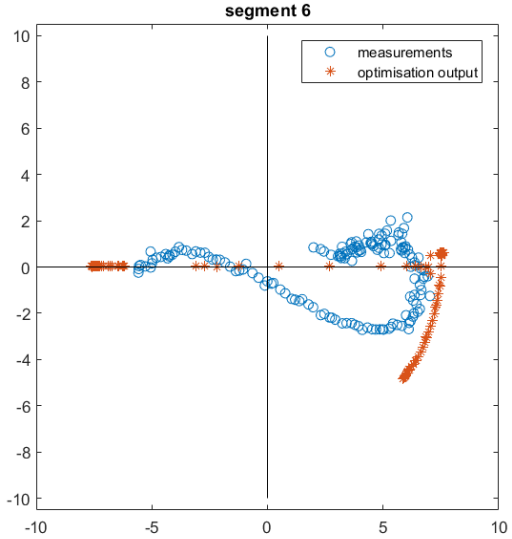

Figure G.18: The numerical g-g diagram compared to the optimal controls for segment 6.

G.0.7. segment 7

Segment 7 is a relatively straight segment.

trajectory-

The main trajectory corresponds (see figure G.19). The differences are once again found at the start and end of the segment. The optimal trajectory has a wider exit from segment 6, explaining the difference at the start. At the end of the segment, the optimal trajectory takes a bit longer to transition towards the inside of the turn. While trajectory of the cyclists might be shorter, the optimal trajectory enlarges the radius of curvature, to ensure maximum possible cornering speed.

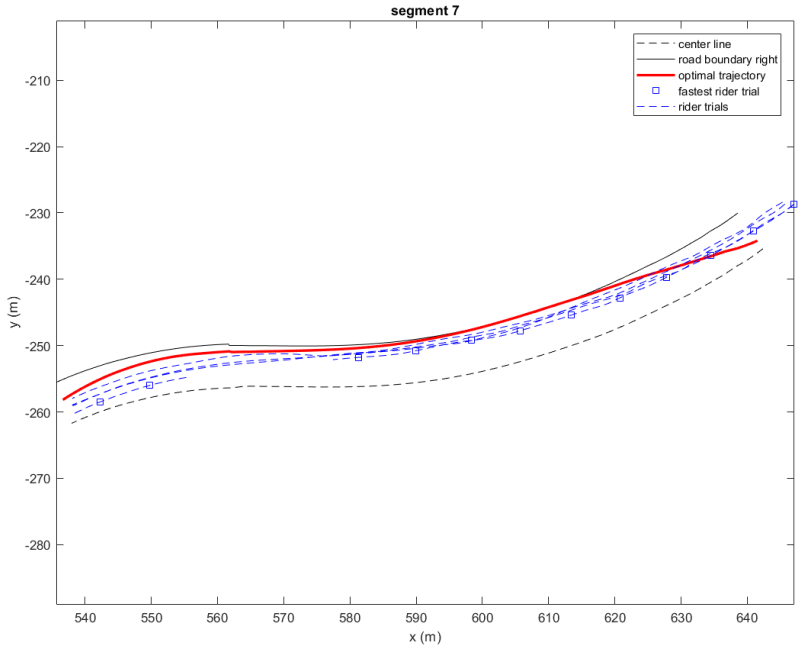

Figure G.19: The optimal trajectory compared to the measured trajectories in segment 7.

velocity profile-

The velocity profiles match (see figure G.20). At the second part of the segment, the elite cyclists seem to brake slightly while the optimal velocity keeps increasing.

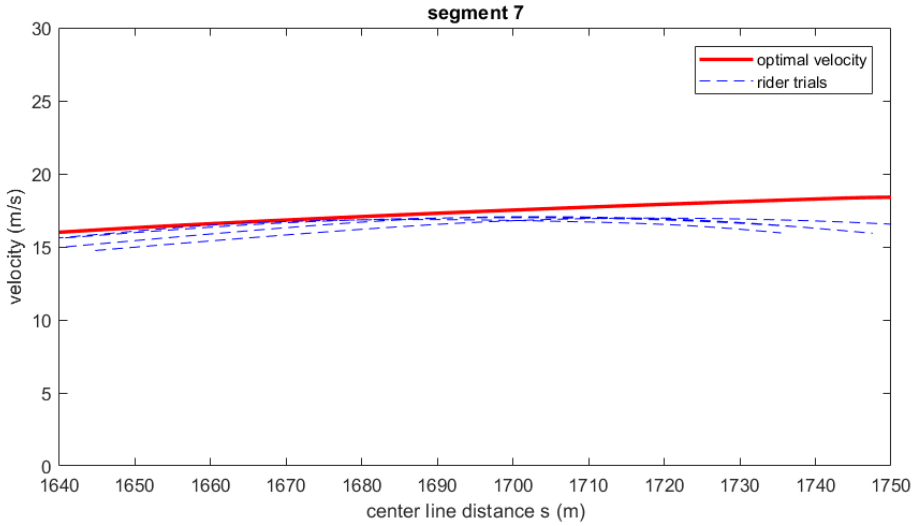

Figure G.20: Comparison of the optimal velocity to the measured velocities in segment 7.

g-g diagram-

First of all, some of the measured accelerations are again higher than they can be (figure G.21). This points towards a measurement error that has been filtered out for the velocity calculations, as such high accelerations are not seen in the velocity plot. Furthermore, the optimal solution shows much higher lateral accelerations. It is questionable whether such high accelerations are necessary, as the optimal trajectory is almost straight. At the end of the segment the turn to the left should require some lateral acceleration, but it is unclear why such high lateral acceleration towards the right should be necessary. This points towards an inaccuracy in the curvature data once more.

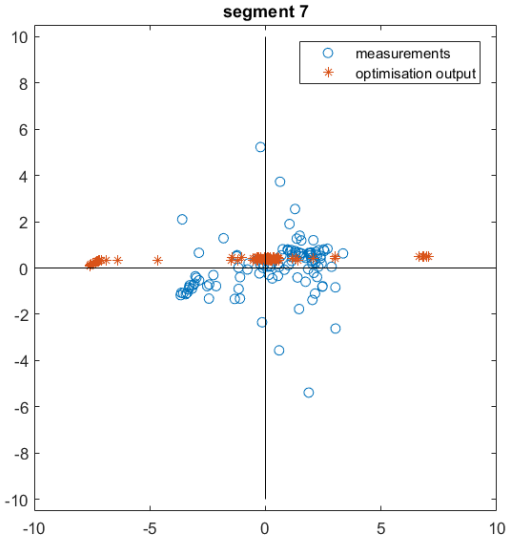

Figure G.21: The numerical g-g diagram compared to the optimal controls for segment 7.

G.0.8. segment 8

Segment 8 is a somewhat larger turn. The end of the segment is the finish line for the experimental trials.

trajectory-

The trajectory is, like those of the cyclists, situated at the inside of the turn (see figure G.22). The optimal trajectory looks strange and wobbly. This is because of the shape of the center line. Those smaller curvatures have been filtered out of the curvature data, while the raw center line data was used to plot the road. When lateral distance n stays constant but the center line is wobbly, the trajectory is wobbly is well. Were the minor curvatures taken into account, then the trajectory would have been more fluent regardless of the center line shape.

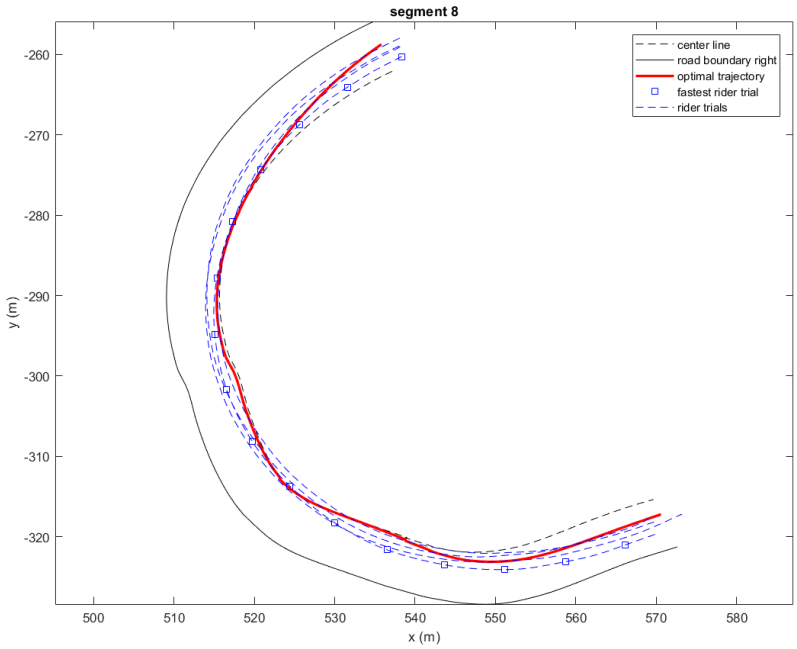

Figure G.22: The optimal trajectory compared to the measured trajectories for the final segment.

velocity profile-

Once again the optimal velocity profile shows that braking shorter and harder is more efficient (see figure G.23). This time however, the minimum velocity that is reached is lower than that of the cyclists. This indicates that the calculated curvature might be higher than the real curvature.

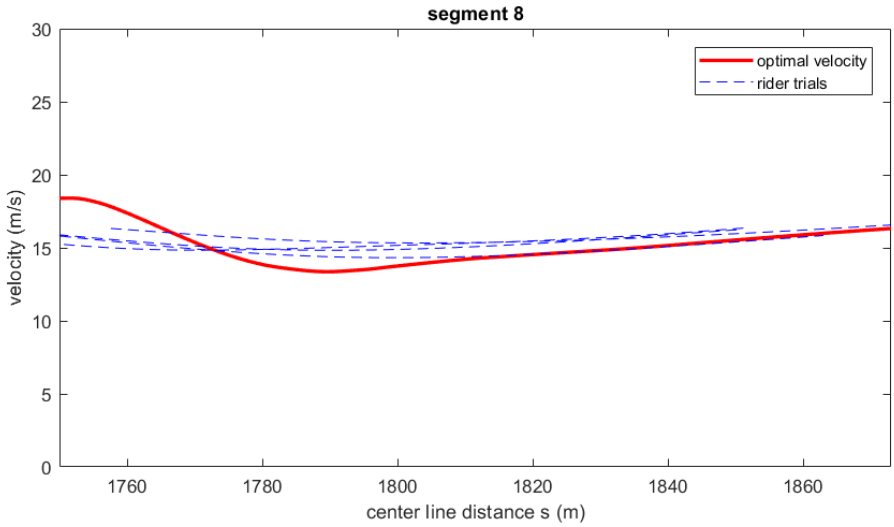

Figure G.23: Comparison of the optimal velocity to the measured velocities for the final segment.

g-g diagram-

It is once again shown by the optimal solution that more lateral acceleration and braking can be reached than the cyclists dare to (figure G.24). Apart from this, no important differences are seen. The plot furthermore confirms that the trajectory of segment 8 is not wobbly at all, this is caused by the way of presenting the trajectory. If the cyclist would cycle such a oscillating path, more divergence in lateral accelerations would be seen.

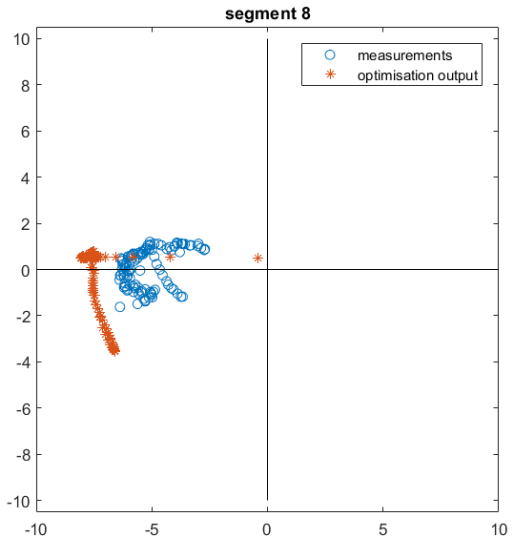

Figure G.24: The numerical g-g diagram compared to the optimal controls for segment 8.

H

Multiple regression sample selection

Table H.1: The ranges of all variables used in multiple regression. Within this range, random values were generated, uniformly distributed over the range (with help of MATLAB's *rand* function)

symbol	description	range	motivation
v	velocity of the cyclist	3-30	speed range Tour de France
ψ	elevation with respect to the inertial xy plane	-0.26-0.26	double the maximum elevation in the L218
γ	banking with respect to the inertial xy plane	-0.26-0.26	double the maximum banking in the L218
β	twist angle	$-0.5\pi - 0.5\pi$	all possible angles
$\dot{\beta}$	time derivative of β	-0.4-0.4	maximum possible $\dot{\beta}$ velodrome
κ	curvature of the center line	-0.3-0.3	minimum radius of curvature of 3.33 m
n	lateral road position	-3-3	width of a two-lane road
χ	angle between the center line tangent and the bicycle longitudinal direction	-0.5π-0.5π	maximum possible angle

I

Scatter plots of sample data

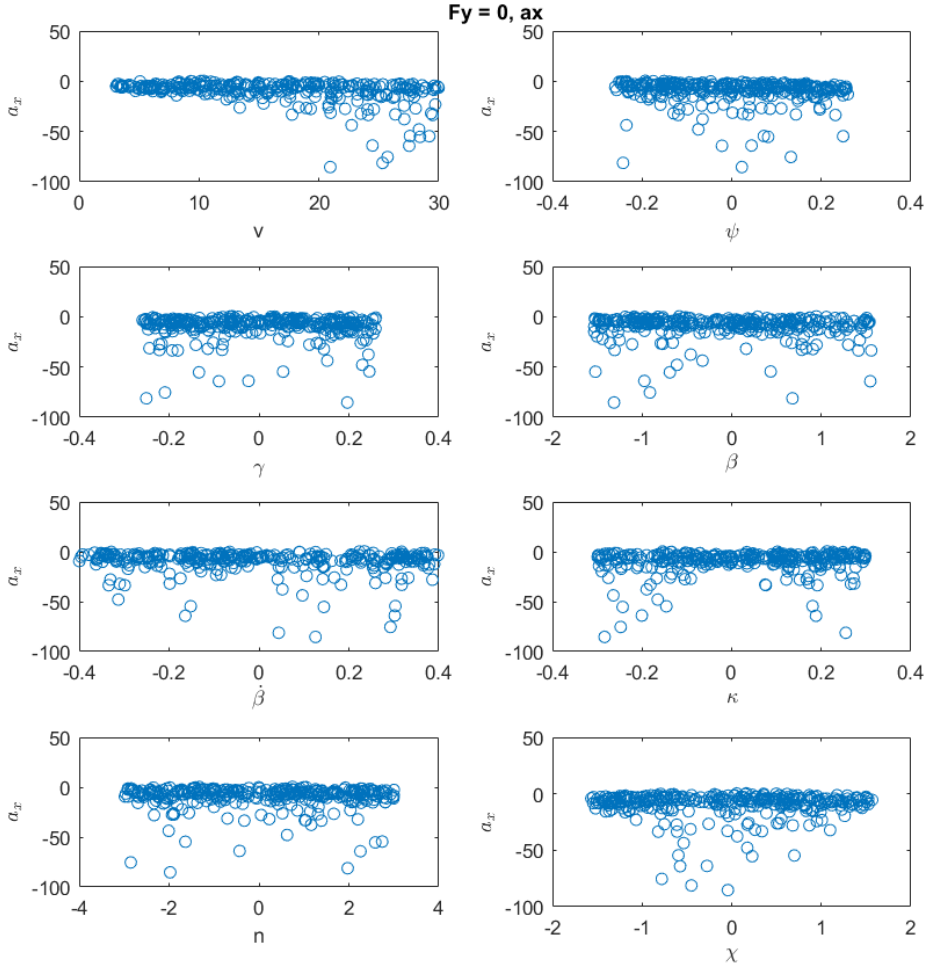

Figure I.1: The scatter plots show the correlation between the separate untransformed independent variables and a_x. For the variables β, κ, and χ nonlinear correlations are observed. As those variables describe angles, and the angles are always inputs for goniometric functions, variable transformations are proposed that take this into account.

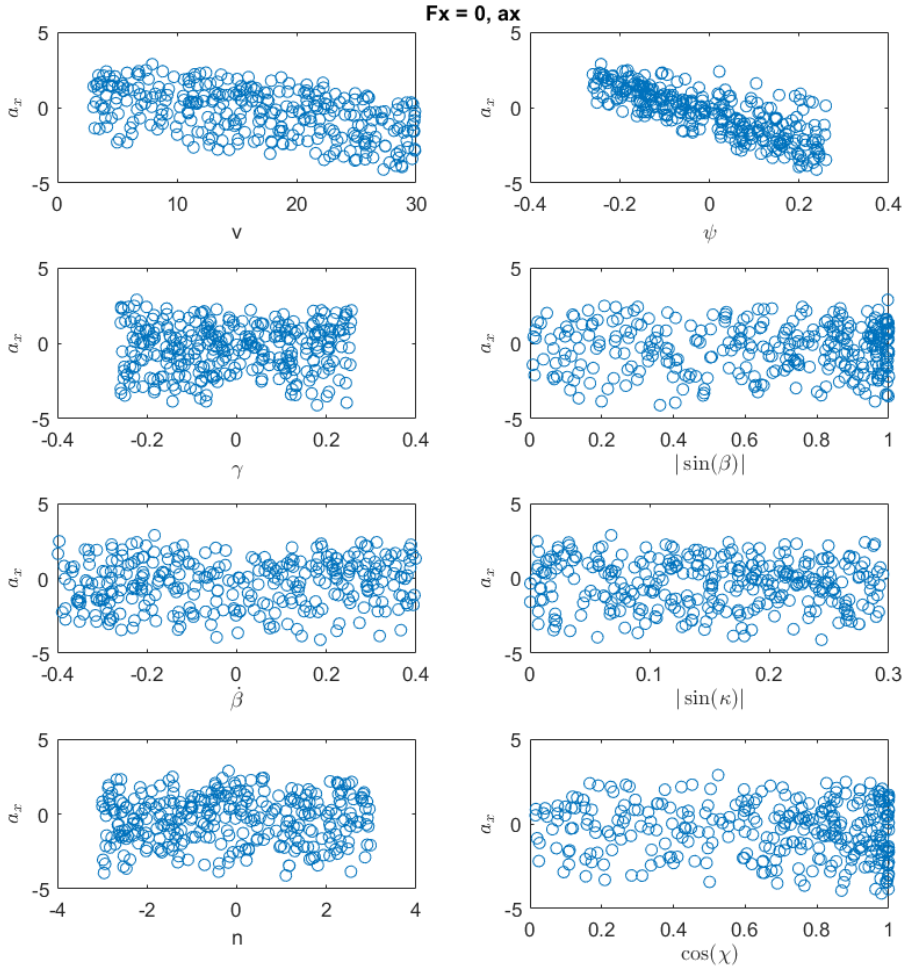

Figure I.2: The scatter plots show the correlation between the separate independent variables and a_x for the position on the Fx = 0 line. For v and ψ, clear linear relationships are visible.

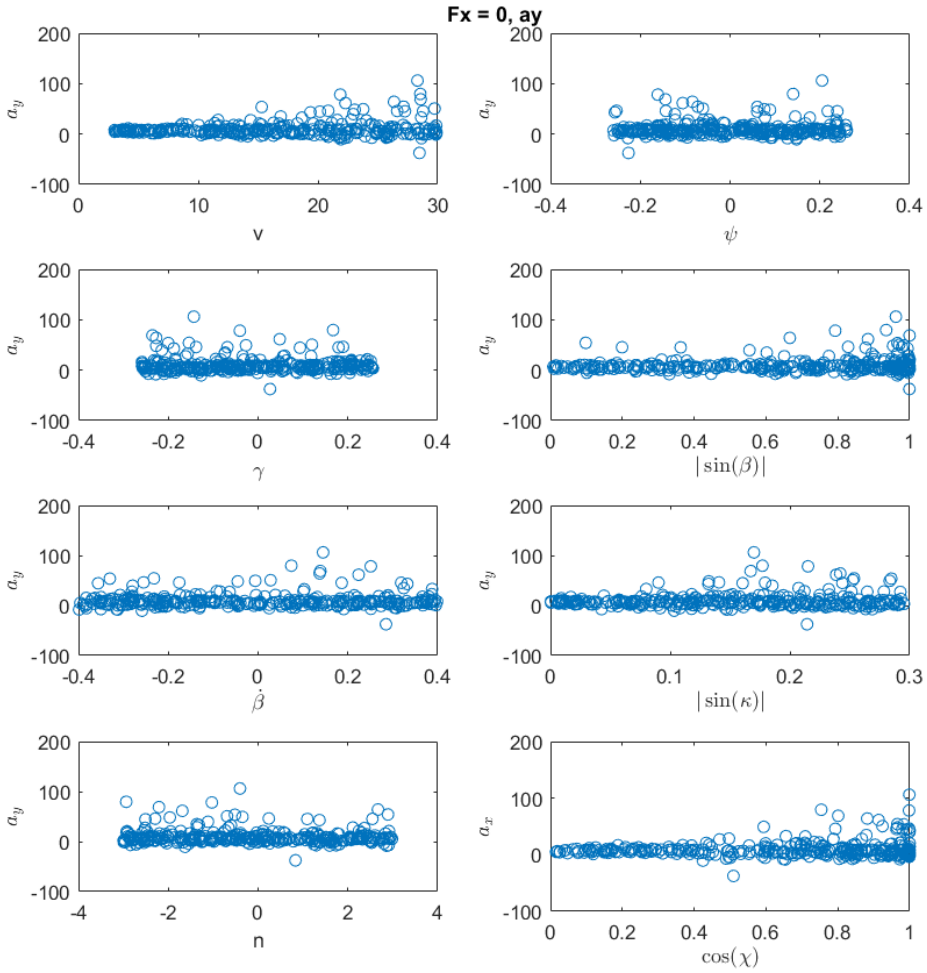

Figure I.3: The scatter plots show the correlation between the separate independent variables and a_y for the position on the Fx = 0 line. No clear linear relationships are visible.

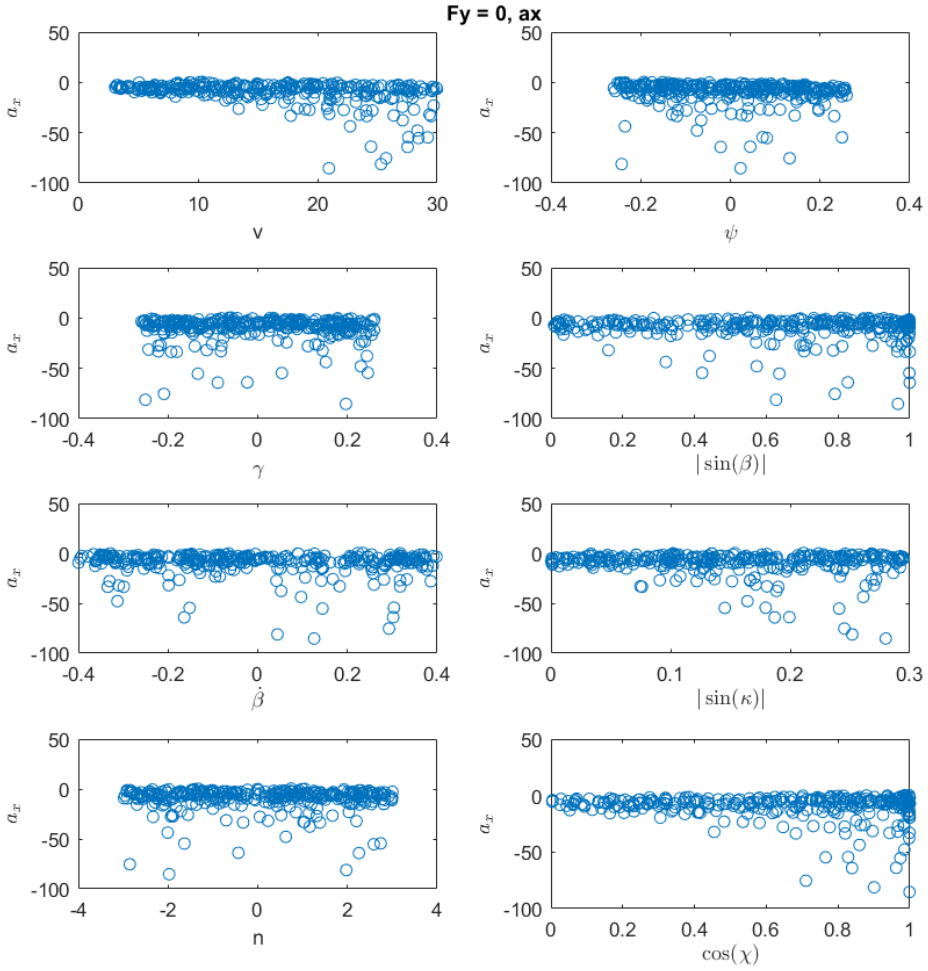

Figure I.4: The scatter plots show the correlation between the separate independent variables and a_x for the position on the Fy = 0 line. No clear linear relationships are visible.

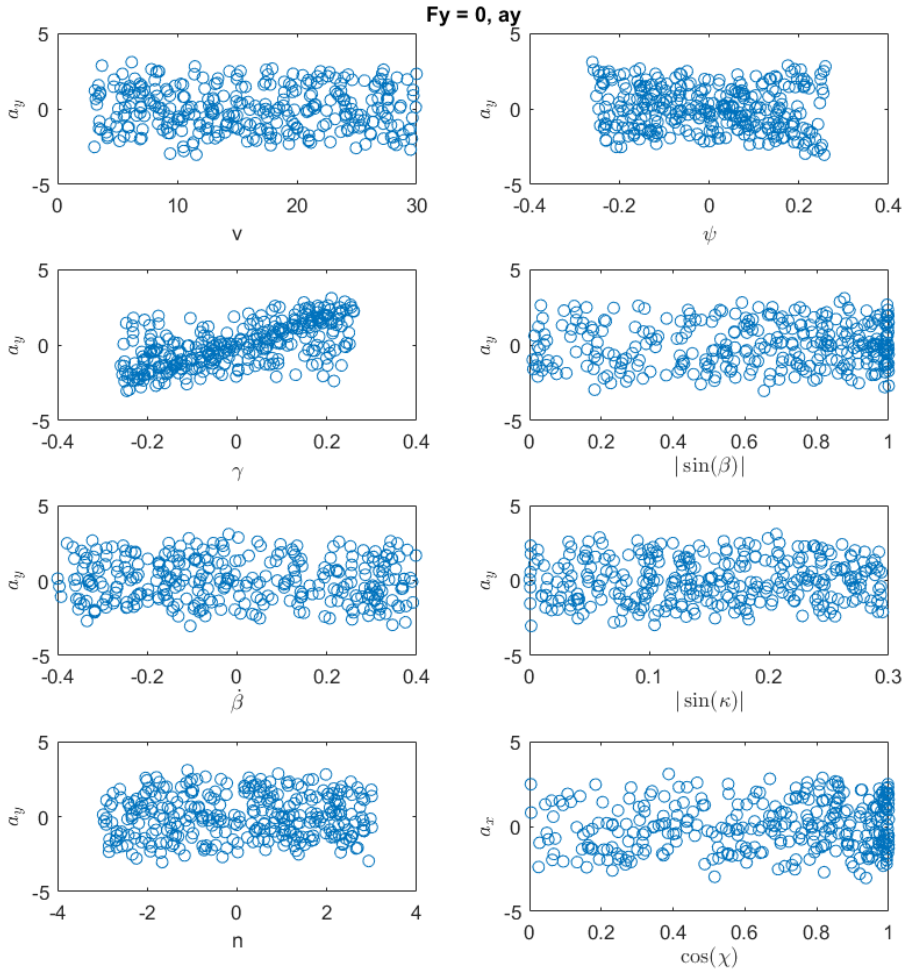

Figure I.5: The scatter plots show the correlation between the separate independent variables and a_y for the position on the Fy = 0 line. For γ, a clear linear relationship is visible.

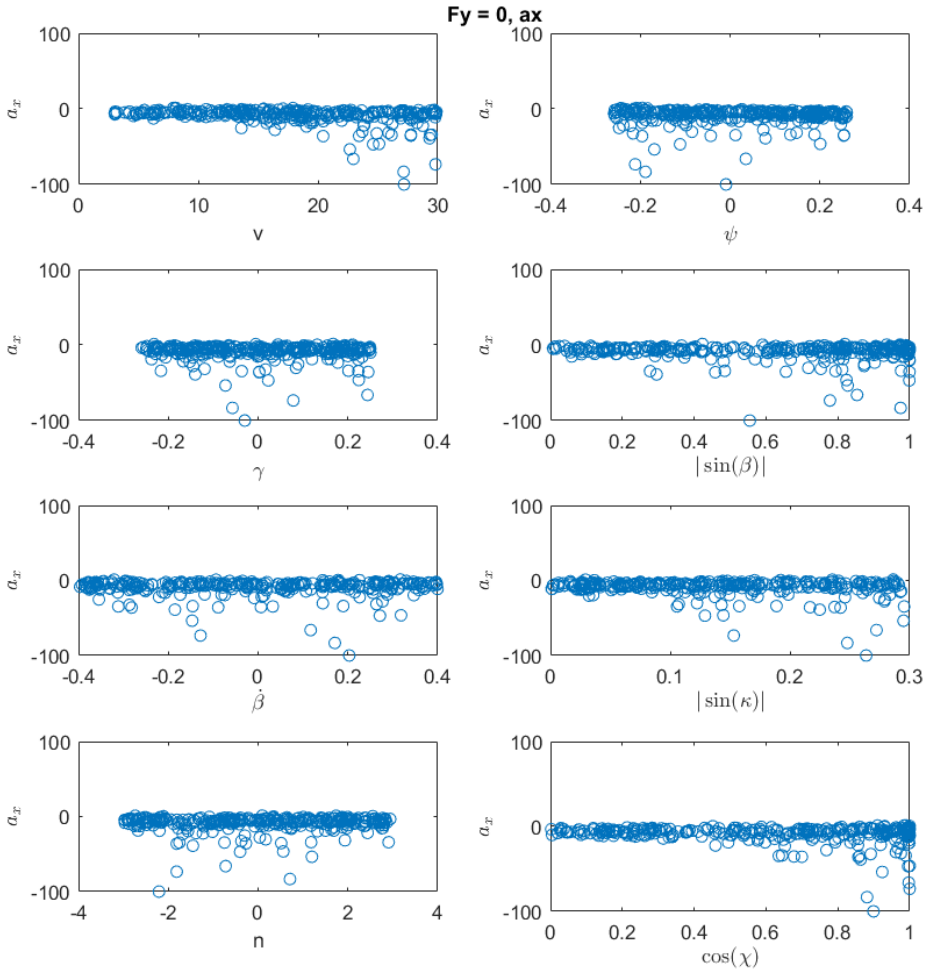

Figure I.6: The scatter plots show the correlation between the separate independent variables and a_x for the position on the -Fx = Fy line. No clear linear relationships are visible.

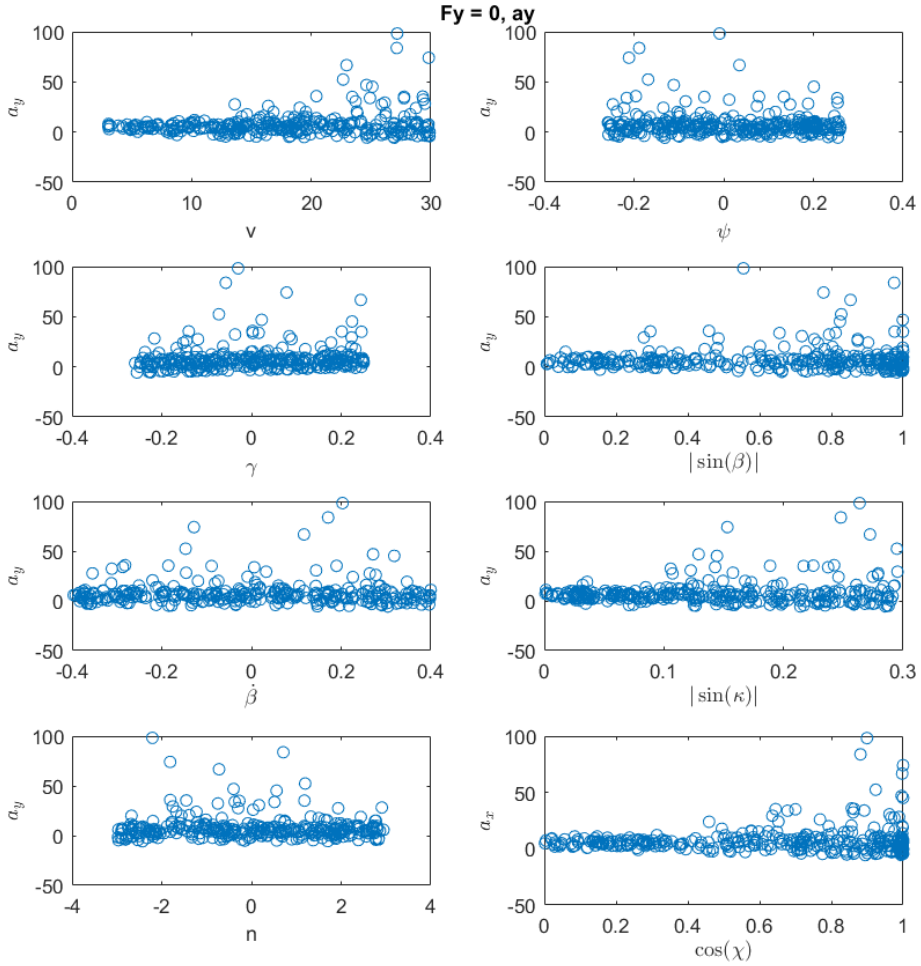

Figure I.7: The scatter plots show the correlation between the separate independent variables and a_y for the position on the -Fx = Fy line. No clear linear relationships are visible.

J

Calculation of the maximum roll angle

In figure J.1 some bicycle geometry aspects are reported. The lengths represent a bicycle of a relatively short person (crank length 170 mm), since this data was the easiest to find [12, 14].

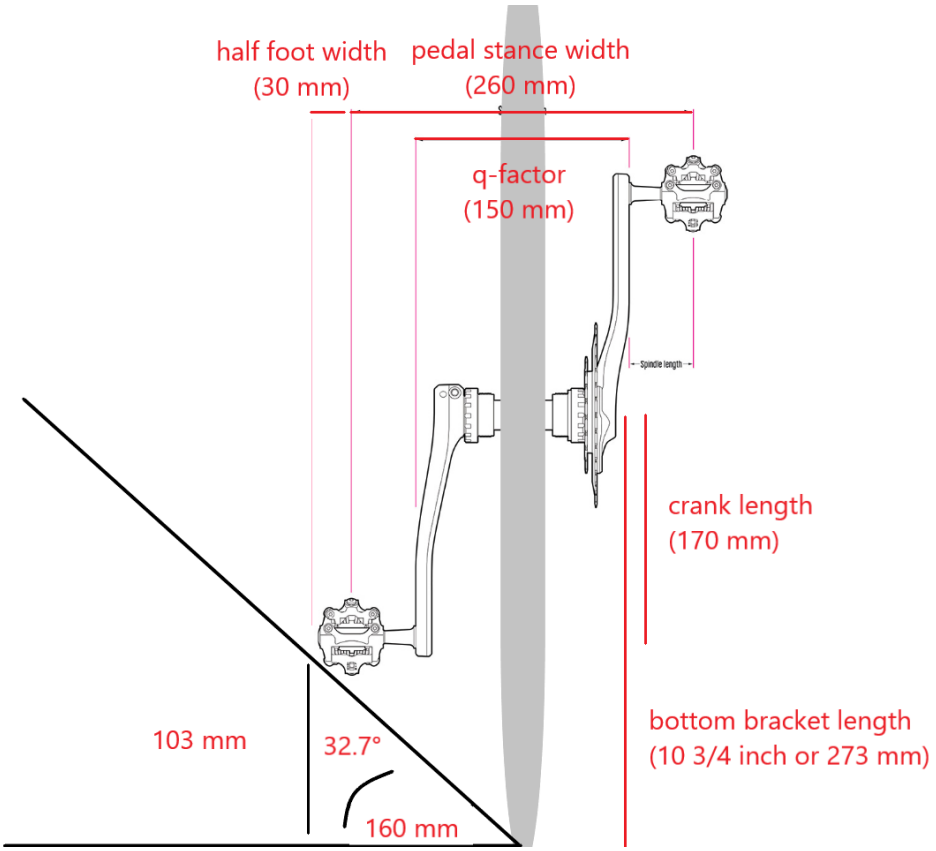

Figure J.1: The angle between the ground and the lower pedal in upright position equals the maximum roll angle of the bicycle. Figure altered from [37]